General Disclaimer

One or more of the Following Statements may affect this Document

- This document has been reproduced from the best copy furnished by the organizational source. It is being released in the interest of making available as much information as possible.

- This document may contain data, which exceeds the sheet parameters. It was furnished in this condition by the organizational source and is the best copy available.

- This document may contain tone-on-tone or color graphs, charts and/or pictures, which have been reproduced in black and white.

- This document is paginated as submitted by the original source.

- Portions of this document are not fully legible due to the historical nature of some of the material. However, it is the best reproduction available from the original submission.

CR 167835

16514

FINAL REPORT TO NASA: CONTRACT 9-~~1665~~

Period Nov. 1, 1981 - Oct. ~~31~~, 1982

E83-10346

STUDY TO ASSESS THE IMPORTANCE OF ERRORS INTRODUCED BY APPLYING NOAA 6 AND NOAA 7 AVHRR DATA AS AN ESTIMATOR OF VEGETATIVE VIGOR: FEASIBILITY STUDY OF DATA NORMALIZATION

(E83-10346) STUDY TO ASSESS THE IMPORTANCE OF ERRORS INTRODUCED BY APPLYING NOAA 6 AND NOAA 7 AVHRR DATA AS AN ESTIMATOR OF VEGETATIVE VIGOR: FEASIBILITY STUDY OF DATA NORMALIZATION (State Univ. of New York, G3/43

N83-27321

Unclas 00346

State U. of New York

M.J. Duggin and D. Piwinski

Technical Monitor: Dr. V. Whitehead

Project Director: Dr. M.J. Duggin

FINAL REPORT TO NASA: CONTRACT 9-1663

Period Nov. 1, 1981 - Oct. 31, 1982

E83-10345
CR-167835

STUDY TO ASSESS THE IMPORTANCE OF ERRORS INTRODUCED BY APPLYING NOAA 6 AND NOAA 7 AVHRR DATA AS AN ESTIMATOR OF VEGETATIVE VIGOR: FEASIBILITY STUDY OF DATA NORMALIZATION

M.J. Duggin and D. Piwinski

Technical Monitor: Dr. V. Whitehead

Project Director: Dr. M.J. Duggin

CONTENTS

		Page
1.	Introduction	1
2.	The anisotropy of the reflectance properties of the ground	8
3.	The effect of the atmosphere	10
4.	Simulation studies: an aid to the generalization of empirical findings	12
5.	Observations of goniometric anisotropy in recorded radiance	14
6.	Experimental studies: empirical studies of target radiance	16
7.	Effect of random variability on target discriminability and quantification	20
8.	The effect of unresolved (sub-pixel sized) cloud on recorded radiance	28
9.	Simulation studies: findings	32
10.	Conclusions	34
11.	Acknowledgements	36
12.	References	37
13.	Table captions	42
14.	Figure captions	43

1. Introduction

In this section we outline the theoretical and experimental work performed in response to the statement of work, the primary contents of which are discussed here. It is noted that, while using the image data archives and computation facilities at JSC Houston as agreed to originally, difficulties were encountered in obtaining time on the computer due to an overload situation. This has severely restricted the amount of throughput which it has been possible to obtain, using digital data from the NOAA AVHRR in the reported time period. For this reason, in FY 1983 we plan to rent time on a commercial image analysis computer in our attempt to obtain our findings in a more timely fashion. However, we wish to extend our thanks to NASA and to Lockheed support staff, especially G. Ryland, for their willing help in a difficult situation generated by heavy computer usage.

It has already been demonstrated by the Early Warning Crop Condition Assessment (EW/CCA) Project in AgRISTARS that the NOAA 6 and NOAA 7 Advanced Very High Resolution Radiometer (AVHRR) data is useful, in conjunction with meteorological and historical crop information, for mapping and monitoring vegetative (crop) cover on a coarse scale. The Foreign Agriculture Service (FAS) of the USDA is already using this data for assessment purposes. However, due to sources of error in the data, detailed below, the FAS is currently able to use only the central 25% of each image.

The purpose of this project has been to identify and to evaluate potential sources of error in the AVHRR digital data so that appropriate steps may be taken to develop algorithms to minimize the effect of those artifacts detected in the data (artifact being here defined to consist of that part of the signal which not only contributes no useful information on the ground feature of interest (i.e., vegetative canopy), but which indeed obscures the nature and condition of the canopy insofar as said nature and condition may be ascertained from an analysis of the AVHRR digital data).

Artifacts have been found to exist in the data due to anisotropic reflectance properties of the earth's surface and due to anisotropic back-scattering of light from the atmosphere into the sensor. These two effects, coupled with an interaction of the spectral distribution of the radiance incident on the sensor (and the angle dependence of this quantity) with the spectral response of the sensor gives rise to a scan angle-dependence of the sensor imagery. While part of the anisotropy will be random (which cannot be calibrated out of the data) most will be systematic (which can be calibrated out). The systematic variation of scanner data with view angle has been observed for the Landsat MSS[50], which has scan angle limits of $\pm$ 5.8°: the variation will obviously be much larger in the case of the AVHRR, which has scan angle limits of $\pm$ 54°. For this reason, the present investigation has been directed towards predicting the nature and magnitude of the anticipated scan angle-dependence of recorded radiance in order to understand the nature of the effects and to help extend the findings of

parallel, empirical studies. Findings from empirical studies of digital remotely sensed images are shown to be in support of the predictions of the deterministic simulation studies. This fact lends support to the expectation that the outcome of this investigation will be workable algorithms to normalize artifacts from the digital scanner data.

At present, as mentioned above, only the central 25% of the AVHRR data is used in global crop condition assessment by FAS. Since the probability of cloud is extremely high in some crop growing regions, it will be necessary to extend beyond the central 512 pixels (the central 25% of the image*) in order to obtain images at frequent intervals in time, so as to track dynamic changes in the vegetative canopy and so monitor crop condition.

Even moderately effective correction algorithms might extend the useful part of the scanner image to the central 50%, thereby doubling the frequency of effective coverage of all those areas covered. This would greatly enhance the probability of getting adequate coverage of most areas (even those with high frequency of cloud cover) throughout the growing season, so that information on crop condition may be obtained and updated in a timely manner to permit policy decisions to be made.

At present, the concept of obtaining recorded radiance simultaneously in several optical channels is favored. This provides a "measurement vector" for each area on the ground represented by a pixel. Assuming that sufficient

---

*Pixel length varies strongly with scan angle across track (E-W) by a factor of over 6 at the edge of the scan[52]. Each pixel represents an equal angular increment of the AVHRR mirror, not an equal sized ground area.

is known about the area being mapped, it is possible, in 'supervised classification' analysis, to train the computer to recognize areas of known constitution on the basis of the recorded radiance signatures. In the training process, the pixels of the (known) training areas are then clustered in n-dimensional (where n = no. of data channels) measurement space where each measurement channel represents an axis (dimension). In order to optimize discriminability of the clusters formed by the measurement vectors for pixels of known nature, it may be necessary to transform the measurement vector into a "feature vector". This is achieved by means of a transformation matrix and may result in fewer and/or altered vector elements. Further operations are then performed upon the clusters in n-dimensional "feature space". A decision rule (either (1) a deterministic, arithmetic or geometric algorithm or (2) a statistical, generally Bayesian, algorithm) is then used to decide to which cluster each pixel is most likely to belong. This is achieved by considering boundaries to exist between the clusters in feature space (called, for this purpose, decision space) and by using the selected rule to decide within which boundaries (i.e. within which region of decision space) each pixel belongs.

The assumption is, of course, that the "known" areas on the ground, from which the clusters in measurement space are deduced, have the same optical properties in different locations. For example, if you have only a few training areas on wheat in country 'A', can you reasonably expect that the cluster in measurement space to which the pixels obtained from 'A'

(using the selected sensing device) belong will also contain the measurement vectors from the same crop in country 'B'. The problem is one of what is termed "signature extension". Of course, one need not even go outside the borders of the USA to realize that signature extension is indeed a problem. Further, distortions of measurement vectors by those artifacts (arising from anisotropy) mentioned above will only serve to exacerbate the situation.

The alternative to supervised classification is called (surprise!) unsupervised classification and is used when not enough ground information exists to be able to "train" the computer to recognize specific ground cover types ("classes" or "themes"). The measurement vectors (or feature vectors, if a transformation is applied prior to the classification process) are allowed to fall into clusters according to the naturally occurring spectral differences between the pixels. Not only may such clusters be less separable (since it is not possible to orient the transformation from measurement space to feature space to specifically separate clusters known to represent training areas of known type at ground level) but the assumption that clusters of measurement or feature vectors represent each class or theme in an identifiable manner may not be tested. In other words, it is implicitly assumed that the recorded spectral radiance from a class is representative of that class in a predictive fashion. This may not be the case. Thus, it is not surprising that the classification accuracy (found in the case of supervised classification by using "test areas" of known class) has been found in several studies to be lower for unsupervised than for supervised classification.

While there may be, in the future, great possibilities for automated classification of digital remote sensing data, present FAS studies of crop type and condition and Early Warning Project studies involve the visual investigation of processed AVHRR data.

Instead of using automated clustering algorithms, the measurement vector is abridged from n-dimensions (or m-dimensions, as discussed above, for the feature vector) to form a two-dimensional feature vector. The manner in which the features are combined varies, but the result is what is hoped to be a measure of vegetative vigor (vegetative indes). There are over 50 such indices[53,54] involving two bands of information; the reflected red and infrared, and it may be shown that all of the indices are related. It may be shown that correlations exist between ground targets and remotely sensed radiance levels. However, it has not yet been completely demonstrated that remotely sensed radiance levels may be used to uniquely characterize the nature of ground targets (e.g.[55]). In other words, studies showing that there is a correlation between a vegetative index and some feature of the vegetative canopy do not adequately demonstrate that the vegetation feature considered is the only one controlling the recorded radiance levels.

The vegetation indices considered here were

$$\text{VIN 1} = \text{AVHRR 2} - \text{AVHRR 1}$$

which refers to the difference in radiance recorded in the first two AVHRR channels and

$$\text{VIN 2} = \frac{\text{AVHRR 2} - \text{AVHRR 1}}{\text{AVHRR 2} + \text{AVHRR 1}}$$

These indices and modifications of VIN 1 are used by the Early Warning AgRISTARS project and by FAS.

In simulation studies and in empirical observations, VINs were calculated and angle-dependence studied, as well as the angle dependence of the recorded radiance values.

It is worth mentioning that difficulties arose in this study, not only due to the heavy use of the computer facilities at the AgRISTARS project, but because of the dynamic state of the procedures used to process those tapes used in the analysis of digital radiance levels. An example is the difficulty in determining what corrections (such as sun angle correction) had been applied to the AVHRR tapes. Further difficulties arose due to difficulties in location of and access to the data.

2. The anisotropy of the reflectance properties of the ground

Measurements of reflectance factors at ground level have been made for a variety of sun-target-sensor geometries.[1-13] These measurements show that there is a considerable degree of angular anisotropy in the bidirectional reflectance factor and in the hemispherical-conical reflectance factor. The geometrical nomenclature is shown in Fig. 1. Here, the sun is at a zenith angle z to the vertical and at an azimuth angle ϕ with respect to a reference direction (usually north = N) on the horizontal plane. The detector records radiance at a view zenith (scan) angle θ' with respect to the vertical and at an azimuth ϕ' with respect to the above reference direction in the horizontal plane. A perfectly diffuse reflector would obey Lambert's reflection law and would reflect radiance equally in all directions (i.e. all θ',ϕ'). Real reflectors can be extremely anisotropic in their reflectance properties.

There are stochastic[13-15] and deterministic[16-18] models of the vegetative canopy which describe the angular dependence of the reflectance factor and which have been tested against theory[3,4,12]. The agreement is generally good.

There is a paucity of experimental data. While some excellent measurements have been recorded for wheat and for soybeans in the LARSPEC data file at Purdue University, these are the only complete (i.e. covering the whole hemisphere) reflectance factor data sets which exist. Thus, in order to study the goniometric anisotropy of a variety of vegetation canopies, it will be necessary to obtain enough simultaneously acquired biophysical

(e.g. leaf area and disposition, spectral transmission and reflectance of leaves) and canopy reflectance data to calibrate the canopy reflectance models so that they may be extended into other angular regimes for prediction purposes.

Typical experimental canopy reflectance data are shown in Figs. 2-9 for wheat. The growth stages for wheat are 3.5 (boot) and 4.5 (fully headed) on the modified Feeks scale. The scan angle plan is selected so as to correspond to that of the AVHRR on NOAA 6 and NOAA 7. The dependence of the reflectance properties of the vegetative canopies upon view zenith (scan) angle and upon view azimuth angle is evident.

3. The effect of the atmosphere

The atmosphere interacts with radiance from the sun in such a way that irradiance falling on the top of the atmosphere is absorbed and scattered preferentially in some parts of the spectrum. Generally, the atmosphere acts in such a way as to reduce the intensity of radiation incident on the ground (e.g. [19]).

The irradiance on the ground will consist partly of 'sky' radiance and partly of direct solar illumination depending on the amount of haze and on the amount of cloud in the sky. A curve showing spectral global irradiance is shown in Fig. 14a. Typical ratios of diffuse to direct radiance are shown in Fig. 14b. The measurements from which these curves were constructed were made at ground level using a radiometer with a cosine receptor.

The reflectance properties of the ground are dependent to some extent upon the polar (goniometric) distribution of the radiation field incident at ground level.[20-22]

The radiance reflected by the ground is partly scattered by the atmosphere, reducing signal. However, there is additional radiance which is backscattered from the sky into the sensor. This is termed "path radiance" and may be assessed experimentally from ground measurements made simultaneously with remote sensing data acquisition (e.g. [23-25]). Path radiance may also be experimentally assessed from the remotely sensed data (e.g.[26-29,35]).

An alternative approach is to use models of the atmosphere. Given certain assumptions in the construction of the atmosphere (e.g. formed of layers of different transmission) it is possible to calculate path radiance for various sun-target-sensor geometries, given the scattering particle size and density distribution (e.g.[29-35]).

Yet another approach, is to use the look-up tables calculated by Dave[36-39] for the effects of atmospheric transmission and backscatter. Dave used three different aerosol distributions to represent different climatic conditions. The tables cover all possible sun-target-sensor geometries. While the parameters used by Dave do not provide the answer for all atmospheric conditions, at least this method is useful insofar as it provides a ready method of computing atmospheric effects on remote sensing data. The only drawback is that Dave assumes that the ground reflects with equal efficiency into all view zenith and azimuth angles (i.e. behaves like a Lambertian reflector). This is not sufficiently accurate for representations of data recorded by sensors with large scan angle limits.

Table 1(a) shows typical values of atmospheric extinction optical thickness used for a 'clear' atmosphere (visibility >50 km) and for a 'turbid' atmosphere (visibility <10 km). Table 1(b) shows path radiance calculated for various scan angles towards the sun ($\phi' = 0^{o}$) and away from the sun ($\phi' = 180^{o}$) ([34,40]).

It should be noted that the predictive models are based upon fundamental assumptions and may make corrections for systematic atmospheric effects. However, they will not allow for random effects (e.g.[41]). The correction for atmospheric effects is thus complex, despite the ingenuity of workers in the field.

4. Simulation studies: an aid to the generalization of empirical findings

While it is necessary to make empirical calibrations on an image-by-image basis, it is also necessary to develop an *a priori* understanding of the cause of variations in radiance level and in radiance signature across a scene. This will promote an understanding of the factors involved in causing the anisotropy of detected radiance, enabling data collection conditions to be optimized. When considering data from existing sensors, this means a more prudent selection of imagery to serve a particular purpose. Future applications should involve an optimization of sensor geometry and of spacecraft ephemeris to optimize the detectability or discriminability of particular ground features or characteristics. Simulation models have been described [43-48]. The radiance recorded in a particular bandpass of a sensing device may be described by the following equation:

$$R_r = \frac{\int_{\lambda_1}^{\lambda_2} I(\lambda) \cdot \{E(z,\lambda).R(z,\phi;\theta',\phi',\lambda).\tau(\theta',\lambda) + L_{path}(z,\phi;\theta',\phi'\lambda)\} .d\lambda}{\int_{\lambda_1}^{\lambda_2} I(\lambda).d\lambda} \quad (1)$$

Where:

$I(\lambda)$ = spectral instrument response.

$E(z,\lambda)$ = spectral global irradiance on target

$R(z,\phi;\theta',\phi',\lambda)$ = spectral hemispherical-conical reflectance factor

$\tau(\theta'\lambda)$ = spectral atmospheric transmission

$L_{path}(z,\phi;\theta',\phi',\lambda)$ = spectral atmospheric backscatter (path radiance)

λ_2,λ_1 = (respectively) upper and lower wavelength limits of sensor bandpass at zero power.

The wavelength iependence of these parameters will be marked in the case of the reflectance factor $R(z,\phi;\theta',\phi',\lambda)$ and in the case of the irradiance $E(z,\lambda)$. The instrument response $I(\lambda)$ will be dependent upon the sensing system and may vary rapidly with wavelength. The atmospheric transmission and backscatter or (path radiance) will vary somewhat more slowly with wavelength.

Typical examples of the wavelength dependence of these parameters are shown in Fig. 15. These parameters will interact, in a manner which depends upon the wavelength-dependence and angle-dependence of each parameter (e.g.[48]). The spectral responses of the first two bands of the NOAA 6 AVHRR are shown in Fig. 16. It is necessary to be aware of the magnitudes of such interactions.

Data exist in the LARSPEC files at Purdue University (e.g.[49]) for the angle dependence of the reflectance properties of wheat and, as an example, these were used to compute the anticipated normalized sensor outputs for the NOAA 6 AVHRR. The angular parameters for the wheat reflectance data selected corresponded to the NOAA 6 overpass ephemeris parameters (i.e. for sun-target-sensor geometry). The maturity stage of the wheat when the reflectance measurements were made was 4.5 on the modified Feeks scale. The simulated results are shown in Fig. 17. It is seen that the simulated data show a dependence on view zenith (scan) angle and also upon atmospheric turbidity. These findings and others which will be shown later support experimental observations of radiance made on NOAA-AVHRR images.

5. Observations of goniometric anisotropy in recorded radiance

Observations have been made of a scan angle dependence in Landsat-Multispectral Scanner (MSS) imagery[50]. The MSS has scan angle limits of only $\pm$ 5.78°. The NOAA Advanced Very High Resolution Radiometer (AVHRR) has much larger scan angle limits of $\pm$ 54°. Further, the Landsat D thematic mapper (TM) has proposed scan angle limits of $\pm$ 26°. The SPOT satellite high resolution visible radiometer (HRV) has a proposed angular range of $\pm$ 27° from nadir. Therefore, it is to be expected that for sensing systems with large polar view (scan) angle limits, the scan angle effect will be larger. This is in fact the case (e.g.[46-48]). It is necessary to calibrate digital radiance levels in each channel to the nadir value. This facilitates the within-image and between-image calibration necessary for meaningful signature extension, so that automated or semi-automated image classification procedures may be performed for the whole image with minimum of errors of omission and/or commission. If it is not possible to calibrate the entire image back to nadir then it is necessary to know the practical scan angle limits which must be applied in order to ensure minimum recorded radiance error over the angular range used. In the case of sensing systems with large scan angle limits (such as the NOAA AVHRR) the larger the usable angular range, the more frequent the available coverage over a given area under cloudfree conditions is likely to be. Practical economic and logistical advantages obviously accrue from using as much of an image as possible.

The NOAA AVHRR has scan angle limits of $\pm$ 54° across a 2048 pixel swath. The pixels are 1 km x 1 km at nadir, but increase greatly (by a factor of >6) at extreme scan angles[52].

Two examples of the observed variation in radiance from an AVHRR image collected during this project on an apparently perfectly clear day are shown in Fig. 18 for agricultural terrain and forest in the north central United States imaged on Julian dates 187 and 192 1981 (nadir over Illinois). However, as will be mentioned later, there is no way to be sure that haze, cirrus and unresolved cloud were not present in part(s) of the image. Fig. 19 shows the scan-angle dependence for an image in which some popcorn cloud and haze were present at large scan angles. Here, the variations in recorded scene radiance at view zenith exceeding $\pm$ 25° are probably due to a combination of cloud and cloud shadow[51].

It is seen that the scan angle-dependence of the recorded radiance and of the vegetative index (VIN) generated from the recorded radiances in AVHRR bands 1 and 2 (in this case

$$\text{VIN 1} = \left\{\frac{\text{AVHRR 2 - AVHRR 1}}{\text{AVHRR 2 + AVHRR 1}}\right\}$$

show the same general behavior as the simulated data.

6. Experimental studies: empirical studies of target radiance

The NOAA image tapes were mounted by Lockheed (G. Ryland) and screened for cloud. Those images which were free from cloud for a 50 line swath across the image, over the North Central and Central USA were selected for analysis. Cloud always appeared somewhere, above or below the swath used. The data used was from Global Area Coverage (GAC) tapes, in which four pixels were averaged out of every sequence of five on every third scan line. The cloud screening process was achieved empirically (by eye) using the USDA interactive computer (IMDACS system). The averaged "representative pixels" on the GAC tapes were displayed in false color. The gains and offsets were so adjusted to produce optimum apparent feature separation and each image was photographed for subsequent reference. Selected images were written to disk for subsequent analysis.

This form of analysis suffered from the drawback that only visibly detected cloud (white pixels or pixels which were so low in color saturation as to probably be cloud) was used as a criterion for image acceptance or rejection and for swath location. Another difficulty was in the determination of exactly what treatment the tape had had in prior processing. Some images were archived in the belief that they were raw data (i.e. unaffected by pre-processing) when in actual fact, vertical striping lead to the discovery that they had been "sun angle corrected" (modified with a cosine factor). While this was a useful correction for FAS, in this instance it served as a complication for us (thus proving Sevareid's Law: "The chief cause of problems is solutions").

Close examination was made of five swaths on a total of four separate GAC images out of the many screened. The screening was a lengthy process, involving many tape mounts. This occupied many sessions. For administrative reasons, it was necessary that these sessions on the FAS computer be performed by Lockheed.

After selection of the swath, the radiance values were averaged for all fifty consecutive (GAC) lines. The mean of each set of eight sequential GAC pixels was averaged for 50 GAC lines and plotted as a function of scan angle. The dates of the images used are shown in Table 2. Typical curves are shown in Figs. 20-39. Curves for the pooled data are shown in Figs. 40-43. The pooled data include one set which is not shown in Figs. 20-39. Each successive sequence of four diagrams shows, respectively, the mean relative recorded radiance in AVHRR 1, the mean relative recorded radiance in AVHRR 2, VIN 1* and VIN 2**: each variable is expressed as a function of scan angle (on the diagram the angle is expressed in radians).

It is clear that there is a scan angle dependence of all of these variables and that, indeed, even VIN 1 (a variant of which has been used by FAS as an algorithm to screen cloud) is scan angle-dependent. It is further apparent that the scan angle dependence appears to be of the same form in each case (i.e. for each swath).

---

*VIN 1 = (AVHRR 2 - AVHRR 1)

**VIN 2 $= \left\{\frac{\text{AVHRR 2 - AVHRR 1}}{\text{AVHRR 2 + AVHRR 1}}\right\}$

Computer curve fits were run on all of the data sets shown in Figs. 20-43 and the coefficients of the fitted curves are given in Tables 3-6.

It is seen that the coefficients are not the same but are somewhat similar. More work needs to be done on a larger data set, although the results are suggestive of an "average curve" which may be fitted, resulting in a predictable maximum error in radiance or VIN at a given scan angle.

This method of analysis suffers from the disadvantage that the target may vary across the viewed area, although the viewed region always consisted of farmland under crop (with a closed canopy) and forest. In order to determine whether the scan angle-dependence of the radiance and of the VIN's (shown in Figs. 20-43 and in Tables 3-6) was indeed target dependent, like areas were each examined from different view angles, using data obtained on different days. The radiance values are shown plotted against view angle in Fig. 44 for a mixed forest. The analyzed area consisted of over 300 pixels, except for one image where the viewed area was close to the end of the scan line and so consisted of only about 60 pixels, whose dimensions were much larger than those of the nadir pixels[52]. There is clearly a strong scan-angle dependence of AVHRR 1 and of AVHRR 2: the form of the dependence is the same as that observed using the previous method of analysis. Again, much more work is needed.

The third band of the AVHRR was also used in an experimental sense to detect tenuous cloud, cirrus and haze. It is thought that lower temperatures would occur over cloud and that for this reason, the thermal infrared

channel would be useful in detecting cloud. Visual examination of the data on the interactive computer tends to support this argument, as does a study of the averaged GAC 50 band swath for AVHRR 3 in conjunction with averaged AVHRR 1 and 2 values. However, it is too early to be sure at this stage how useful this approach will be.

An interesting approach suggested by V. Whitehead[56] is that the variance of the radiance and VIN data, expressed as a function of scan angle, will depend upon the presence of cirrus, haze and tenuous cloud. While the approach appears promising, more work is needed before conclusions may be safely drawn.

7. Effects of random variability on target discriminability and gratification.

There are two components to target radiance variability. The first is systematic; and the more we know about the system, the better our calibration for this component will be. This systematic variation in target radiance will arise due to sun-target-sensor geometry, percentage of cloud or haze in the pixel and atmospheric backscatter. The random components will be due to: (a) topographic variations causing local changes in shadowing and sun-target-sensor geometry variations; (b) pixel composition variation; (c) wind causing changes to canopy morphology; (d) random atmospheric variations (e.g., aerosol content and density distribution); (e) irradiance fluctuations at the target to name only some of the causes. In this section, we consider only random variations in irradiance and in target reflectance. The following is an abstraction of a recent work by Duggin.[58]

Variations in surface reflectance and in irradiance and atmospheric transmission in bandpass r are noise, and place limits on the minimum signal difference necessary for target discrimination. We concentrate in this study on the noise components introduced by surface reflectance variability, by variability of solar irradiance at the target and by atmospheric transmission variability.

The irradiance falling upon the target varies with solar elevation in a diurnal fashion, but the spectral distribution of the irradiance also varies. Besides the diurnal variation, there is also a high frequency variation, of unknown period (Duggin[41]).

Duggin[41] determined the coefficient of variation of the global irradiance about a diurnally varying value for several days' measurements

for selected wavelengths and for the Landsat MSS bandpasses. The data were pooled over several days, and the summary results are shown in Table 7.

As shown by Duggin[41,58], the 95% confidence interval on the detected mean radiance difference between n pixel pairs in targets P and Q is:

$$\left[(\bar{L}_r)_P - (\bar{L}_r)_Q\right] \pm HW\left[(\bar{L}_r)_P - (\bar{L}_r)_Q\right] \quad -(1)$$

where $(\bar{L}_r)_P$ = mean radiance detected from n pixels in target P

$(\bar{L}_r)_Q$ = mean radiance detected from n pixels in target Q

$$HW\left[(\bar{L}_r)_P - (\bar{L}_r)_Q\right] = \frac{t_{0.5,m}}{\sqrt{n}}\left\{\left[\sigma\,(L_r)_P\right]^2 + \left[\sigma\,(L_r)_Q\right]^2\right\}^{\frac{1}{2}} \quad -(2)$$

where (e.g.) $\sigma\,(L_r)_P$ denotes standard deviation of the radiance $(L_r)_P$ from a pixel in target P and HW denotes half the width of the 95% confidence interval on the difference $\left[(\bar{L}_r)_P - (\bar{L}_r)_Q\right]$. In order to separate the targets P and Q with a 95% confidence of being correct, on the basis of the difference between the mean radiances, then $\left[(\bar{L}_r)_P - (\bar{L}_r)_Q\right]$ must be equal to or greater than $HW\left[(\bar{L}_r)_P - (\bar{L}_r)_Q\right]$. $t_{0.5,m}$ is the student factor, where (m + 1) is the number of observations used in estimating $\sigma\,(L_r)_P$ and $\sigma\,(L_r)_Q$. Here, the larger the variability in the radiance reaching the sensor from target P or from target Q in bandpass r, the larger the value of $HW\left[(\bar{L}_r)_P - (\bar{L}_r)_Q\right]$.

Now $L_r = \left\{ E_r \cdot \frac{\rho_r}{\pi} \cdot \tau_r + (L_{path})_r \right\}$ -(3)

(e.g.[41])

where L_r = detected radiance in bandpass r

ρ_r = bidirectional reflectance in bandpass r

τ_r = atmospheric transmission in bandpass r

$(L_{path})_r$ = atmospheric backscatter (path radiance) in bandpath r

and E_r = global irradiance in bandpass r

So if path radiance across the scene is assumed constant and if the coefficient of variation (standard deviation divided by the mean) of solar irradiance on the target is assumed approximately equal to the coefficient of variation of the atmospheric transmission, then (assuming that the path radiance is approximately constant): -

$$\left[\frac{\sigma(L_r)}{(\bar{L}_r)} \right]^2 \simeq 2 \left[\frac{\sigma(E_r)}{\bar{E}_r} \right]^2 + \left[\frac{\sigma(\rho_r)}{\bar{\rho}_r} \right]^2 \qquad -(4)$$

and (2) and (4) give

$$HW\left\{(\bar{L}_r)_P - (\bar{L}_r)_Q\right\} = \frac{t_{0.5,m}}{\sqrt{n}} \left\{ (\bar{L}_r)_P^2 \left[2 \left(\frac{\sigma(E_r)}{\bar{E}_r} \right)^2 + \left(\frac{\sigma(\rho_r)}{\bar{\rho}_r} \right)_P^2 \right] \right.$$

$$\left. + (\bar{L}_r)_Q^2 \left[2 \left(\frac{\sigma(E_r)}{\bar{E}_r} \right)^2 + \left(\frac{\sigma(\rho_r)}{\bar{\rho}_r} \right)_Q^2 \right] \right\}^{\frac{1}{2}} \qquad -(5)$$

which is the minimum necessary radiance difference at the sensor for a discrimination of P and Q (on the basis of the difference in mean pixel radiance in bandpass r) with a 95% confidence of being correct.

In the computation of vegetative indices (VINs), combinations of radiance values in different bandpasses are used. These are either additive or multiplicative, or a combination of both. It is our purpose in this section to discuss the difference in VIN which must exist before two vegetated areas may be said to differ with a 95% confidence on the basis of the difference in VIN.

The differences in VIN which must exist between groups of n pixels in two vegetated targets before the canopies may be said to differ (e.g. healthy vs. stressed) will depend upon the variability of the surface reflectance and upon the variability of the irradiance upon the ground target. Over uniform target areas, discrimination will be more accurately performed for large numbers of pixels located in each target area.

As was pointed out in the previous section, the spectral reflectance indicatrix depends strongly on the sun-target-sensor geometry. This means that the variations in reflectance properties of the surface could vary from one set of angular conditions to another: $\left[\frac{\sigma(\rho_r)}{\bar{\rho}_r}\right]$ could well depend upon solar zenith and azimuth angle and upon scanner look angle for any bandpass, altering HW $\left[(\bar{L}_r)_P - (\bar{L}_r)_Q\right]$. Insufficient data exist to explore this possibility at present.

Equation (5) deals with target separability on the basis of radiance falling on the sensor. However, it has been pointed out above

that the spectral response of the sensor across its nominal bandpass interacts with the spectral response of the target. Therefore, strictly speaking, equation (5) would need to be rewritten so that the detector outputs were considered, rather than radiance incident on the detector. The purpose of this section is to demonstrate the relative importance of surface reflectance variability and atmospheric variability in determining minimum necessary differences in scene (upwelling) radiance at the sensor to produce differences in sensor output adequate for target discrimination (with a 95% confidence). We therefore consider the sensor-target interaction to determine whether despite these interactions and variations, detection and quantification of vegetative disease severity is feasible using Landsat digital remotely sensed data. Similar approaches would be applicable to any sensor.

Calculations have been performed using reflectance measurements made with a pair of calibrated Exotech model GTR-100 radiometers on agricultural targets (e.g.[57]).

The sampled area was 1 m in diameter in each case and sampled areas were 80 m apart in order to make it possible to relate the variability of the ground data to the Landsat MSS data. The target was an agricultural area in NSW which was measured as part of a previous experiment. Tables 8-10 show the hemispherical-conical reflectance values in each band and the number of observations (n) from which the mean and coefficient of variation (standard deviation divided by the mean) are calculated.

It may be seen that the coefficient of variation (C.V.) of the reflectance is typically about 10% in MSS 4-7. It may be that the coefficient of variation might decrease with a larger sampling area. However, it is interesting to note that the C.V.'s in spectral reflectance factors (hemispherical-conical) reported by Duggin[41] for a sandstone target are of the same order of magnitude, although he used spectroradiometers with 25 nm bandpass, rather than fixed band radiometers. It is, therefore, likely that these figures may be bandpass-independent to a first order of approximation.

Relative, mean normalized sensor output values (NS_r) were calculated (using the method of (e.g.) Duggin, Slater and Somers[44] for the Landsat-3 multispectral scanner (MSS) viewing at nadir (zero scan angle) soybean targets affected with rust at different levels of severity (Casey and Duggin, unpublished data). The means of the values calculated for the six different channels (each with its own spectral response) in each of the different bandpasses were considered. The relative VIN values shown in Table 11 were obtained for a 45^{o} solar zenith angle: a clear (perfectly transmitting) atmosphere was assumed. These data may be used to calculate the difference in recorded digital VIN values over healthy and unhealthy soybean targets which would be required to perform a target discrimination with a 95% probability of being correct. It was assumed that 30 adjacent pixels were filled with each target.

For discriminations using a vegetative index, equation (5) may be written as equation (6) where the VIN is a combination of recorded radiance in MSS 5 and MSS 7 (MSS 7/MSS 5). The coefficient of variation of

reflectance in both bands is approximately 0.10 (from Tables 2-4), and the irradiance variability is derived from that obtained in MSS bands 5 and 7 (Table 1) for an accumulation of several days' data.

$$HW\left\{\overline{VIN(P)-VIN(Q)}\right\} = \frac{t_{0.05,29}}{\sqrt{30}}\left\{\left(\overline{(VIN(P)}\right)^2\left[A+B_P\right] + \left(\overline{VIN(Q)}\right)^2\left[A+B_Q\right]\right\}^{\frac{1}{2}} \qquad -(6)$$

Here, P refers to the healthy soybean target and Q refers to the stressed soybean target.

$$\text{where } A = 2\left\{\left(\frac{\sigma(E_5)}{\bar{E}_5}\right)^2 + \left(\frac{\sigma(E_7)}{\bar{E}_7}\right)^2\right\}$$

if E_5 = irradiance in MSS band 5 (600-700 nm)

and E_7 = irradiance in MSS band 7 (800-1100 nm)

and where, if ρ_5 = (hemispherical-conical) reflectance in MSS band 5, while

ρ_7 = reflectance in MSS band 7.

$$B_P = \left[\left(\frac{\sigma(\rho_5)}{\bar{\rho}_5}\right)^2 + \left(\frac{\sigma(\rho_7)}{\bar{\rho}_7}\right)^2\right]_P$$

$$B_Q = \left[\left(\frac{\sigma(\rho_5)}{\bar{\rho}_5}\right)^2 + \left(\frac{\sigma(\rho_7)}{\bar{\rho}_7}\right)^2\right]_Q$$

$$\text{Let } \left(\frac{\sigma(\rho_5)}{\bar{\rho}_5}\right)_P = \left(\frac{\sigma(\rho_7)}{\bar{\rho}_7}\right)_P = \left(\frac{\sigma(\rho_5)}{\bar{\rho}_5}\right)_Q = \left(\frac{\sigma(\rho_7)}{\bar{\rho}_7}\right)_Q \approx 0.10$$

Then $B_P = B_Q = 2 \left[\frac{\sigma(\rho_5)}{\bar{\rho}_5} \right]_P^2 = 2 \times 10^{-2}$

and $A = 2 \left\{ (.0405)^2 + (.0731)^2 \right\} = 1.397 \times 10^{-2}$,

using for data in Table 11, $t_{0.05,29} = 2.00$.

In Table 12, we show the VIN (MSS 7/MSS 5) differences which were calculated to exist between soybean canopies with different rust severity levels. We also show the calculated minimum necessary differences for rust severity discrimination at the 95% confidence level, using VINs calculated for the mean radiance from 30 pixels in each severity region. One may conclude that rust severity discrimination and quantification, at least for the soybean targets considered here, is indeed possible at the 95% confidence level using Landsat VIN data.

However, the important conclusion is that there is an excellent chance that stress (in this case rust in the soybean canopy) can (at least in some cases) be detected using Landsat data. It is likely that the augment would be similarly successful if applied to the AVHRR data (assuming that the stressed area is large enough to detect). There is a possibility of stress quantification. More work needs to be done for various targets and for various sun-target-sensor geometries.

8. The effect of unresolved (sub-pixel sized) cloud on recorded radiance.

While the presence of cloud can increase the radiance levels in the individual bandpasses in the visible and in the reflective infrared regions, a decrease in temperature is recorded in the mid-infrared region as may be seen for example in Fig. 45. Indeed, temperature is one of the methods of measuring the presence of cloud; and it is anticipated that by studying simultaneously the visible, reflective and mid-infrared region for each pixel, progress will be made in the detection of sub-pixel-sized (i.e. of unresolved) cloud.

Unresolved cloud can cause difficulties in mapping and quantifying ground features. Since cloud detection algorithms are successful only for levels of cloud contained within a pixel which exceed a certain value, undetected cloud and haze can distort the level and the spectral (i.e. between-channel) distribution of radiance from targets. That is, unresolved cloud can alter the radiance at wavelength λ from a given pixel, because unresolved cloud can alter the apparent reflectance factor of the ground area imaged within a pixel in the manner described by the following equation.

$$R(z,\phi;\theta',\phi',\lambda) = \left\{ \sum_m R(z,\phi;\theta',\phi',\lambda)_m \times a_m \right\} \times (1-a_{cloud}) + R(\lambda)_{cloud} \times a_{cloud} \qquad -(2)$$

where $R(z,\phi;\theta',\phi',\lambda)$ is the effective overall spectral hemispherical-conical reflectance factor for the pixel for the sun-target-sensor geometry shown in Fig. 1 and where there are m components (cover types) at ground level, each with a spectral hemispherical-conical reflectance factor (for the same geometry) $R(z,\phi;\theta',\phi',\lambda)$ and each of which occupies a proportion

(fraction) of the pixel a_m at ground level. The ground area giving rise to the pixel under consideration is partly covered by an intervening layer of cloud, with diffuse (and, therefore, geometrically independent) spectral reflectance factor $R(\lambda)_{cloud}$. The cloud covers a fraction a_{cloud} of the discussed pixel. While it may not be exactly correct to refer to clouds as strictly diffuse (i.e. Lambertian) reflectors, it is a close approximation.

Equation (2) shows, on substitution into equation (1) (section 4), that the greater the percentage of the pixel covered by cloud, the higher the overall radiance levels. However, in the case of vegetation, due to the far lower reflectance of the plant canopy in the visible part of the spectrum than in the reflective infrared, the presence of cloud can alter the ratio of the apparent near infrared reflectance to the visible red reflectance of the area included within a pixel. Since vegetation is frequently monitored on a repetitive basis using satellite scanner data, methods have been developed by which combinations of radiance recorded in different scanner channels are combined into a "vegetation index". Such an index is not only sensitive to the nature and vigor of vegetation, but because it is unidimensional data, it is also simpler (and cheaper) to analyze (for repeated coverage of large areas) than multichannel data clustered in multidimensional feature space.

The vegetative index

$$VIN\ 1 = \{AVHRR\ 2 - AVHRR\ 1)\}$$

has been used[59] to screen the AVHRR digital radiance data in AVHRR bands

1 and 2 for cloud. When cloud is present, to the extent that it largely fills the IFOV or the sensor (pixel), VIN 1 becomes negative. However, calculations for nadir viewing show that for a clear atmosphere and for targets consisting only of wheat, VIN 1 will not become zero until 33% of the IFOV is filled with cloud. This figure becomes 39% for a turbid atmosphere. For a target consisting of 70% wheat and 30% soil, the percentages of the FOV which must be filled with cloud to make VIN 1 zero are 24% for a clear (meteorological range >50 km) atmosphere and 31% for a turbid (meterorological range <10 km) atmosphere. This is shown in Fig. 46. For small percentages of cloud contamination in the AVHRR IFOV (1 km x 1 km at nadir), there can be a very substantial change produced in the spectral signature of the recorded radiance. Calculations of VIN 1 performed for a range of view zenith (scan) angles are shown in FIg. 47 (clear atmosphere) and Fig. 48 (turbid atmosphere). For a clear atmosphere and a target which is 100% wheat, substantial decreases (over 30% at nadir) are caused by each 10% of the FOV obscured by cloud. The effect is even worse (over 60% at nadir) for a target which is composed of 70% wheat and 30% soil. The effects for a turbid atmosphere are seen (Fig. 48) to be as great. The scan angle effect for a clear atmosphere is assymetric about nadir and causes an increase of up to approximately 50% above the nadir value at $\theta' = \pm 54^{o}$. Atmospheric turbidity reduces this effect.

A commonly used vegetative index is, as mentioned earlier,

$$\text{VIN 2} = \left\{\frac{\text{AVHRR 2} - \text{AVHRR 1}}{\text{AVHRR 2} + \text{AVHRR 1}}\right\}$$

Figs. 49 and 50 show the effects of both a clear and turbid atmosphere and scan angle on this vegetative index, calculated in each case for a

pure wheat and for a 70% wheat, 30% soil target. For a clear atmosphere (Fig. 49), the presence of 20% cloud produces a five-fold decrease, or worse, in vegetative index at all scan angles for both the pure and for the mixed targets. Fig. 50 shows that for a turbid atmosphere, the effect is almost as bad, although atmospheric turbidity has reduced the apparent scan-angle effect in the recorded signal. Less than 25% of cloud in a pixel will not be detected during screening of the AVHRR data, using VIN 1, despite the large effects of such cloud on the vegetative indices. Effects on VIN 1 and VIN 2 due to sub-pixel sized cloud can give rise to substantial errors in assessment of ground cover type and conditions.

While the above findings are provocative, they refer to only two targets. More calculations and comparison with experimental data is required. Further work could definitely help develop algorithms to screen out cloud and haze. Clearly, the effect of variable quantities of unresolved cloud and haze will be the same as random variations in target radiance, caused by random variations in irradiance on the target and reflectance of the target.

9. Simulation Studies: Findings

Using equation (1), calculations were performed for the wheat canopy at growth stages 3.5 (boot) and 4.5 (fully headed) on the modified Feeks scale. Reflectance factor data was obtained from the LARSPEC data files[49,60] for sun-target-sensor geometries equating to NOAA-6 and to NOAA-7 overpass times.

The results of the calculations of sensor output are shown in Figs. 51-74 for the AVHRR radiance values. Discontinuities in the predicted sensor output at nadir are due to errors within the LARSPEC data, since the values were obtained from measurements made at different times.

The trends in simulation studies are generally the same as those observed empirically in the radiance data. In order to draw detailed conclusions from this approach, it will be necessary to have reflectance factor data from mathematical models of vegetation canopy, which have been calibrated using experimental data. In this case, it would be possible to compute predictive contrast ratios between the target and its surroundings for various AVHRR geometries. However, much more work is needed here which could usefully form the basis of a further task.

However, certain conclusions may be drawn from the study:

1. There is a scan-angle dependence of the digital radiance data recorded in each AVHRR channel.
2. The sensor output is sensor dependent. In other words, the output of the NOAA-6 and -7 AVHRR's over the same target will differ (due to the different sensor spectral responses).
3. There appears to be a growth-stage dependence of the scan-angle dependence of sensor output. This would suggest that any

empirical data normalization algorithms would need to have a factor allowing for growth stage.

4. There is a strong angle dependence of the VIN1 = (AVHRR 2 - AVHRR 1) which is used at present for screening out cloud from the AVHRR digital data in pre-processing. This will further reduce the value of this algorithms for screening cloud from an image.

5. The VIN2 = $\left\{\frac{\text{AVHRR 2 - AVHRR 1}}{\text{AVHRR 2 + AVHRR 1}}\right\}$ is growth stage dependent, is scan angle dependent and is dependent on atmospheric turbidity.

10. Conclusions and Recommendations

There is a present need to operationally use NOAA AVHRR data to map and to monitor vegetation types and conditions in near-real time. This task can be greatly enhanced if it is possible to use a greater portion of each GAC image than the central 25% now in use. Empirical and simulation studies suggest that an enlargement of the "cloud-free" image data set will permit the development of a series of correction algorithms, by means of which the digital scanner imagery may be corrected for ground reflectance and for atmospheric scattering anisotropy, within certain accuracy limits. The acquisition of a larger data set will provide an estimate of the accuracy limits.

The sensor outputs, representing recorded radiance values in spectral bandpasses defined by AVHRR 1, AVHRR 2 are not only scan angle dependent, but are also dependent on growth stage and on sensor spectral response. Therefore, any empirical correction algorithms used to normalize the digital radiance or VIN data will need to contain factors for growth stage and for instrument spectral response.

There is a need to improve the screening algorithms for cloud, since presently used algorithms still do not screen out pixels which are contaminated by cloud and which can, therefore, show vegetation indices distorted by factors of over two. The algorithm presently used to screen cloud has been shown in simulation studies to be strongly scan angle dependent, which thus reduces its value.

While it may be possible to normalize out systematic effects in AVHRR data, it is not possible to correct in any way for random functuations in target radiance. However, it is possible to estimate the

necessary radiance difference between targets in order to be able to provide target discrimination and quantification within pre-determined limits of accuracy. More work is needed in this area in order to be able to estimate the target dependence and scan angle dependence of the radiance difference needed to discriminate and to quantify targets with pre-determined confidence limits.

Due to difficulties in obtaining time on the USDA computer in Houston, since there are many operational demands on this installation, a larger image data set will be examined than has previously been possible. We shall use a contract facility. Not only will swaths across the GAC images be examined, but further selected targets will also be examined from different view angles by using sequential overpass data. NASA/USDA will provide copies of the GAC data for this purpose.

There is a need to determine to what extent selected vegetation targets can be identified and their condition quantified using digital AVHRR data, given that systematic error correction will not be precise and that random errors occur in the AVHRR data. This problem should be examined using appropriate statistical methods.

A major difficulty exists in lack of documentation of pre-processing algorithms used on AVHRR digital data. This resulted in extra time taken in this project due to a misconception of those algorithms which it was thought had been used. It is respectfully suggested that this area might receive attention.

11. Acknowledgements

We wish to acknowledge technical assistance from Gene Ryland, drafting assistance of Maggie Duggin and typing assistance of Joyce Carpenter.

12. REFERENCES

1. Bauer, M.E., L.L. Biehl, C.S.T. Daughtry, B.F. Robinson and E.R. Stoner (1979). AgRISTARS Supporting Research, Final Report NAS9-15466, vol. 1.

2. Lunnik, N.J.J. and W. Verhoef (1974). NIWARS Publ. No. 23, Delft, The Netherlands.

3. Chance, J.G. and E.W. LeMaster (1977). "Suits reflectance models for wheat and cotton: theoretical and experimental tests". Appl. Optics 16,407.

4. Chance, J.E. and E.W. LeMaster (1978). "Plant canopy light absorption model with application to wheat". Appl. Optics 17, 2629-2636.

5. Colwell, J.E. (1974). "Vegetation canopy reflectance". Remote Sens. Environ. 3, 175-183.

6. Coulson, K.L. (1966). "Effects of reflection properties of natural surfaces in aerial reconnaissance". Appl. Optics 5, 905-917.

7. Coulson, K.L., G.M. Bouricius and E.L. Gray (1965). "Optical reflection properties of natural surfaces". J. Geophysical Res. 70, 4601-4611.

8. Egbert, D.D. and F.T. Ulaby (1972). "Effects of angles on reflectivity". Photogrammetric Eng. 38, 556-564.

9. Duggin, M.J. (1977). "Likely effects of solar elevation on the quantification of changes in vegetation with maturity using sequential Landsat imagery". Appl. Optics 16, pp. 521-523.

10. Kollenkark, J.C., V.C. Vanderbilt, C.S.T. Daughtry and M.E. Bau (1982). "Influence of solar illumination angle on soybean canopy reflectance". Appl. Optics, 21, 1179-1184.

11. Robinson, B.F. and L.L. Biehl (1979). "Calibration procedures for measurement of reflectance factor in remote sensing field research". SPIE Vol. 196 Measurements of Optical Radiations, 16-26.

12. Suits, G.H. and G. Safir (1972). "Verification of a reflectance model for mature corn with applications to corn blight detections". Remote Sens. Environ. 2, 183.

13. Smith, J.A. (1979). MRS Literature Survey of bidirectional reflectance. ORI, Inc., 1400 Spring Rd., Silver Spring, Md.

14. Berry, J.K. and J.A. Smith (1977). "An overview of vegetation canopy modelling for signature correction and analysis". 4th Annual Symp. on Machine Processing of Remotely Sensed Data, p. 194.

15. Smith, J.A. and L.E. Oliver (1972). "Plant canopy models for simulating composite scene spectroradiance in the 0.4 to 1.05 micrometer region". Proc. Eighth Internat. Symp. on Remote Sensing of Environ., Ann Arbor, MI., 1333-1353.

16. Suits, G.H. (1972). "The calculation of the directional reflectance for a vegetative canopy", Remote Sens. Environ. 2, 117.

17. Suits, G.H. (1972). "The causes of azimuthal variations in directional reflectance of vegetative canopies", Remote Sens. Environ. 2, 175.

18. Verhoef, W. and N.J.J. Bunnik (1976). "The spectral directional reflectance of row crops. Part 1: Consequences of non-Lambertian behavior for automatic classification. Part 2: Measurements on wheat and simulations by means of a reflectance model for row crops." Tech. Rpt. No. NIWARS-Publ. 35. NIWARS, Delft, The Netherlands.

19. Valley, S.L., ed. (1965). Handbook of Geophysics and Space Environments, Air Force Cambridge Research Lab., Bedford, MA.

20. Kriebel, K.T. (1976). "On the variability of the reflected radiation field due to differing distributions of the irradiation". Remote Sensing Environ. 4, 257-264.

21. Kriebel, K.T. (1977). "Reflection properties of vegetated surfaces: tables of measured spectral biconical reflectance factors". Universitat Munchen - Meterorologisches Inst. Wissenschaftliche Mietteilung, Nr 29.

22. Kirchner, J.A., S. Youkhana and J.A. Smith (1982). "Influence of sky radiance distribution on the ratio technique for estimating bidirectional reflectance". Photogrammetric Eng. and Remote Sens. 48, 955-959.

23. Rogers, R.H. and K. Peacock (1973). "A Technique for correcting ERTS data for solar and atmospheric effects". Symp. on Significant Results Obtained from the Earth Resources Technology Satellite - 1, March. NASA SP-327, Vol. 1, p. 1115.

24. Rogers, R.H. (1973). "Investigation of Techniques for correcting ERTS data for solar and atmospheric effects". Bendix Aerospace Systems Div., Rept. MNC 655, October.

25. Ellis, P.E. and M.J. Duggin (1978). "Atmospheric measurements" in Landsat 2 Over New Zealand: Monitoring our Resources from Space. New Zealand Department of Scientific and Industrial Research DSIR Bulletin 221, pp. 83-101.

26. Kowalik, W.S. (1981). Ph.D. Thesis, "Atmospheric Correction to Landsat data for limonite discrimination", Stanford University, 363 pp.

27. Switzer, P., W.S. Kowalik and R.J.P. Lyon (1981). "Estimation of atmospheric path radiance by the covariance matrix method", Photogramm. Eng. and Remote Sensing 47, 1469-1476.

28. Potter, J.F. and M.A. Mendlowitz (1975). "On the determination of haze levels from Landsat data". Proc. Tenth Int. Symp. on Remote Sensing of Environ., Ann Arbor, MI., pp. 695-703.

29. Potter, J.F. (1977). "The correction of Landsat data for the effects of haze, sun angle and background reflectance". Proc. Symp. on Machine Processing of Remotely Sensed Data, IEEE 77Ch 1218-7MPRSD, June, pp. 24-32.

30. Turner, R.E. (1978). "Elimination of atmospheric effects from sensor data". Proc. 12th Int. Symp. on Remote Sensing of Environ., Ann Arbor, MI., pp. 783-793.

31. Turner, R.E., W.A. Malila and R.F. Nalepka (1971). "Importance of atmospheric scattering in remote sensing". Proc. 7th Int. Symp. on Remote Sensing of Environ., Ann Arbor, MI., pp. 1651-1697.

32. Otterman, J. and R.S. Fraser (1976). "Earth-atmosphere system and surface reflectivities in arid regions from Landsat MSS data." Remote Sensing of Environ. 5, 247-266.

33. Fraser, R.S., Bahethi, Om. P., Al-Abbas, A.H. (1977). "The effect of the atmosphere on the classification of satellite observation to identify surface features". Remote Sensing of Environ. 6, 229-249.

34. Herman, B.M. and S.R. Browning (1975). "The effect of aerosols on the earth-atmospheric albedo", J. Atmos. Sci. 32, 1430.

35. Johnson, W.R. and M.L. Sestak (1981). AgRISTARS Report NASA SR-LI-04071; JSC-17127.

36. Dave, J.V. (1978). "Extensive data sets of the diffuse radiation in realistic atmospheric models with aerosols and common absorbing gases". Solar Energy 21, 361-369.

37. Dave, J.V. and J. Canosa (1974). "A direct solution of the radiactive transfer equation: application to atmospheric models with arbitrary vertical nonhomogeneities", J. Atmos. Sci. 31, 1089-1101.

38. Dave, J.V. (1975). "A direct solution of the spherical harmonics approximation to the radiative transfer equation for an arbitrary solar elevation. Part 1: theory". J. Atmos. Sci. 32, 790-798.

39. Dave, J.V. (1980). "Simulation colorimentry of the earth-atmosphere system". Remote Sensing of Environ. 9, 301-324.

40. Slater, P.N. (1980). Private communication.

41. Duggin, M.J. (1974). "Target differentiation using spectral discrimination techniques". Proc. 9th Internat. Symp. on Remote Sensing of Environ., Ann Arbor, MI., 499-515.

43. Park, S.K., R.E. Davis, F.O. Huck and R.F. Arduini (1980). "Multispectral data acquisition and classification: computer modelling for smart sensor design". Proc. AIAA Conf. "Sensor Systems for the 80's", Colorado Springs, CO., Dec. 2-4, 47-56.

44. Duggin, M.J., P.N. Slater and S.L. Somers (1980). "A method for calibrating multispectral scanners to allow for the spectral dependence of instrument response", Proc. AIAA Conf., "Sensor Systems for the 80's", Colorado Springs, CO., Dec. 2-4, 76-83.

45. Chance, J.E. (1981). "Crop identification and leaf area index calculations with Landsat multitemporal data". Int. J. Remote Sensing 2, 1-14.

46. Schnetzler, C.C. (1981). "Effect of sun and sensor geometry, canopy structure and density and atmospheric conditions on the spectral response of vegetation, with particular emphasis on across-track pointing". Proc. Conf. "Signatives Spectrales d'objets en teledetection", Avignon 8-11 Sept., pp. 509-520.

47. Kirchner, J.A. and C.C. Schnetzler (1981). "Simulated directional radiances of vegetation from satellite platforms". Int. J. Remote Sensing 2, 253-264.

48. Duggin, M.J. (1980). "Effect of instrument spectral response on use of the Landsat MSS for vegetative disease assessment", Appl. Optics 19, 2081-2083.

49. Bauer, M.E., L.L. Biehl, C.S.T. Daughtry, B.F. Robinson and E.R. Stoner (1979). AgRISTARS Supporting Research: Final Report, NAS 9 - 154-66, Vol. 1.

50. Kaneko, T. and J.L. Engvall (1977). "View angle effect in Landsat imagery". Proc. 11th Internat. Symp. on Remote Sensing of Environ., Ann Arbor, MI. 945-951.

51. Duggin, M.J., D. Piwinski, V. Whitehead and G. Ryland. "Evaluation of NOAA-AVHRR data for crop assessment". Appl. Optics 21, 1873-1875.

52. Tappan, G. and G.E. Miller (1982). "Area Estimation of environmental phenomena from NOAA-n satellite data". AgRISTARS Report EW-L1-04190, NASA doc. JSC-17437, 12 pp. plus appendices.

53. Perry, C. (1982). Private communication.

54. Lautenschlager, L.F. and C. Perry (1981). Proc. Survey Research Methods Section of Amer. Statistician Assn., Washington, D.C.

55. Blystone, R. and M.J. Duggin (1980). "On the analysis of remote sensing data to predict selected vegetative variables". Proc. ASP Fall Technical Meeting, Niagara Falls, October, RS-2-B-1 to RS-2-B-11.

56. Whitehead, V. (1982). Private communication.

57. Duggin, M.J. (1980). Photogrammetric Eng. and Remote Sensing 46, 643-647.

58. Duggin, M.J. (1982). To appear in Int. J. Remote Sensing.

59. Ravet, F. (1981). Private communication.

60. Biehl, L. (1982). Private communication.

13. TABLES

	Title	Page No.
1.(a)	Typical values of atmospheric extinction optical thickness for a clear atmosphere (meteorological range >50 km) and for a turbid atmosphere (meteorological range < 10 km)	
1.(b)	Path radiance calculated for various view zenith (scan) angles (θ') for both the upsun ($(\phi'-\phi)=0^{o}$) and for the downsun ($(\phi'-\phi)=180^{o}$) positions	
2.	Images used in empirical analysis of digital AVHRR data	
3.	Best fit curve for GAC mean radiance data in AVHRR 1 plotted against scan angle θ'	
4.	Best fit curve for GAC mean radiance data in AVHRR 2 plotted against scan angle θ'	
5.	Best fit curves for vegetative index VIN 1 from mean AVHRR data (AVHRR 2 - AVHRR 1) plotted against scan angle θ'	
6.	Best fit curve for vegetative index VIN 2 from mean AVHRR data $\left\{\frac{\text{AVHRR 2 - AVHRR 1}}{\text{AVHRR 2 + AVHRR 1}}\right\}$ plotted against scan angle θ'	
7.	The average values for coefficients of variation of global irradiance	
8.	Coefficient of variation (%) of measured hemispherical-conical reflectance factor in MSS bandpasses approx. 8 weeks before harvest	
9.	Coefficient of variation (%) of measured hemispherical-conical reflectance factor in MSS bandpasses approx. 5 weeks before harvest	
10.	Coefficient of variation (%) of measured hemispherical-conical reflectance factor in MSS bandpasses approx. 3 weeks before harvest	
11.	Mean calculated sensor outputs and VIN (=MSS 7/Mss 5) for the Landsat-3 MSS when viewing a soybean target in various stages of stress	
12.	VIN (=MSS 7/MSS 5) differences calculated from simulated (MSS) sensor outputs for different rust severity levels and VIN differences which would be necessary for discrimination at the 95% level of confidence	

14. FIGURE CAPTIONS

1. Geometric nomenclature in consideration of reflectance properties.

2. Spectral reflectance factor of wheat at growth stage 3·5. (Boot). NOAA-6-AVHRR geometry: upsun viewing (i.e., looking towards sun).

3. Spectral reflectance factor of target in Fig. 2, but for downsun viewing (i.e., looking away from sun). NOAA-6-AVHRR geometry.

4. Spectral reflectance factor of wheat at growth stage 3·5 (Boot). NOAA-7-AVHRR geometry: upsun viewing.

5. Spectral reflectance factor of wheat at growth stage 3·5 (Boot). NOAA-7-AVHRR geometry: downsun viewing.

6. Spectral reflectance factor of wheat at growth stage 4·5. NOAA-6 AVHRR geometry: upsun viewing.

7. Spectral reflectance factors of wheat at growth stage 4·5. NOAA-6 AVHRR geometry: downsun viewing.

8. Spectral reflectance factor of wheat at growth stage 4·5. NOAA-7 AVHRR geometry: upsun viewing.

9. Spectral reflectance factor of wheat at growth stage 4·5. NOAA-7 AVHRR geometry: downsun viewing.

+

+

+

+

14a. Solar zenith angle dependence of spectral global irradiance.

14b. Solar zenith angle dependence of ratio of diffuse to total spectral global irradiance.

15. Wavelength-dependence of factors controlling remotely sensed radiance.

16. Spectral response curves of first two bandpasses of NOAA-6 AVHRR.

+ Figures 10-13 omitted as policy decision during final collation.

17. Simulated sensor output for NOAA-6 AVHRR at various scan angles. Target is wheat at growth stage 4·5. Vegetative index shown is

$$\left\{\frac{\text{AVHRR 2 - AVHRR 1}}{\text{AVHRR 2 + AVHRR 1}}\right\}$$

18. Observed mean radiance variation across image; obtained using 50 averaged, sequential bands of GAC (global area convage) data. Images used were obtained on a clear day.

19. Observed mean radiance variation across images; obtained using 50 averaged, sequential bands of GAC data. Some cloud and haze present on image.

20 - 43. Sets of 4 sequential curves for observed mean radiance obtained by averaging 50 sequential scan lines of GAC data and presenting the mean of each 8 sequential GAC pixel radiance or VIN values plotted as a function of scan angle θ' expressed in radians. The sequence consists (respectively) of radiance recorded in AVHRR 1, radiance recorded in AVHRR 2, VIN 1 = (AVHRR 2 - AVHRR 1) and VIN 2 = $\left\{\frac{\text{AVHRR 2 - AVHRR 1}}{\text{AVHRR 2 + AVHRR 1}}\right\}$. There are five images which have been analyzed, constituting the first five (5) sequences of four (4) curves each, followed by a sequence of the pooled data. In each case, the best fit quadratic curve is shown on the scatter plot and the coefficients of each best-fit curve are shown on the plot.

44. Radiance recorded in AVHRR 1 and AVHRR 2, plotted as a function of scan angle. Data was obtained over the same forested target from different (sequential) images.

45. Scan angle dependence of first three bands of the NOAA AVHRR.

46. VIN 1 = (AVHRR 2 - AVHRR 1) simulated for view angle = 0 (nadir) for a pure wheat and for a 70% wheat, 30% soil target for various percentages of the pixel filled by cloud. Both clear and turbid atmospheres are considered.

47. VIN 1 = (AVHRR 2 - AVHRR 1) calculated for both pure wheat and 70% wheat, 30% soil targets. A clear atmosphere is considered and the effects of scan angle are shown for various percentages of pixel obscured by cloud.

48. VIN 1 = (AVHRR 2 - AVHRR 1) calculated for both pure wheat and 70% wheat, 30% soil targets. A turbid atmosphere is considered and the effects of scan angle are shown for various percentages of pixel obscured by cloud.

49. VIN 2 = $\frac{\text{AVHRR 2 - AVHRR 1}}{\text{AVHRR 2 + AVHRR 1}}$ calculated for both pure wheat and 70% wheat, 30% soil targets. A clear atmosphere is considered and the effects of scan angle are shown for various percentages of pixel obscured by cloud.

50. VIN 2 = $\frac{\text{AVHRR 2 - AVHRR 1}}{\text{AVHRR 2 + AVHRR 1}}$ calculated for both pure wheat and 70% wheat, 30% soil targets. A turbid atmosphere is considered and the effects of scan angle are shown for various percentages of pixel obscured by cloud.

51 - 62. Simulated scan angle-dependence of wheat at various growth stages for clear (meteorological range >50 km) and for turbid (meteorogolical range <10 km) atmosphere, calculated for NOAA-6 and NOAA-7 AVHRR bands 1 and 2 as marked.

63 - 68. Simulated scan angle-dependence of (AVHRR 2 - AVHRR 1) for targets, atmospheres and sensors considered in Figs. 51-62, as marked.

69 - 74. Simulated scan angle-dependence of $\left\{\frac{\text{AVHRR 2 - AVHRR 1}}{\text{AVHRR 2 + AVHRR 1}}\right\}$ for targets, atmospheres and sensors considered in Figs. 51-62, as marked.

Table 1(a). Values of Atmospheric Extinction Optical Thickness Used

ATMOSPHERE	λ = 0.65 pm	λ = 0.90 pm
"CLEAR"	.074	.033
"TURBID"	.445	.313

Table 1(b). Path Radiance (mw cm^{-2} sr^{-1} μm^{-1})

SCAN ANGLE θ	ATMOSPHERE	λ = .650 pm		λ = .900 pm	
		∅ = 0°	∅ = 180°	∅ = 0°	∅ = 180°
5°	"CLEAR"	.894	.977	.330	.344
15°		.845	1.099	.325	.368
25°		.841	1.276	.337	.415
5°	"TURBID"	2.915	3.047	2.590	2.624
15°		2.938	3.379	2.599	2.734
25°		3.187	4.102	2.762	3.058

Table 2. Apparently Cloud-Free Images Used In Analysis.

Image I.D. No.	Figures
GAC 18.09 (lines 450-500)	20 - 23
GAC 18.10 (lines 500-550)	24 - 27
GAC 18.02 (lines 450-500)	28 - 31
GAC 18.01 (lines 500-550)	32 - 35
GAC 18.01 (lines 450-500)	36 - 39

Table 3. Best fit curves for GAC mean radiance data in AVHRR 1 plotted against scan angle ($y = a_0 + a_1x + a_2x^2$).

Image I.D. No.	a_0	a_1	a_2
GAC 18.09 (lines 450-500)	3.50	1.82	9.62
GAC 18.10 (lines 500-550)	3.91	0.662	9.79
GAC 18.02 (lines 450-500)	2.13	0.0699	4.86
GAC 18.01 (lines 500-550)	2.28	1.27	4.03
GAC 18.01 (lines 450-500)	2.73	-0.0704	5.01
Pooled Data	2.97	0.633	7.52

Table 4. Best fit curves for GAC mean radiance data in AVHRR 2 plotted against scan angle ($y = a_0 + a_1x + a_2x^2$).

Image I.D. No.	a_0	a_1	a_2
GAC 18.09 (lines 450-500)	9.22	1.59	6.40
GAC 18.10 (lines 500-550)	9.08	0.338	5.96
GAC 18.02 (lines 450-500)	5.62	-0.296	3.02
GAC 18.01 (lines 500-550)	5.76	-0.224	3.84
GAC 18.01 (lines 450-500)	6.27	-1.20	4.14
Pooled data	7.48	0.00402	5.17

Table 5. Best fit curves for VIN 1* from GAC mean radiance data plotted against scan angle ($y = a_0 + a_1x + a_2x^2$).

Image I.D. No.	a_0	a_1	a_2
GAC 18.09 (lines 450-500)	5.72	-0.227	-3.22
GAC 18.10 (lines 500-550)	5.17	-0.325	-3.83
GAC 18.02 (lines 450-500)	3.50	-0.366	-1.85
GAC 18.01 (lines 500-550)	3.48	-1.49	-0.192
GAC 18.01 (lines 450-500)	3.55	-1.13	-0.869
Pooled data	4.50	-0.629	-2.36

*VIN 1 = (AVHRR 2 - AVHRR 1)

Table 6. Best fit curves for VIN 2* from GAC mean radiance data plotted against scan angle ($y = a_0 + a_1x + a_2x^2$).

Image I.D. No.	a_0	a_1	a_2
GAC 18.09 (lines 450-500)	0.437	-0.0618	-0.431
GAC 18.10 (lines 500-550)	0.380	-0.0248	-0.419
GAC 18.02 (lines 450-500)	0.431	-0.0213	-0.391
GAC 18.01 (lines 500-550)	0.433	-0.162	-0.263
GAC 18.01 (lines 450-500)	0.411	-0.0596	-0.343
Pooled data	0.418	-0.0642	-0.378

$$*\text{VIN 2} = \left\{\frac{\text{AVHRR 2} - \text{AVHRR 1}}{\text{AVHRR 2} + \text{AVHRR 1}}\right\}$$

Table 7. The average values for coefficients of Variation of global irradiance. (Duggin 1974).41

ISCO	450 nm	600 nm	800 nm	1050 nm
$\frac{\sigma(E_r)}{\bar{E}_r}$ (8 days)	6.04%	4.54%	5.57%	6.22%

EXOTECH	MSS-1 500-600 nm	MSS-2 600-700 nm	MSS-3 700-800 nm	MSS-4 800-1050 nm
$\frac{\sigma(E_r)}{\bar{E}_r}$	3.62%	4.05%	4.68%	7.31%

Table 8. Coefficient of variation (%) of measured hemispherical-conical reflectance factor in MSS bandpasses approximately 8 weeks before harvest.

	MSS 4	MSS 5	MSS 6	MSS 7	n
Sunflower Stubble	18.8	16.7	11.3	12.1	20
Furrowed Soil	5.4	4.8	6.0	7.3	10
Sorghum Stubble	18.7	18.6	14.8	14.0	10
Fertilized Barley (a)	9.8	14.7	11.1	12.9	12
(b)	8.5	11.7	14.1	17.3	10
Unfertilized Barley (a)	9.7	12.6	6.6	7.8	10
(b)	13.1	16.9	6.1	7.7	10
Barley (Late Plant)	5.0	7.1	9.3	11.4	10
Fertilized Barley (Late Plant)	5.4	7.8	6.9	8.5	10
Grass (Sparse)	13.6	13.3	20.3	20.3	10
Pasture (Grazed)	9.0	15.5	10.3	10.6	10
Pasture (Heavily Grazed)	8.1	6.8	6.5	6.3	10

Table 9. Coefficient of variation (%) of measured hemispherical-conical reflectance factor in MSS bandpasses approximately 5 weeks before harvest.

	MSS 4	MSS 5	MSS 6	MSS 7	n
Fertilized Barley	9.3	9.1	9.4	9.5	20
Barley	14.9	16.1	4.1	14.4	20
Barley	16.6	17.6	5.1	5.5	20
Barley	11.1	11.0	5.1	6.3	20
Barley (Late Plant)	15.0	14.7	11.5	10.4	10

Table 10. Coefficient of variation (%) of measured hemispherical-conical reflectance factor in MSS bandpasses approximately 3 weeks before harvest.

	MSS 4	MSS 5	MSS 6	MSS 7	n
Fertilized Barley	8.3	8.6	4.5	4.2	16
Fertilized Barley	7.7	9.4	18.3	10.2	23
Barley	9.1	9.2	11.0	11.8	26
Barley	8.4	8.1	6.0	5.9	18
Barley	11.2	12.8	15.1	16.0	27

Table 11. Mean calculated sensor outputs and VIN (= MSS 7/MSS 5) for the Landsat - 3 MSS when viewing a soybean target* in various stages of stress.

	MSS 5	MSS 7	VIN
Healthy Soybean	69.82	430.80	6.170
Soybean 2.08% rust	79.56	330.11	4.150
Soybean 4.11% rust	80.03	315.06	3.940
Soybean 7.46% rust	81.82	288.39	3.520
Soybean 11.5% rust	93.48	211.35	2.260

*Spectral reflectance data were measured by Casey and Duggin, (unpublished data).

Table 12. VIN (= MSS 7/MSS 5) differences calculated from simulated (MSS) sensor outputs for different rust severity levels and VIN differences which would be necessary for discrimination at the 95% level of confidence.

	VIN (MSS 7/MSS 5)	Δ (VIN)	Necessary Δ (VIN) for 95% confidence of discrimination
Soybean: healthy	6.17		
		2.02	0.50
Soybean: 2.08% rust	4.15		
		0.21	0.39
Soybean: 4.11% rust	3.94		
		0.42	0.36
Soybean: 7.46% rust	3.52		
		1.26	0.28
Soybean: 11.5% rust	2.26		

Fig. 1

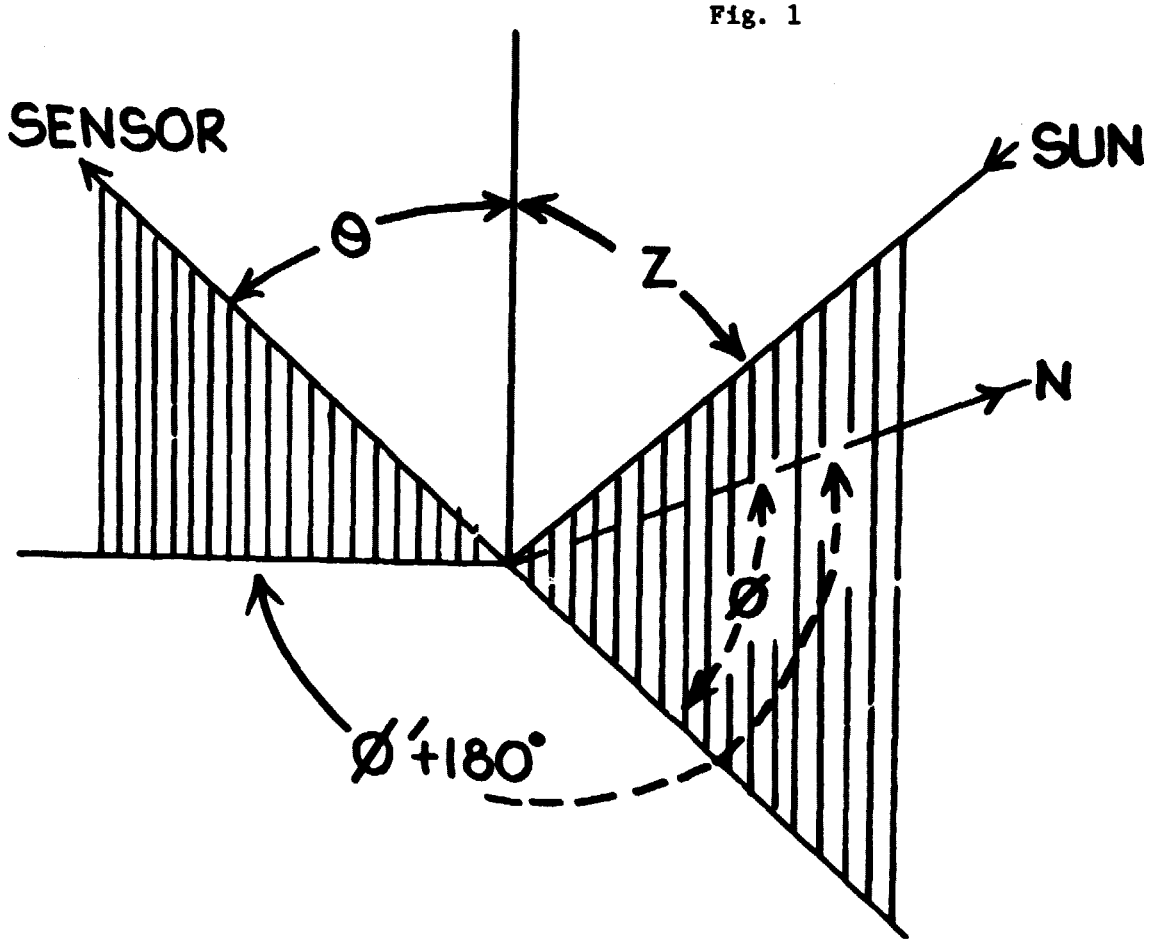

ø = solar azimuth
(ø′+180) = detector azimuth (view azimuth)
Z = solar zenith angle
θ′ = view zenith angle

Fig. 2

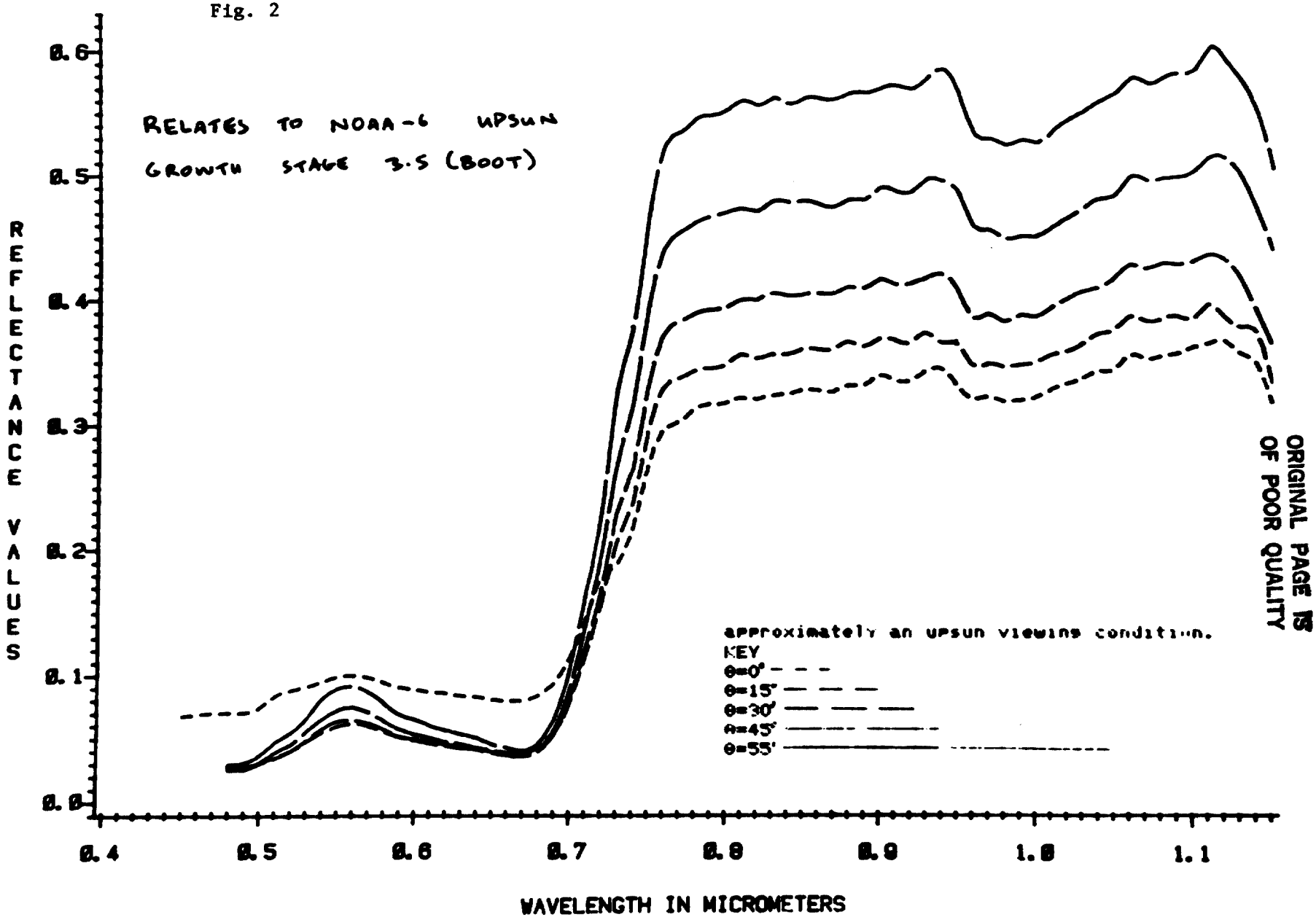

Fig. 3

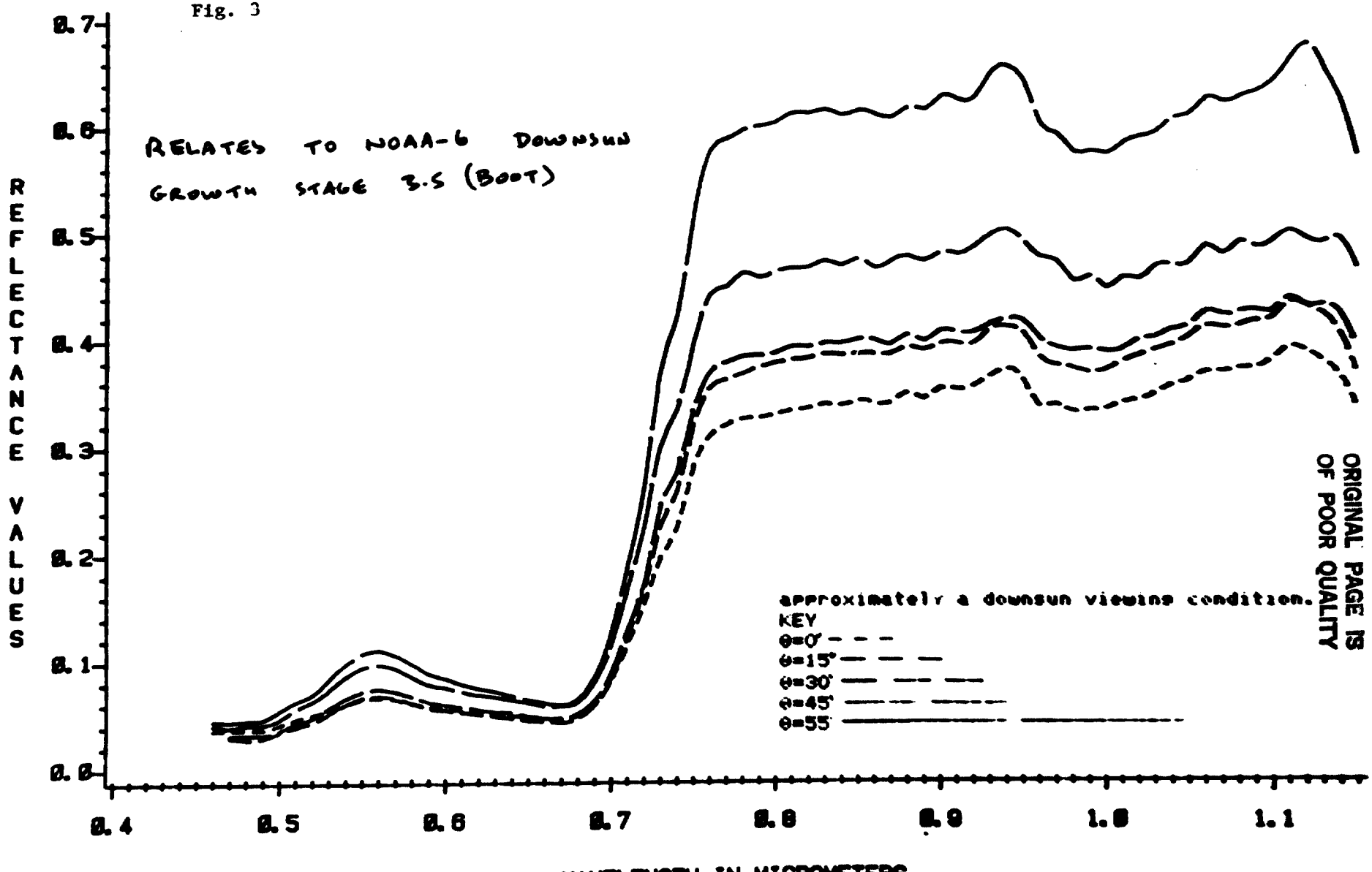

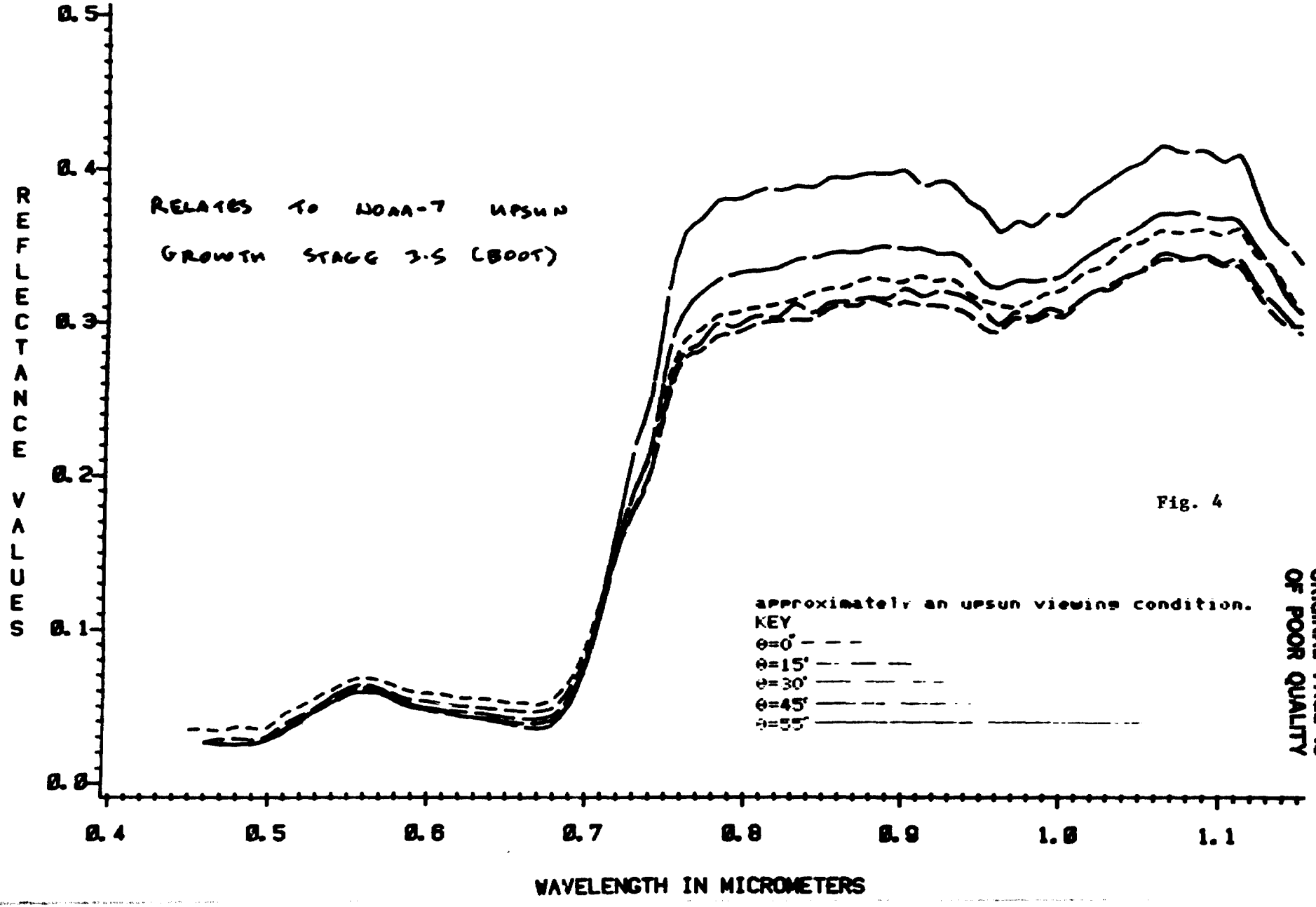

Fig. 4

Fig. 5

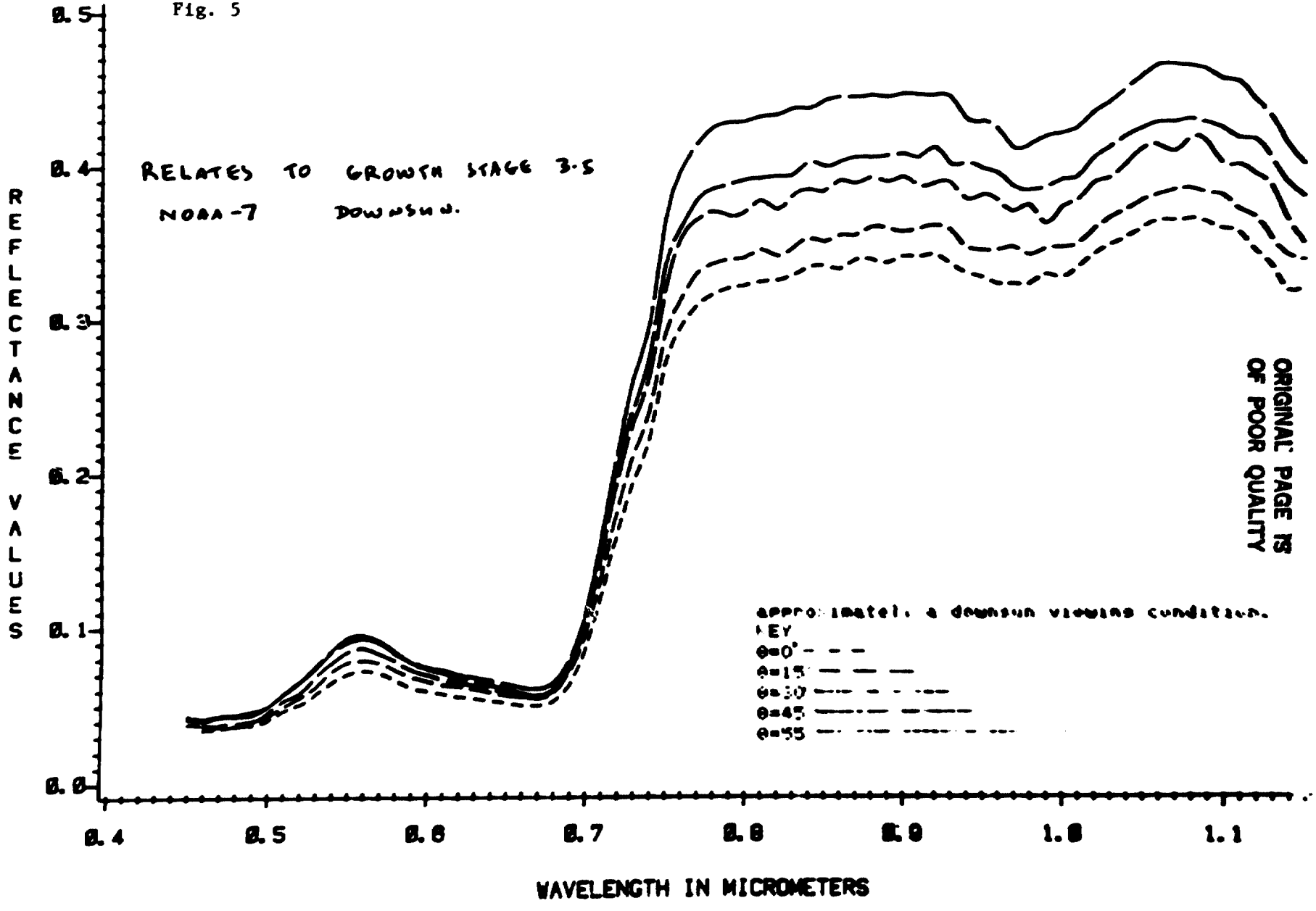

Fig. 6

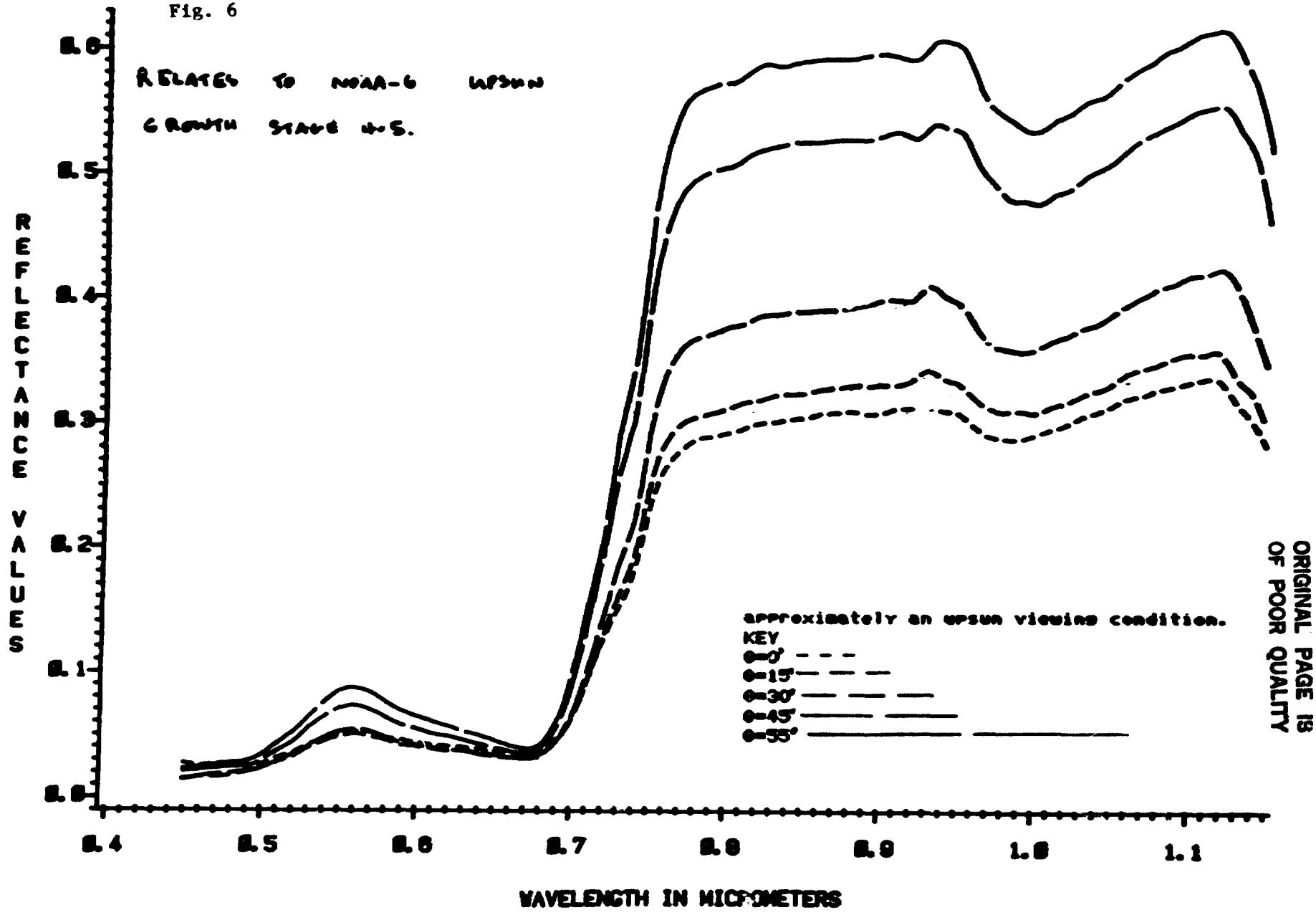

Fig. 7

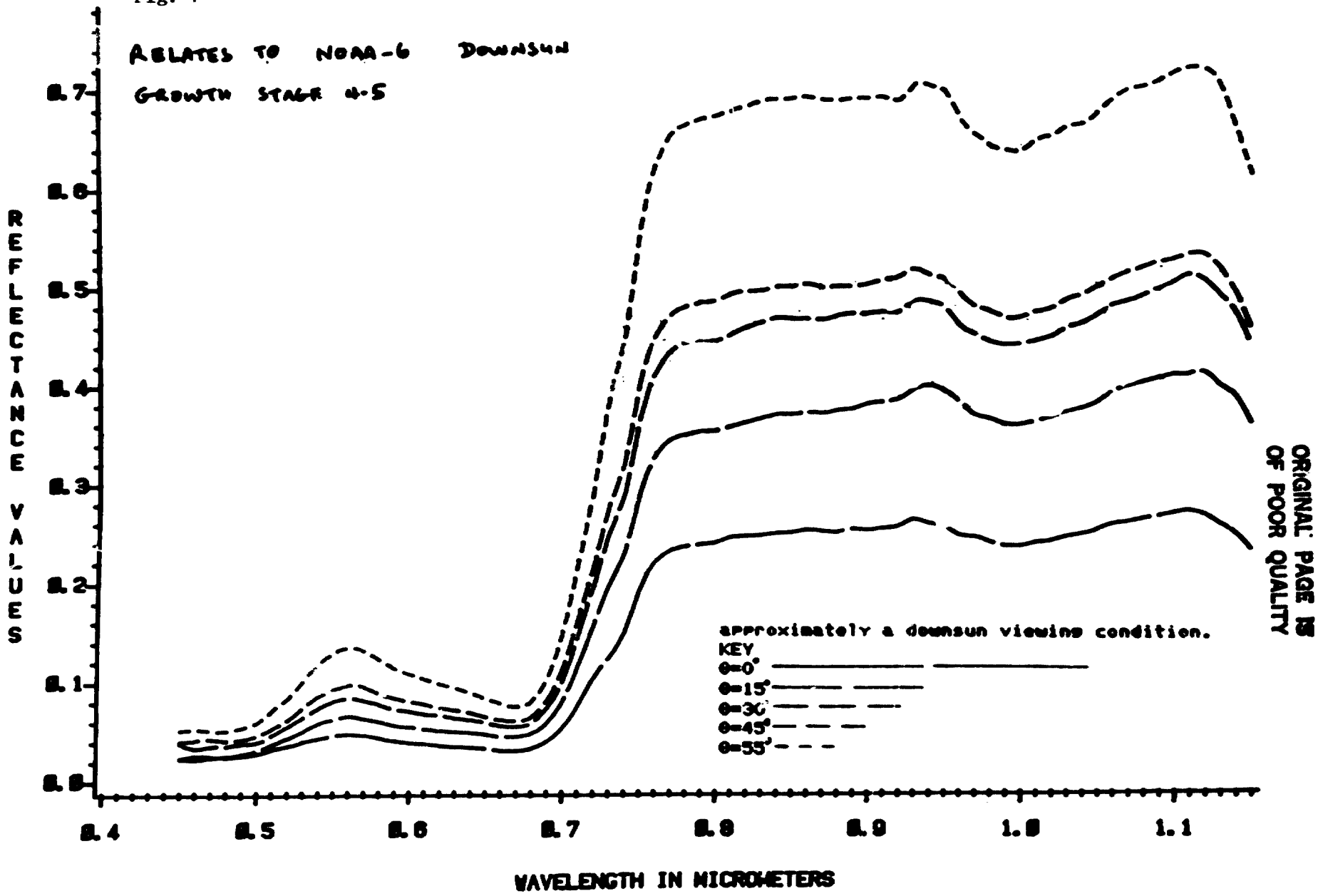

Fig. 8

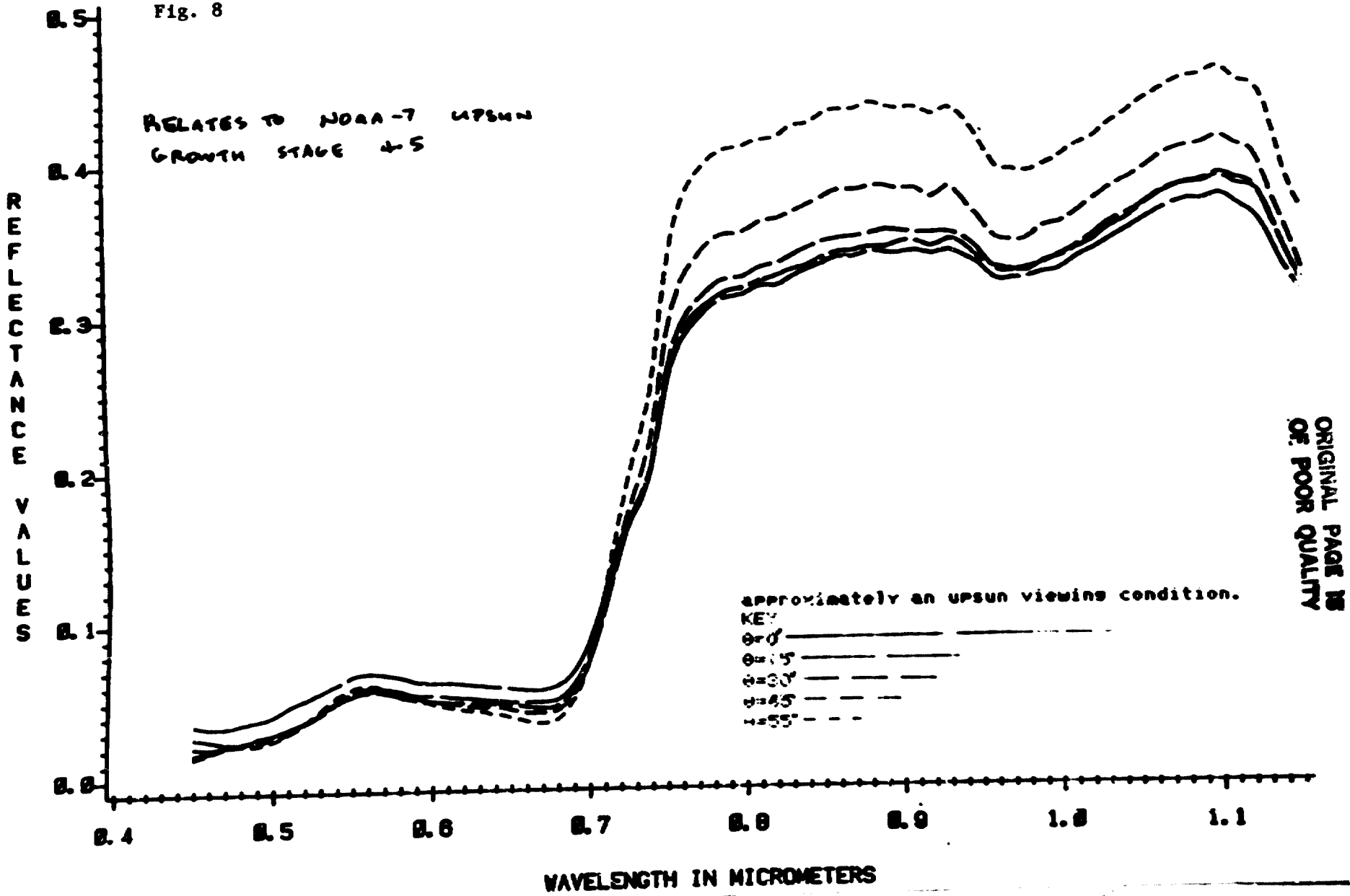

Fig. 9

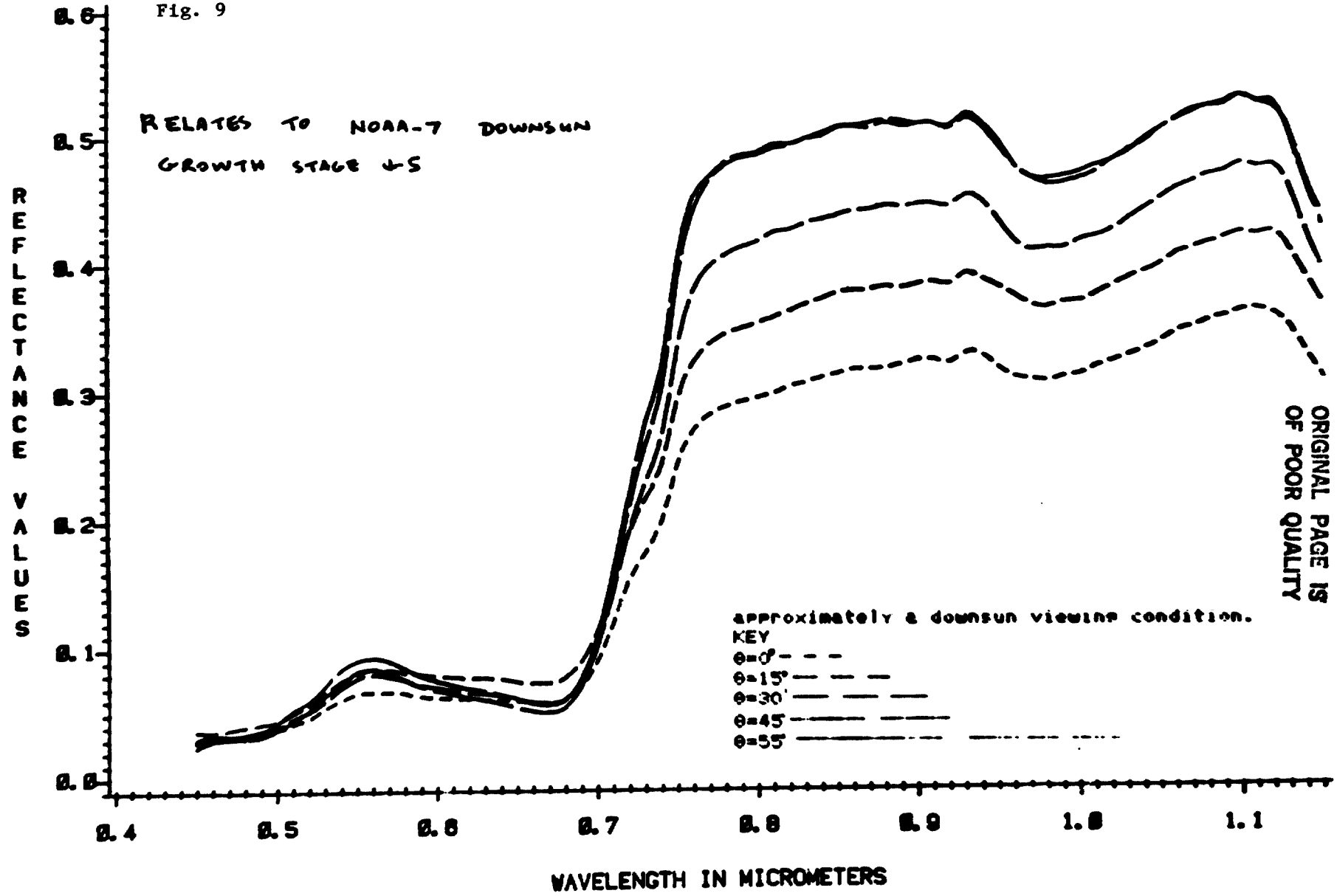
RELATES TO NOAA-7 DOWNSUN
GROWTH STAGE ↓5
REFLECTANCE VALUES
0.6
0.5
0.4
0.3
0.2
0.1
0.0
0.4
0.5
0.6
0.7
0.8
0.9
1.0
1.1
WAVELENGTH IN MICROMETERS
approximately a downsun viewing condition.
KEY
θ=0°
θ=15°
θ=30°
θ=45°
θ=55°
ORIGINAL PAGE IS
OF POOR QUALITY

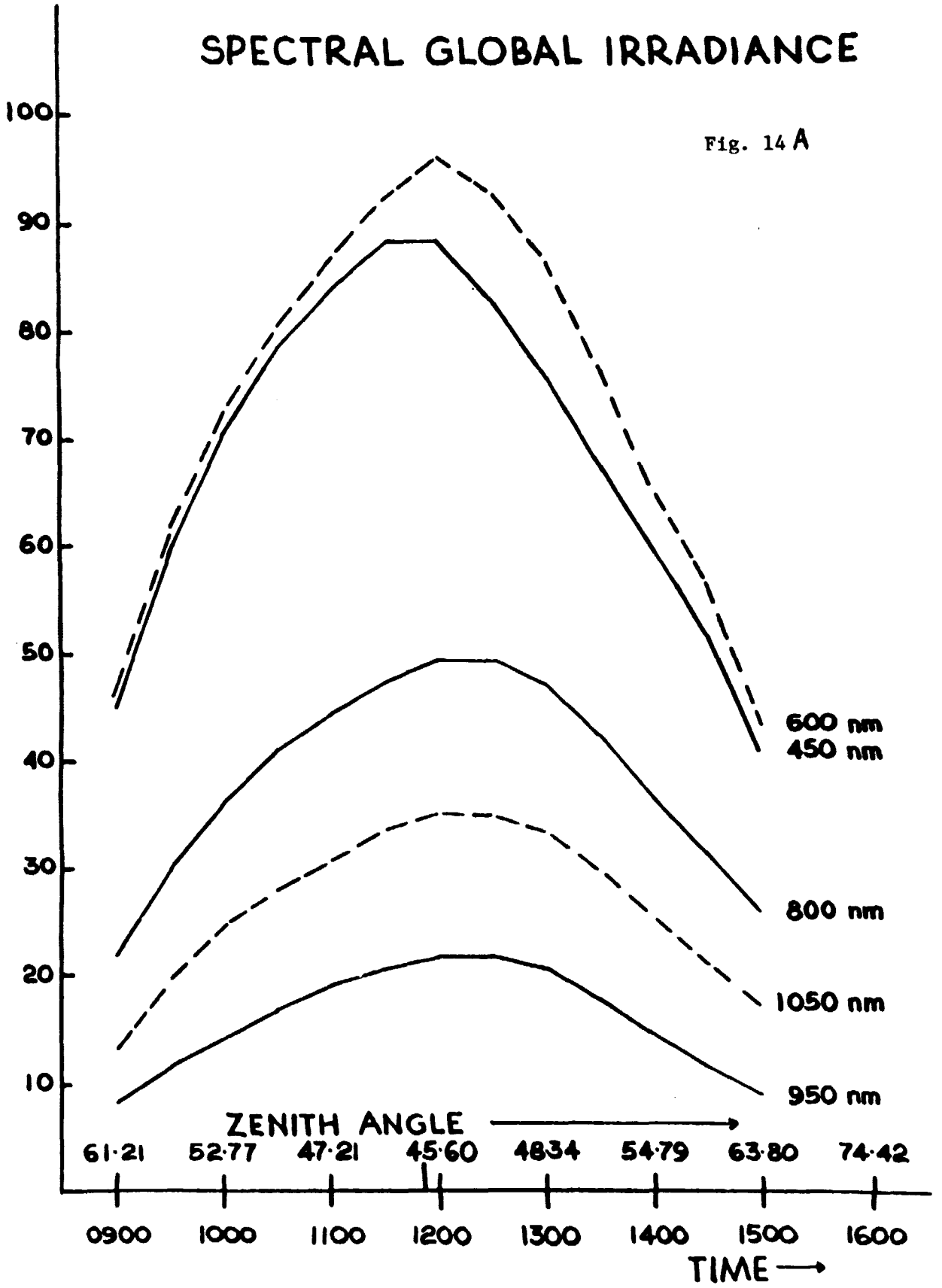

SOLAR ZENITH ANGLE DEPENDENCE OF SPECTRAL GLOBAL IRRADIANCE

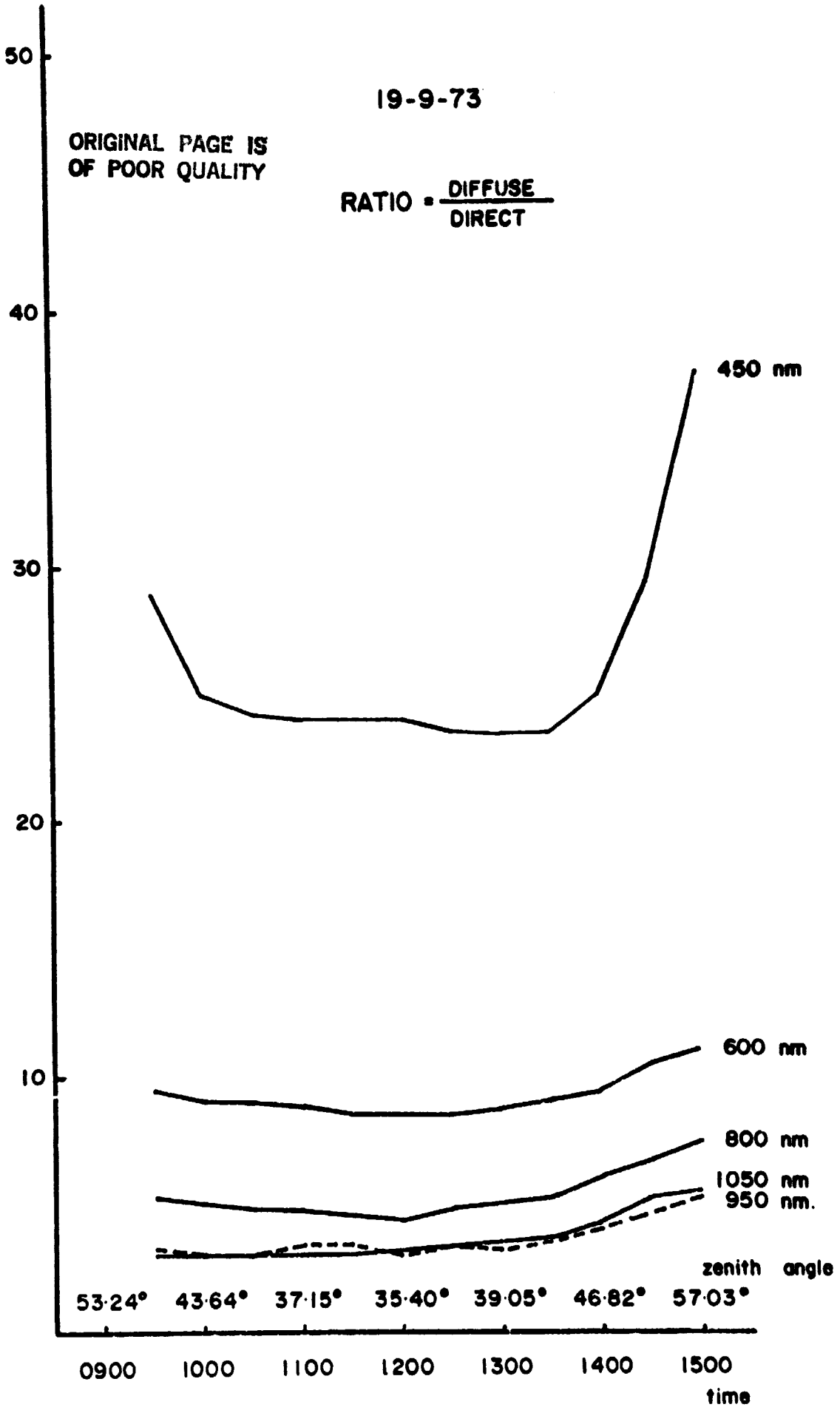
19-9-73
ORIGINAL PAGE IS
OF POOR QUALITY
RATIO = DIFFUSE / DIRECT
50
40
30
20
10
450 nm
600 nm
800 nm
1050 nm
950 nm.
zenith angle
53·24°
43·64°
37·15°
35·40°
39·05°
46·82°
57·03°
0900
1000
1100
1200
1300
1400
1500
time

Fig. 14-B

Fig. 15

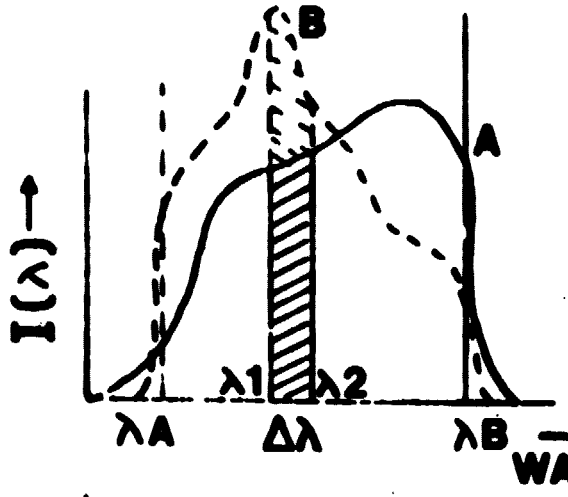

Spectral sensitivity of detector I(λ)

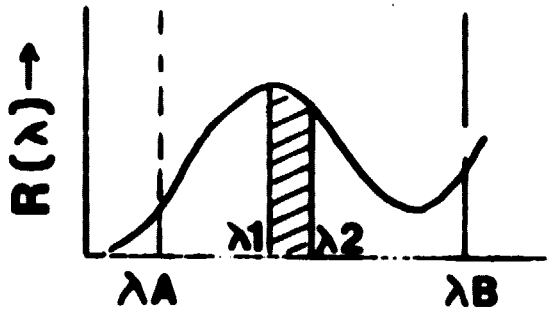

Spectral reflectance factor of target R(λ)

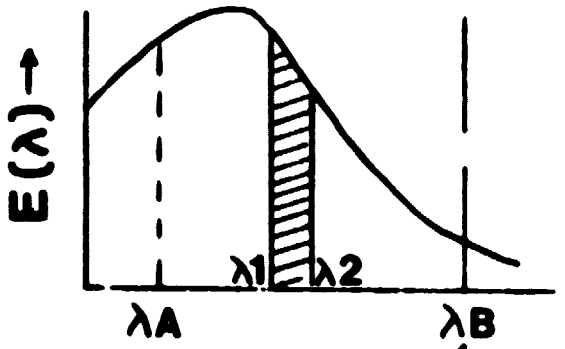

Spectral solar irradiance on target E(λ)

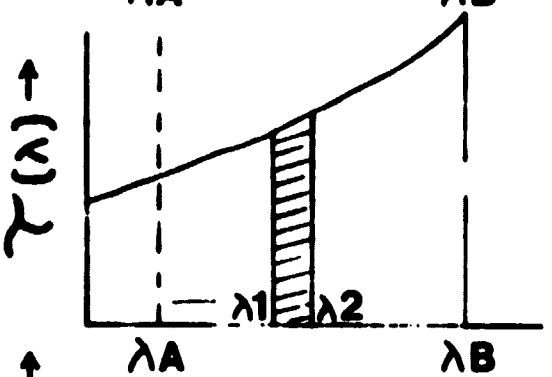

Spectral atmospheric transmission τ(λ)

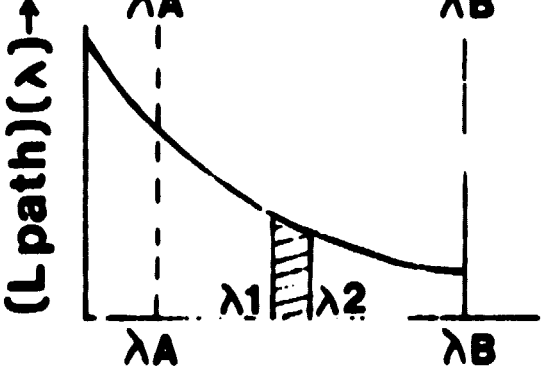

Spectral atmospheric path radiance (Lpath)(λ)

Fig. 16

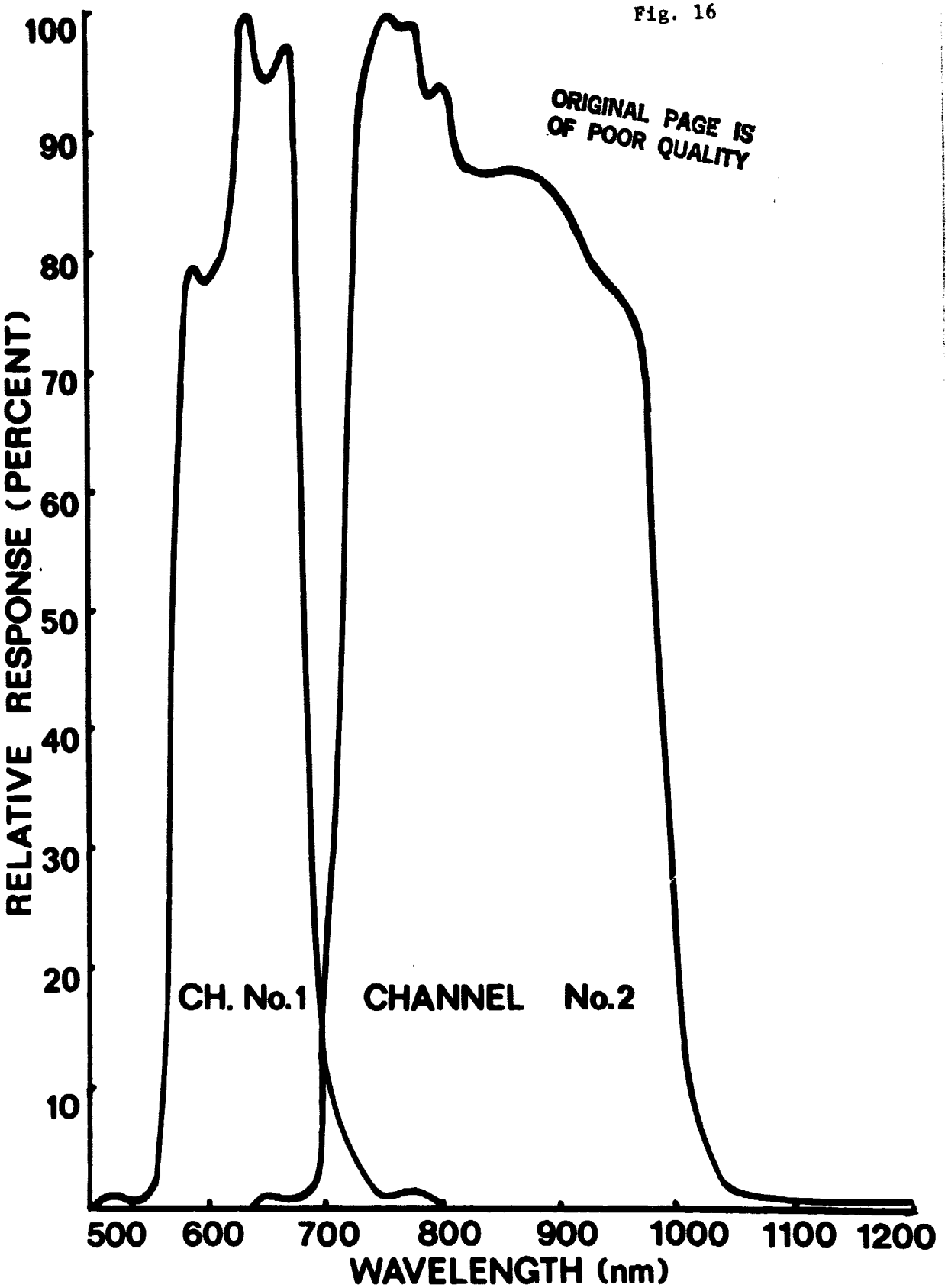
ORIGINAL PAGE IS
OF POOR QUALITY
RELATIVE RESPONSE (PERCENT)
100
90
80
70
60
50
40
30
20
10
CH. No.1
CHANNEL No.2
500
600
700
800
900
1000
1100
1200
WAVELENGTH (nm)

CLEAR ATMOSPHERE ——
TURBID ATMOSPHERE - - -

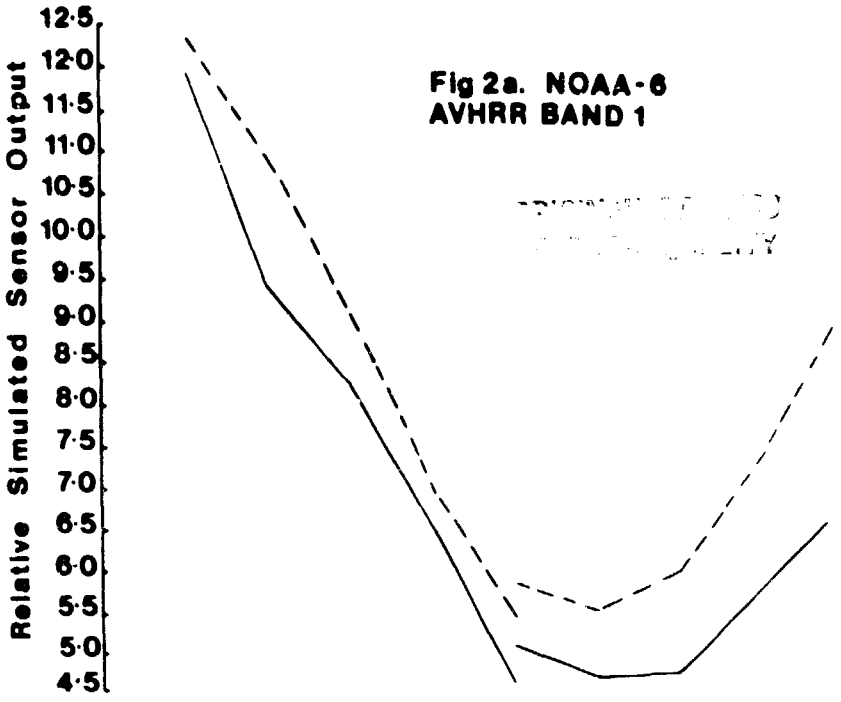

Fig 2a. NOAA-6
AVHRR BAND 1

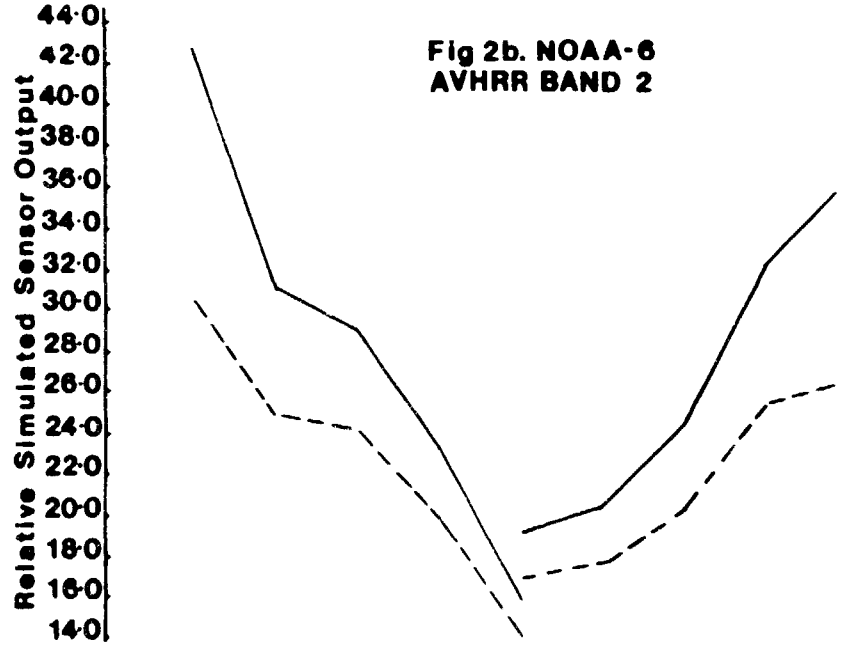

Fig 2b. NOAA-6
AVHRR BAND 2

Fig. 2c.

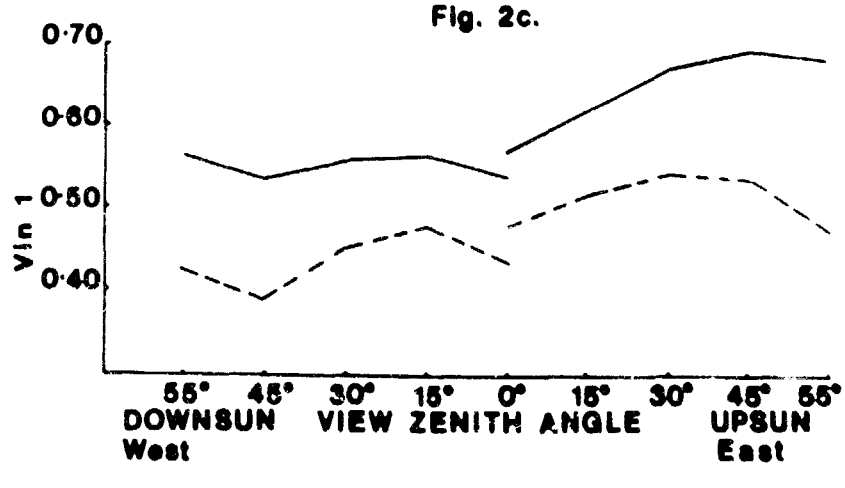

Fig. 18

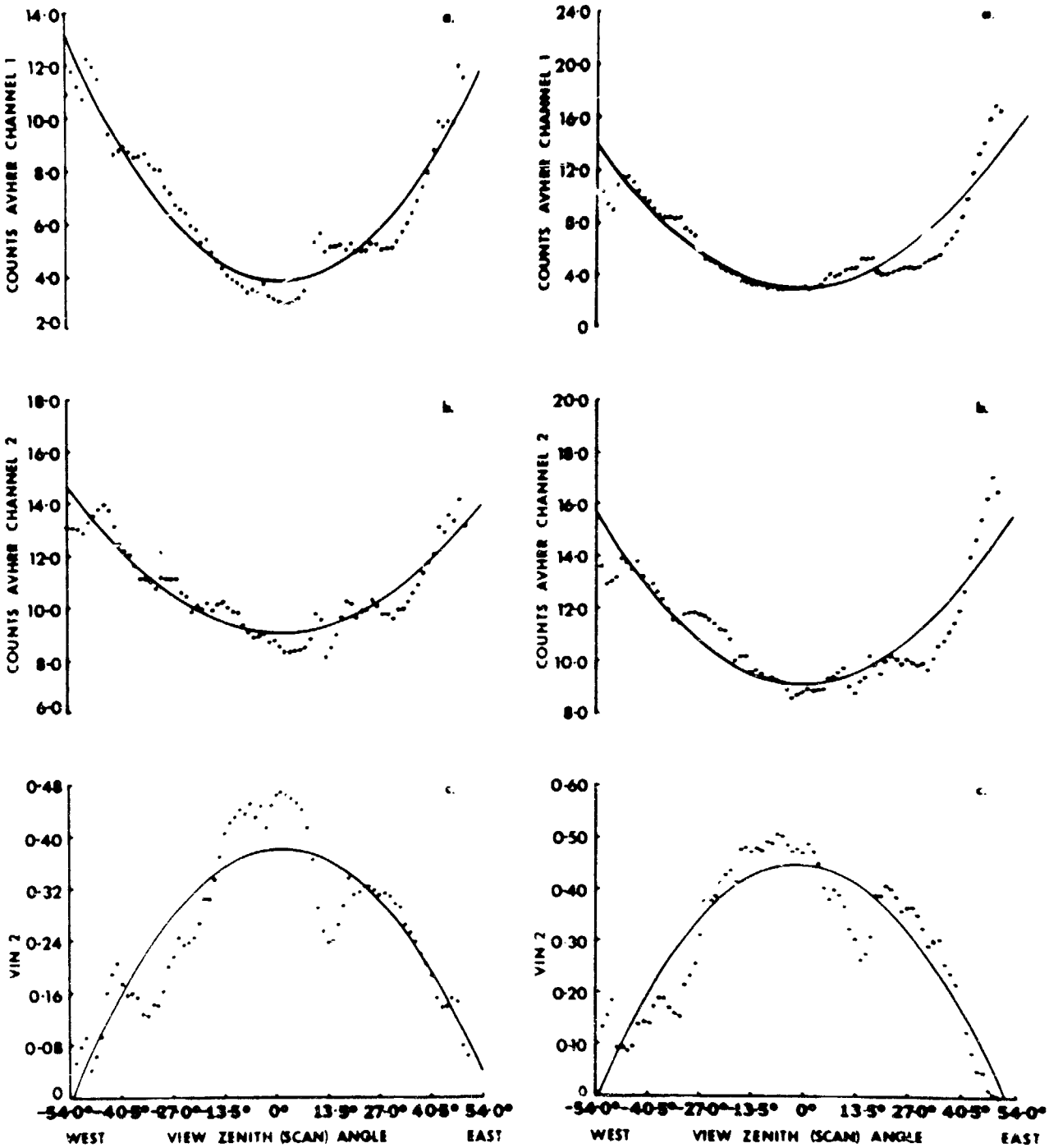

Two different image swaths were analyzed to illustrate that sensor output and vegetation index (normalized difference of sensor outputs) vary with view zenith (scan) angle.

Fig. 19

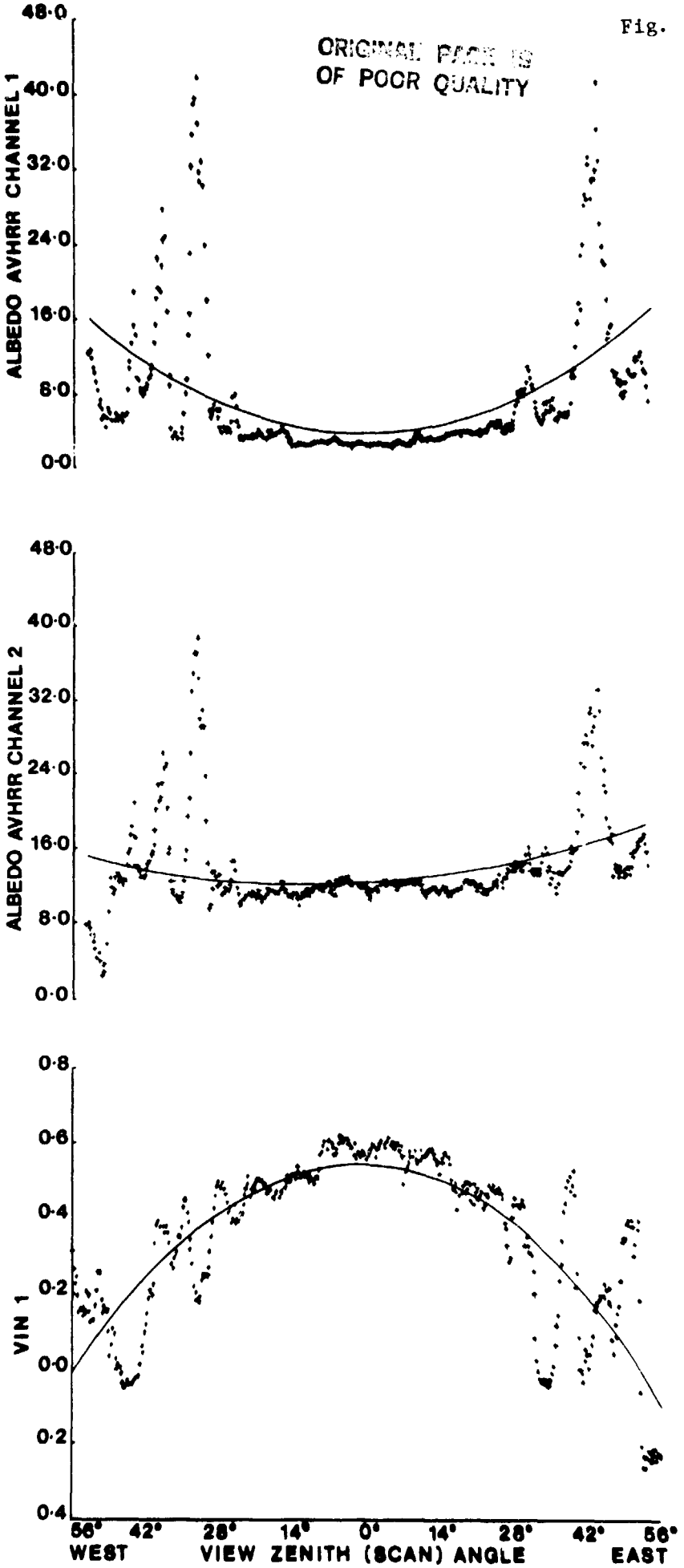

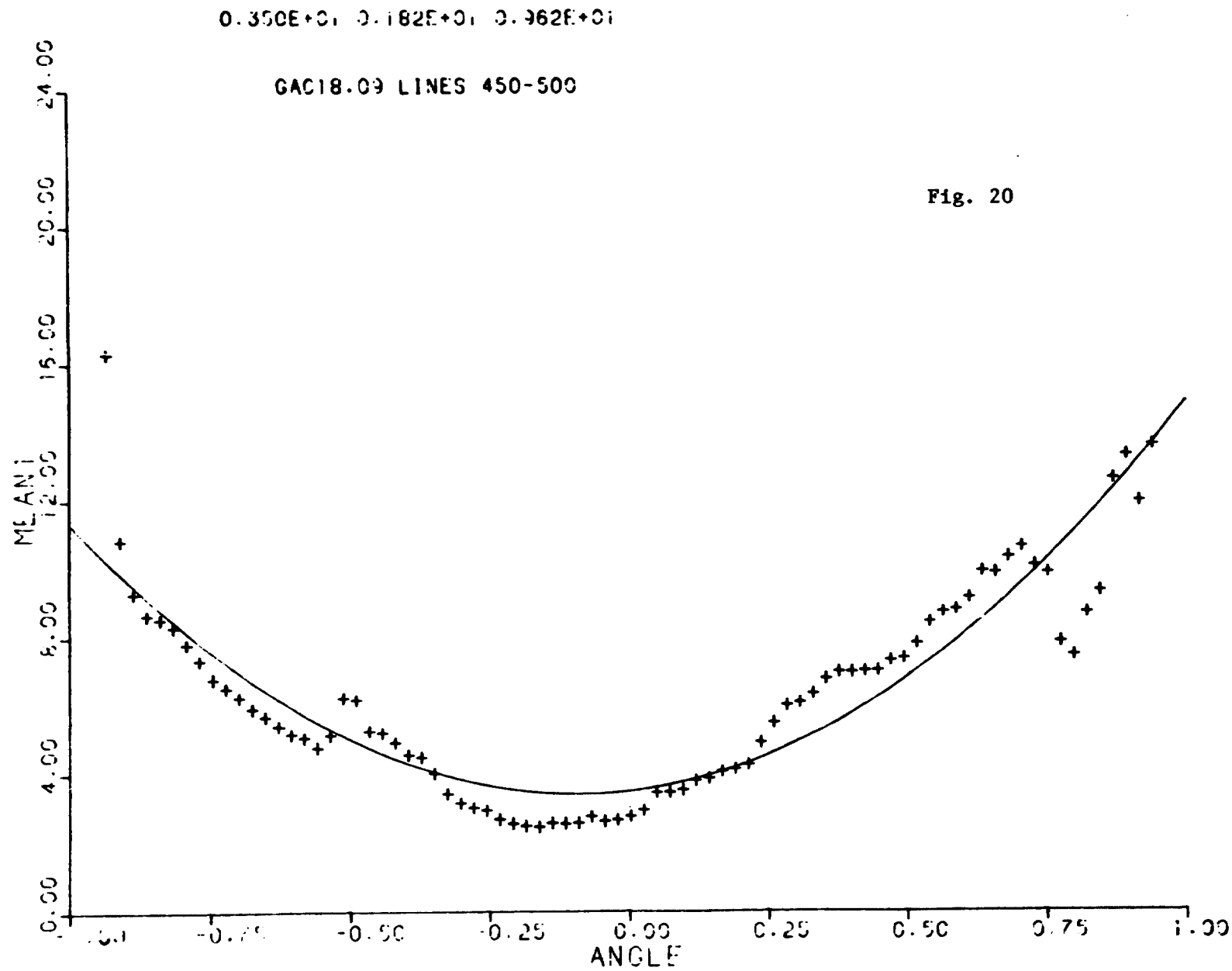

Fig. 20

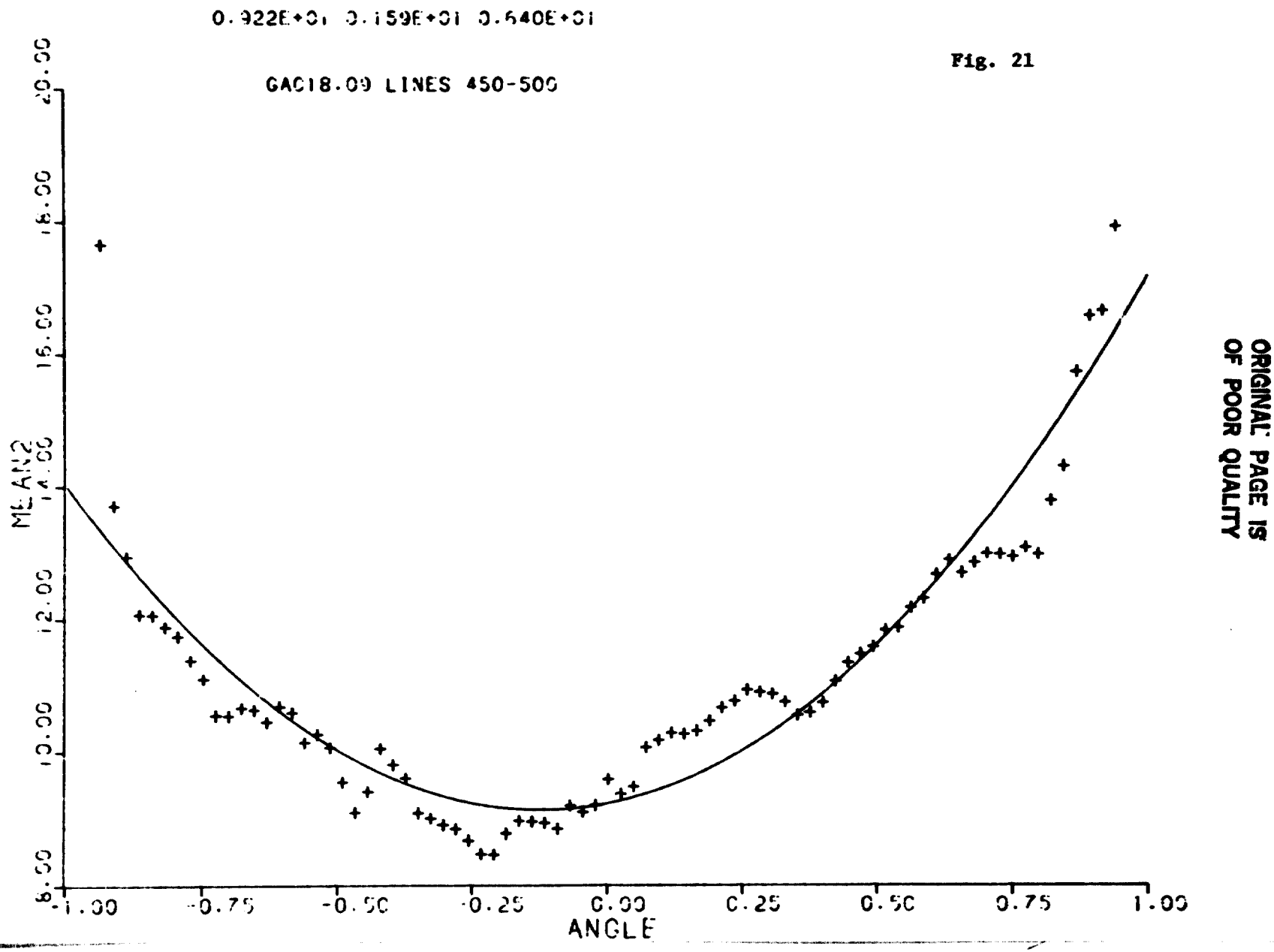

Fig. 21

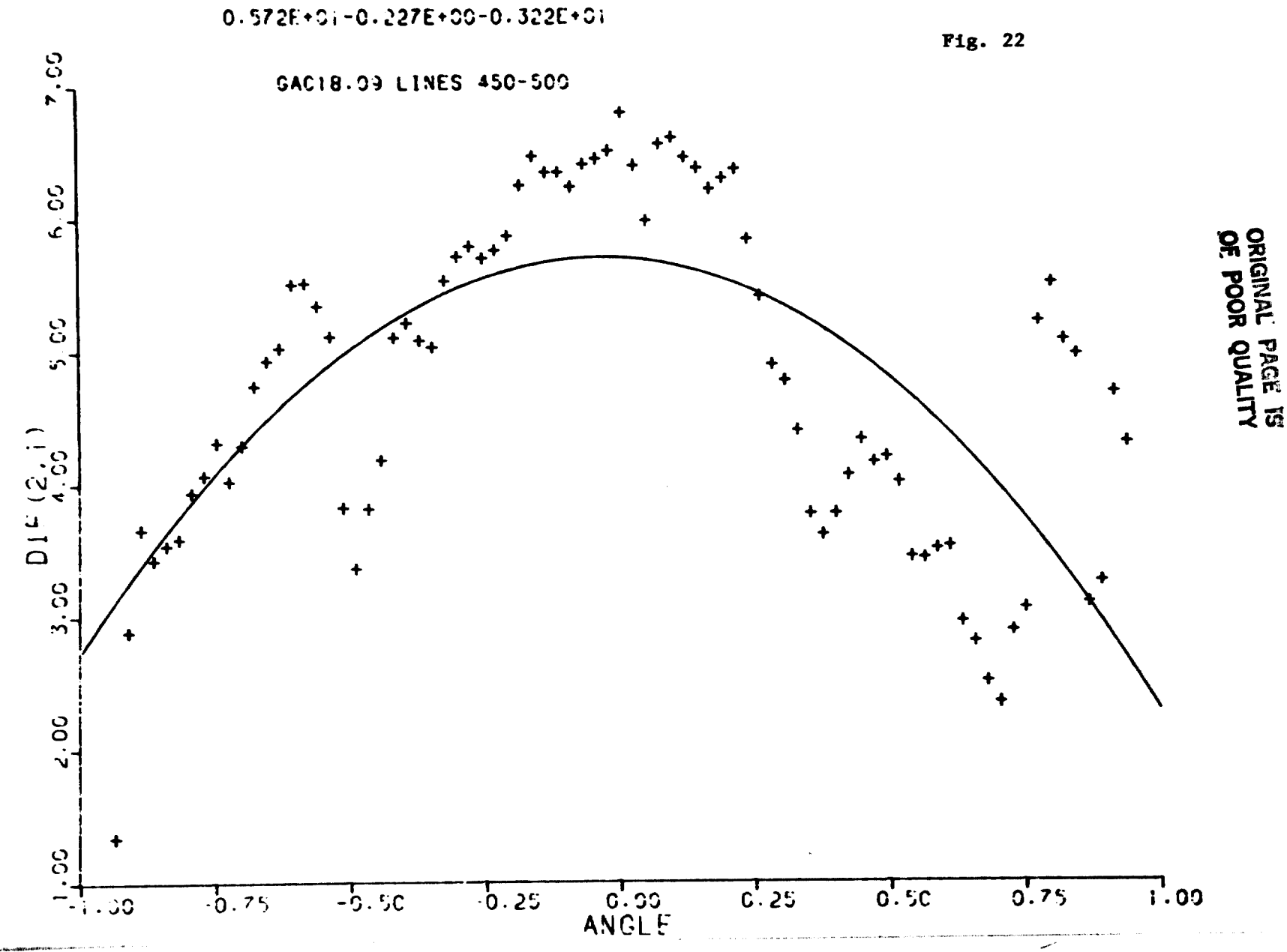

Fig. 22

0.437E+00-0.618E-01-0.431E+00

CAC18.09 LINES 450-500

Fig. 23

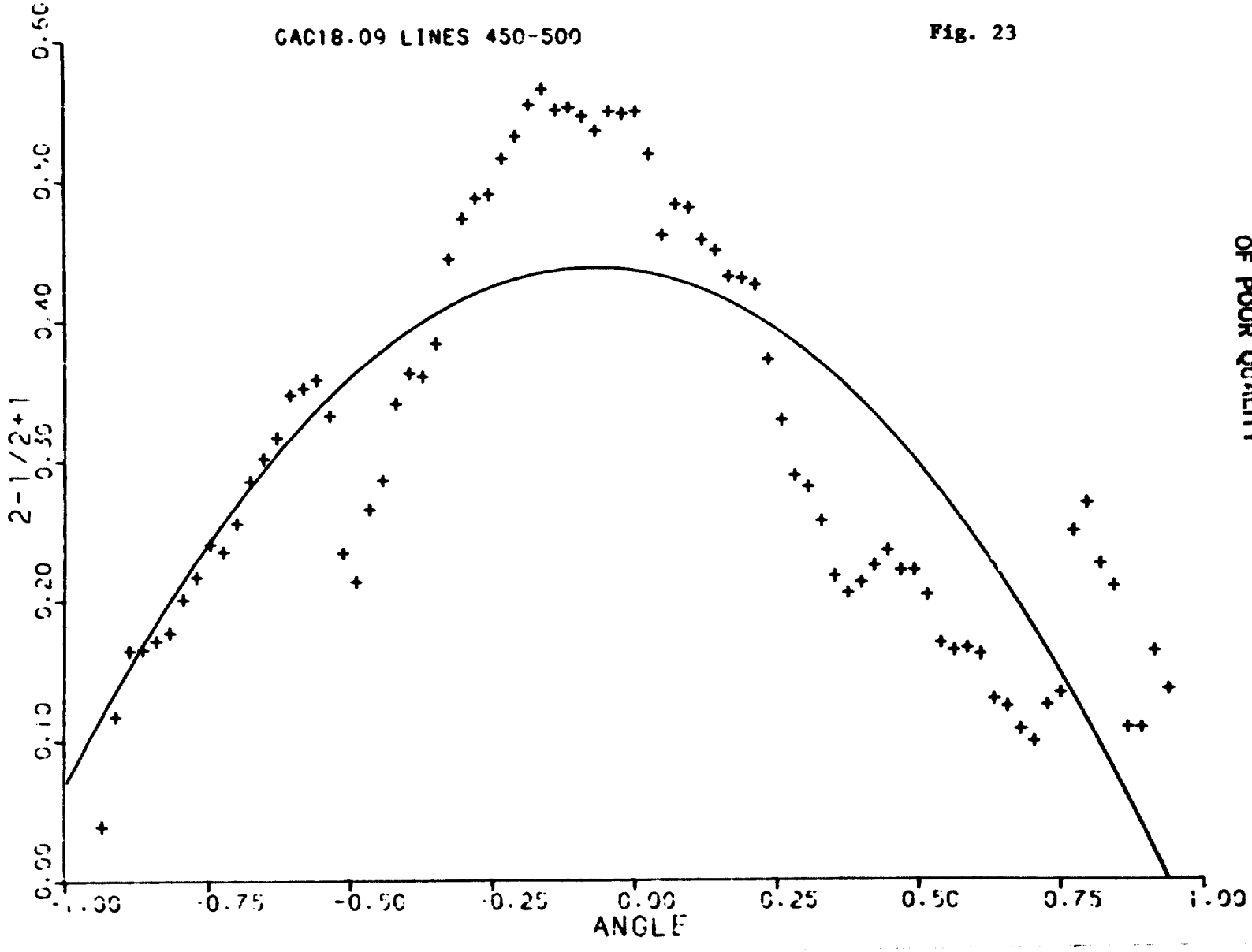

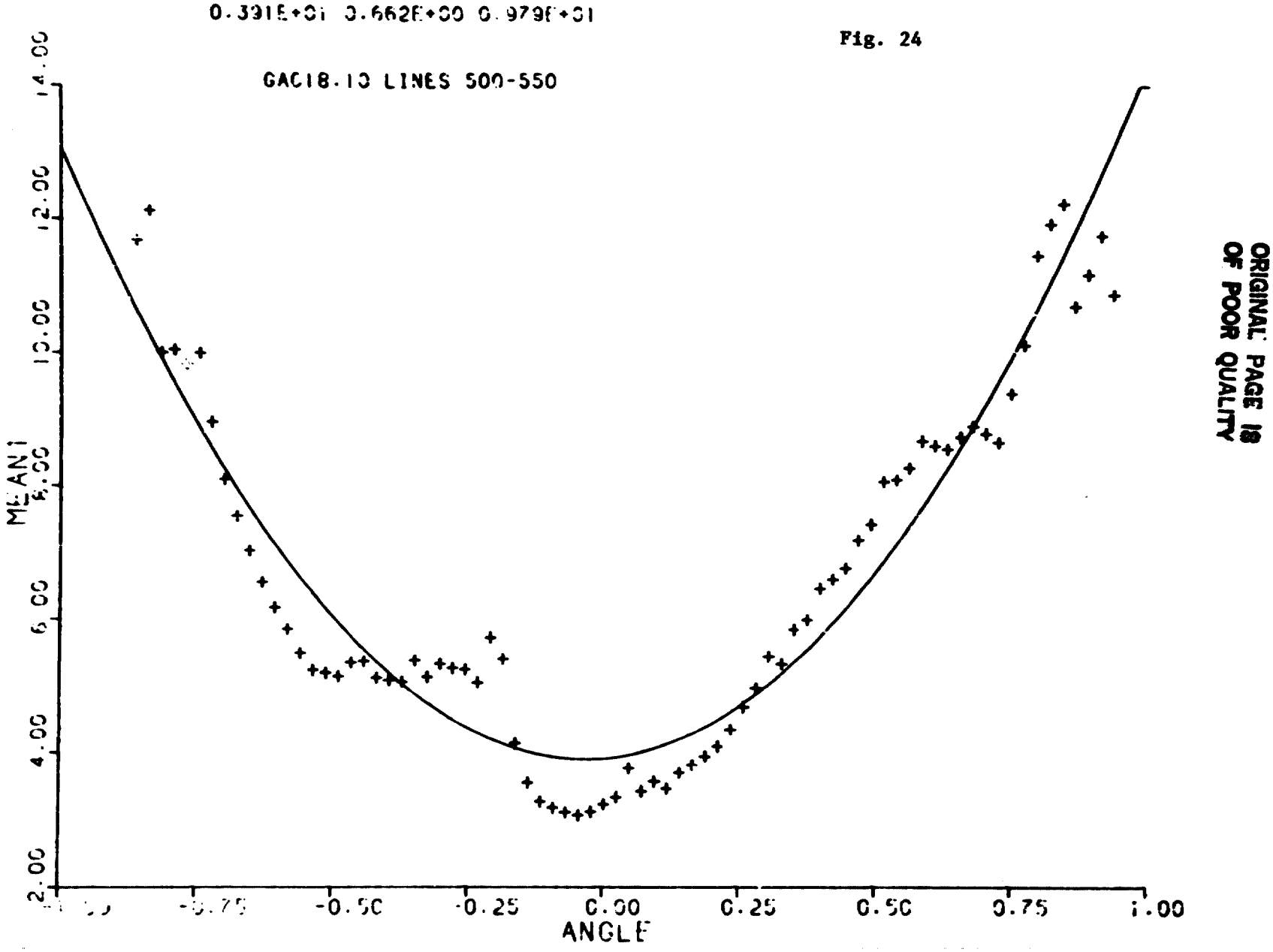

Fig. 24

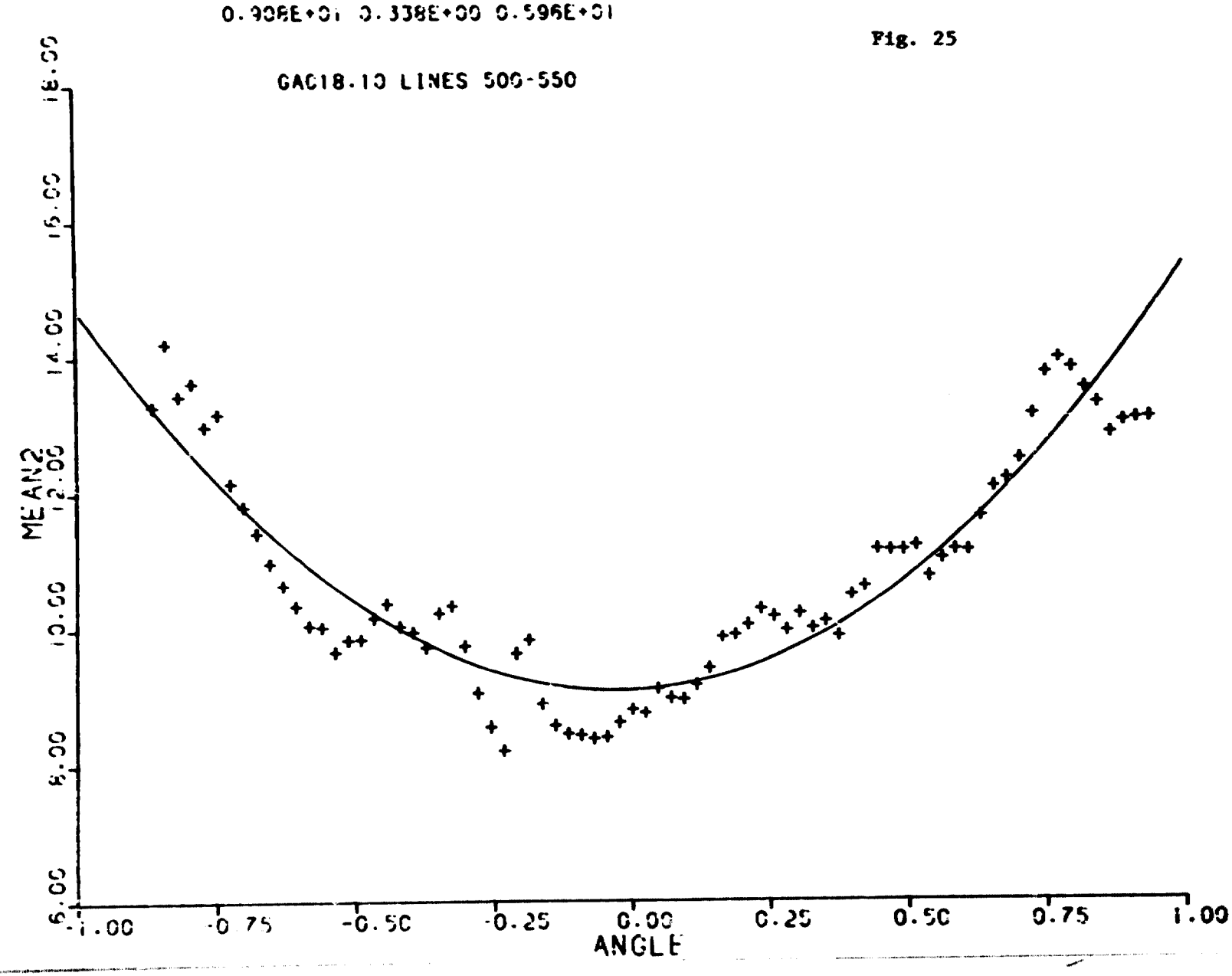

Fig. 25

0.517E+01-0.325E+00-0.383E+01

Fig. 26

GAC18.10 LINES 500-550

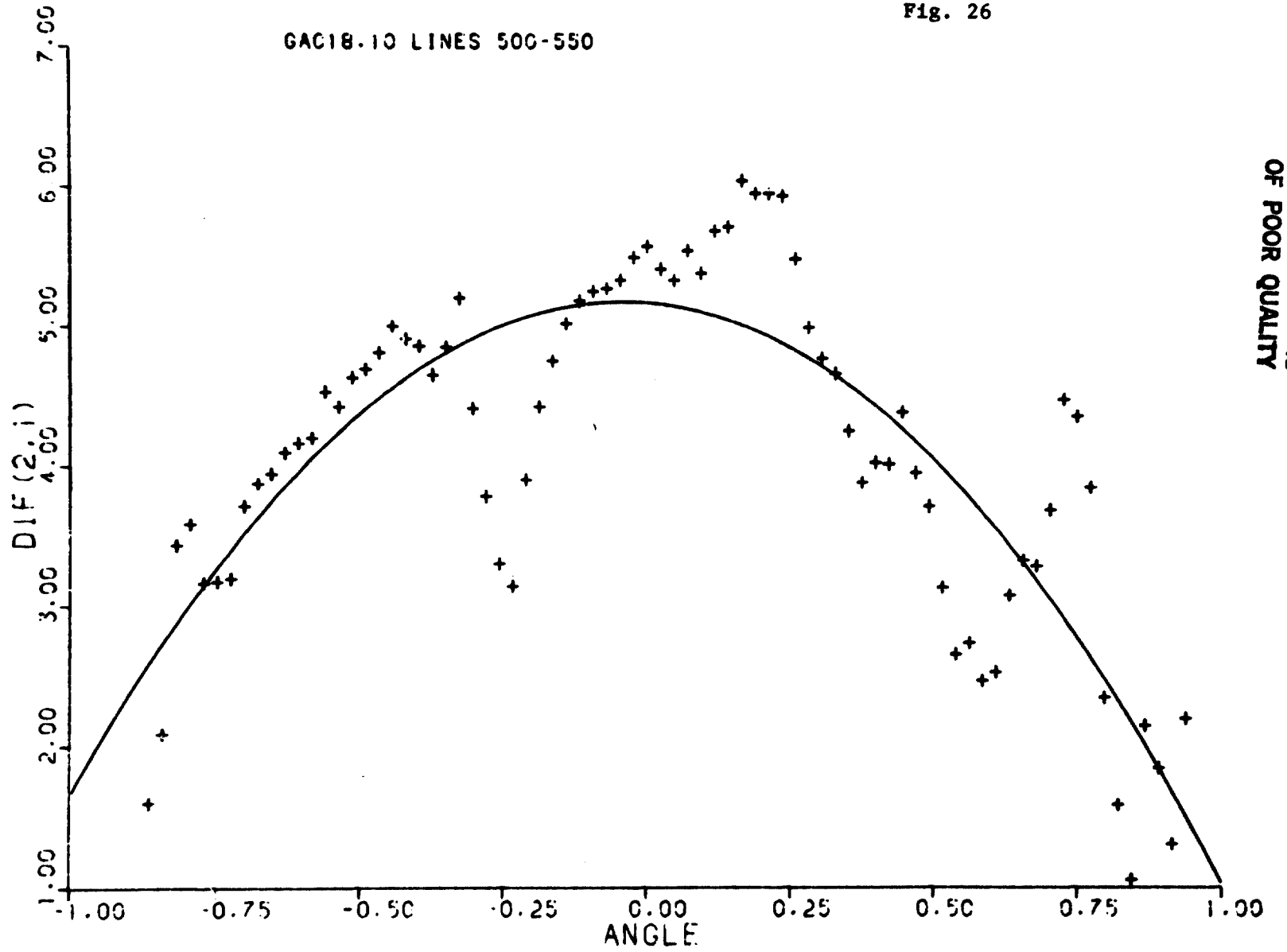

0.380E+00-0.248E-01-0.419E+00

Fig. 27

CAC18.10 LINES 500-550

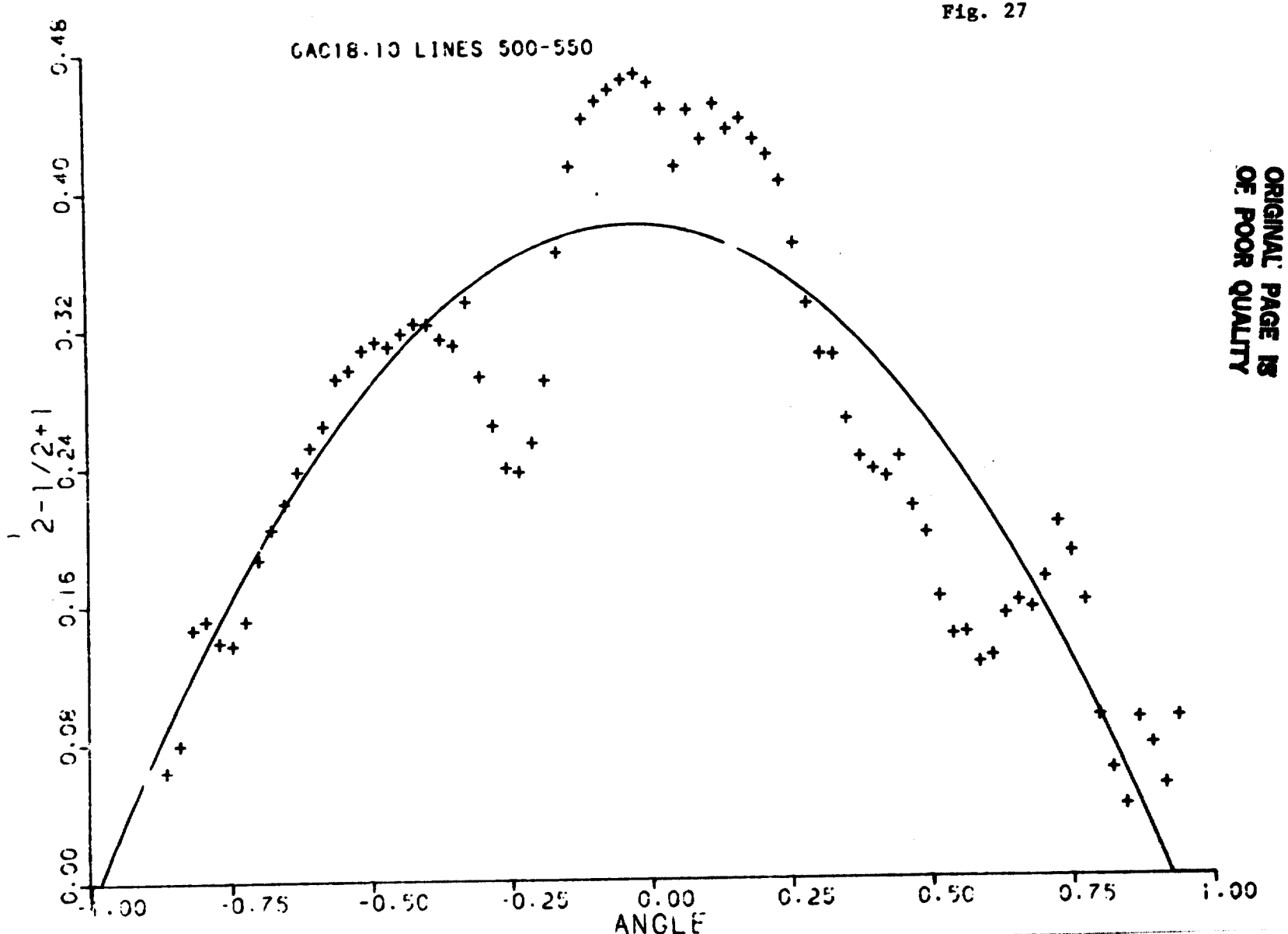

0.213E+01 0.699E-01 0.486E+01

Fig. 28

GAC18.02 LINES 450-500

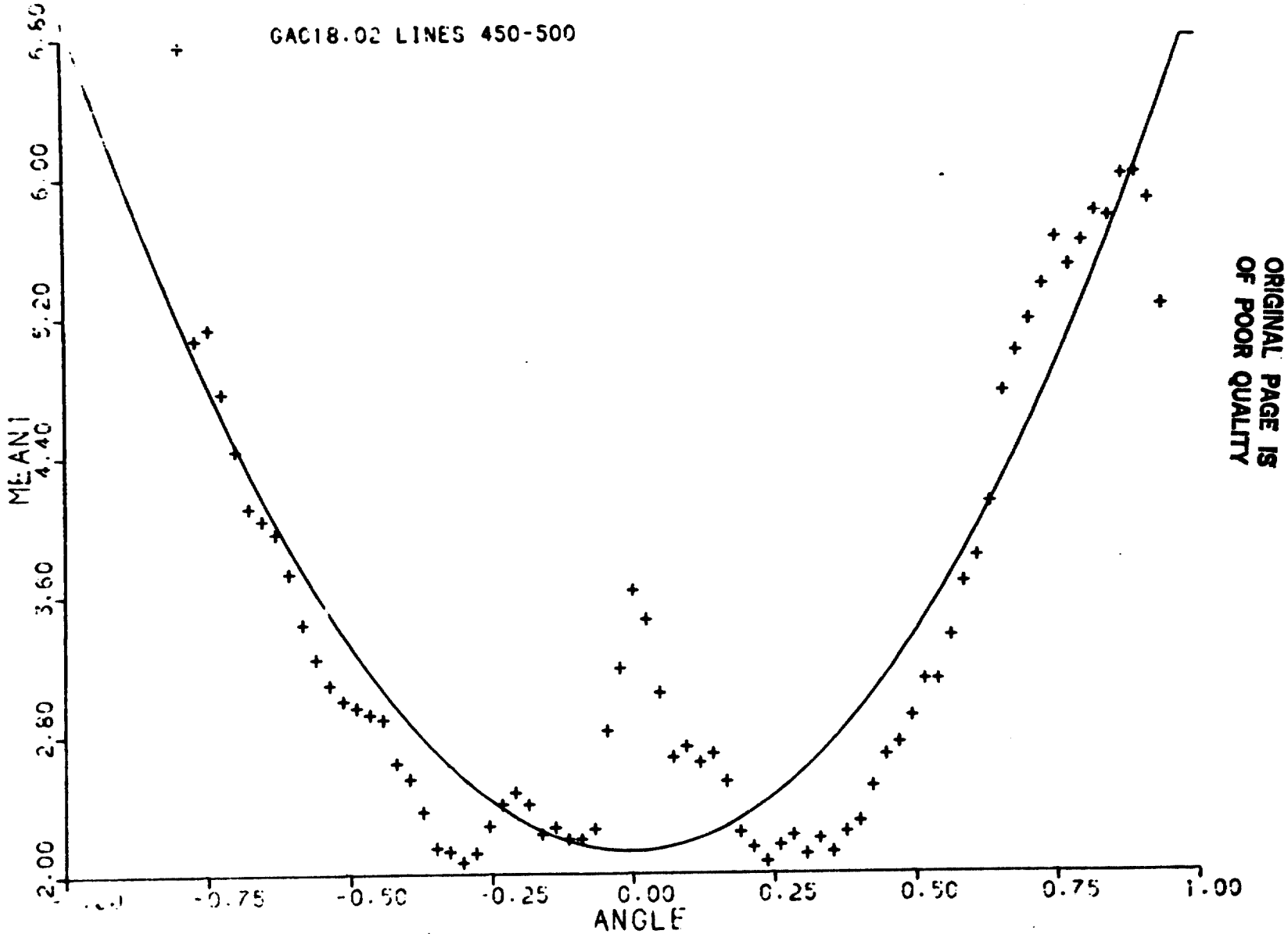

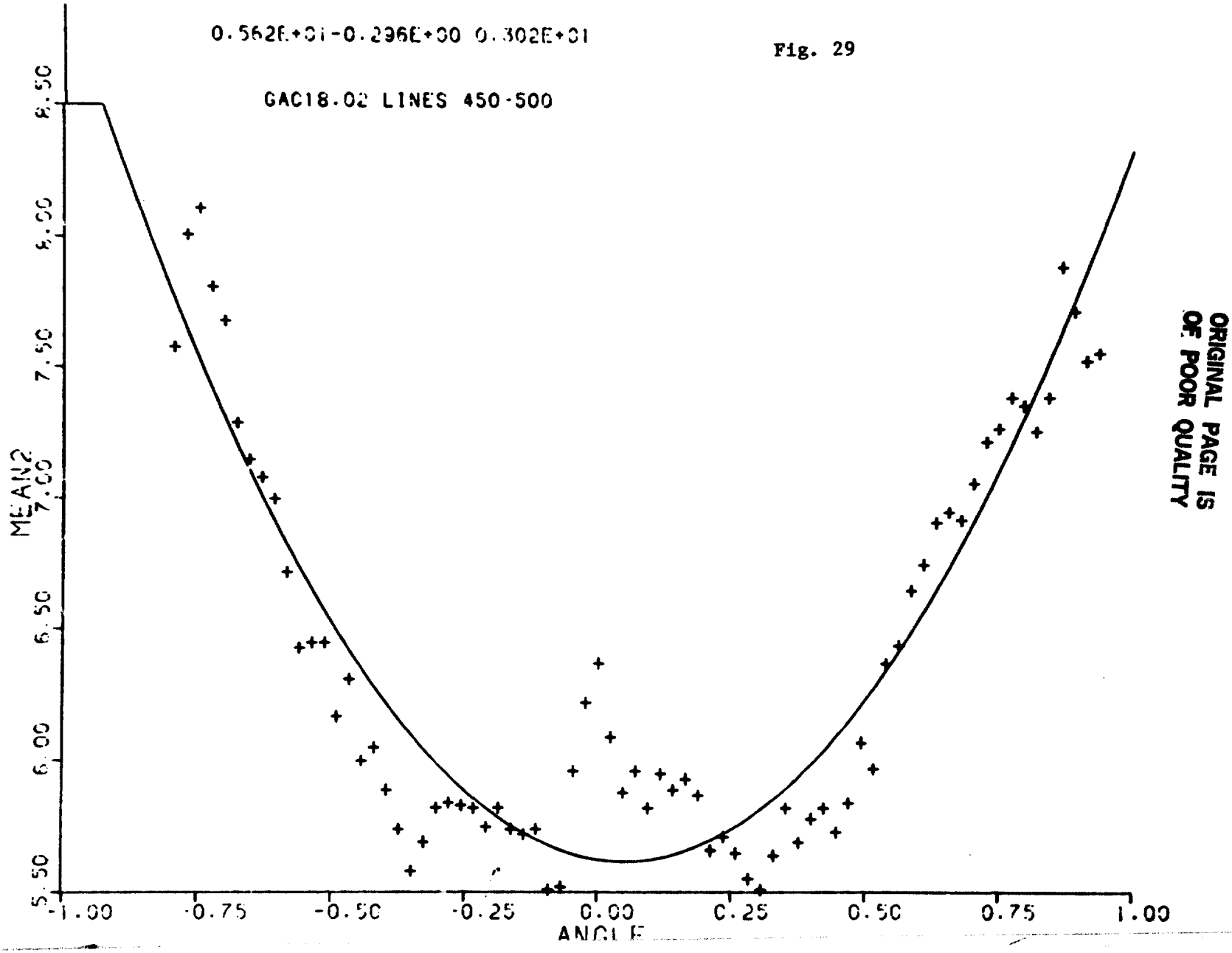

Fig. 29

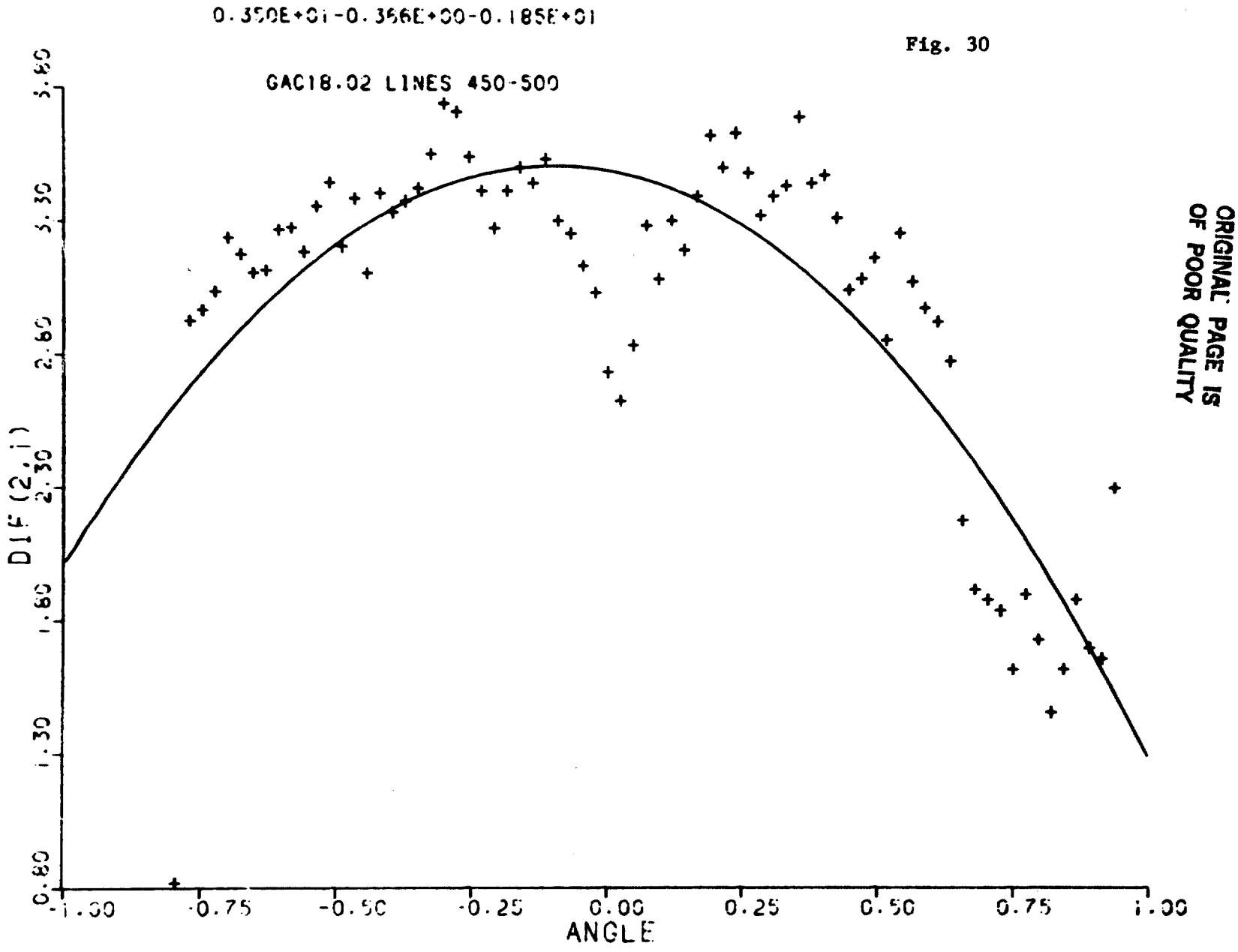

Fig. 30

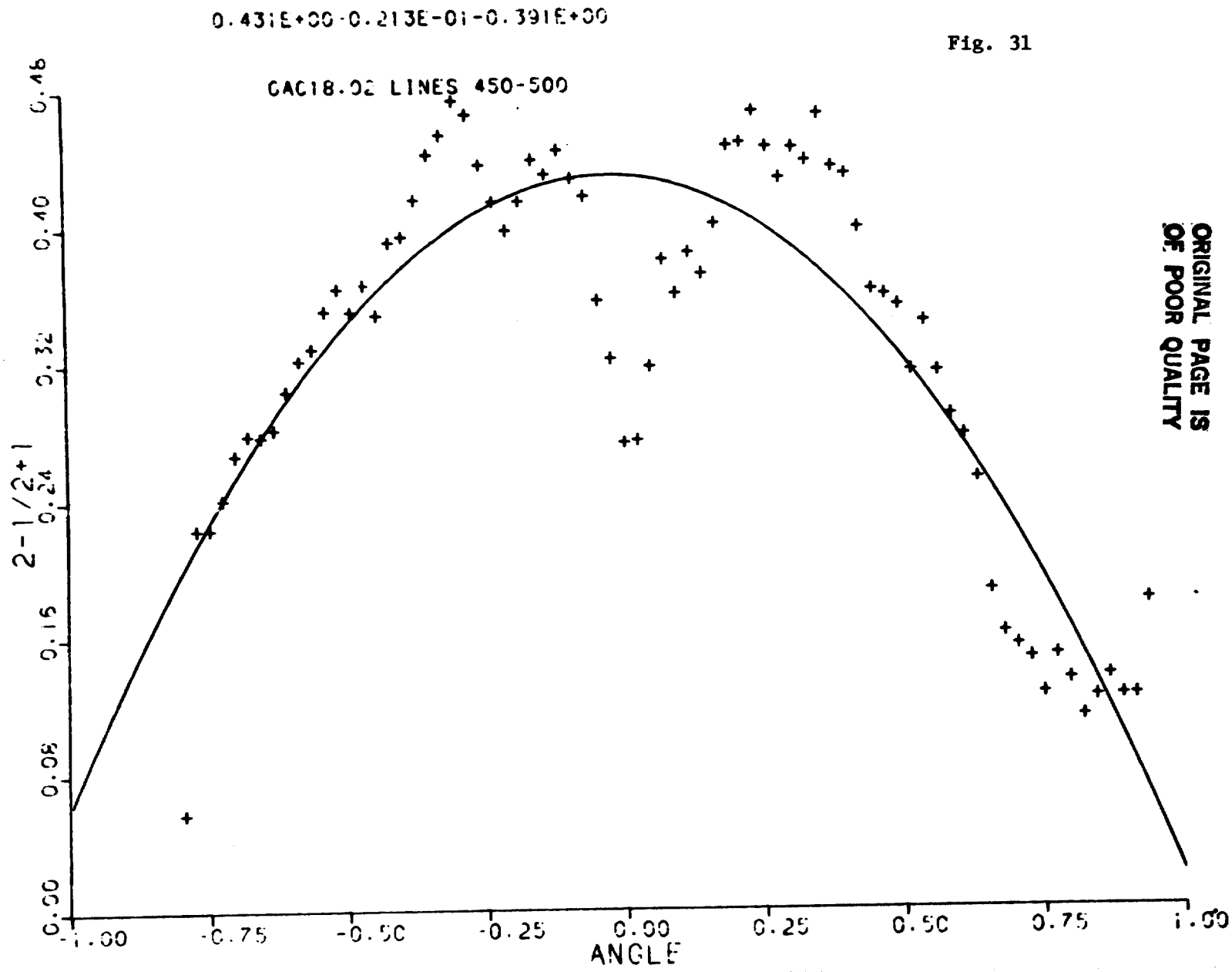

Fig. 31

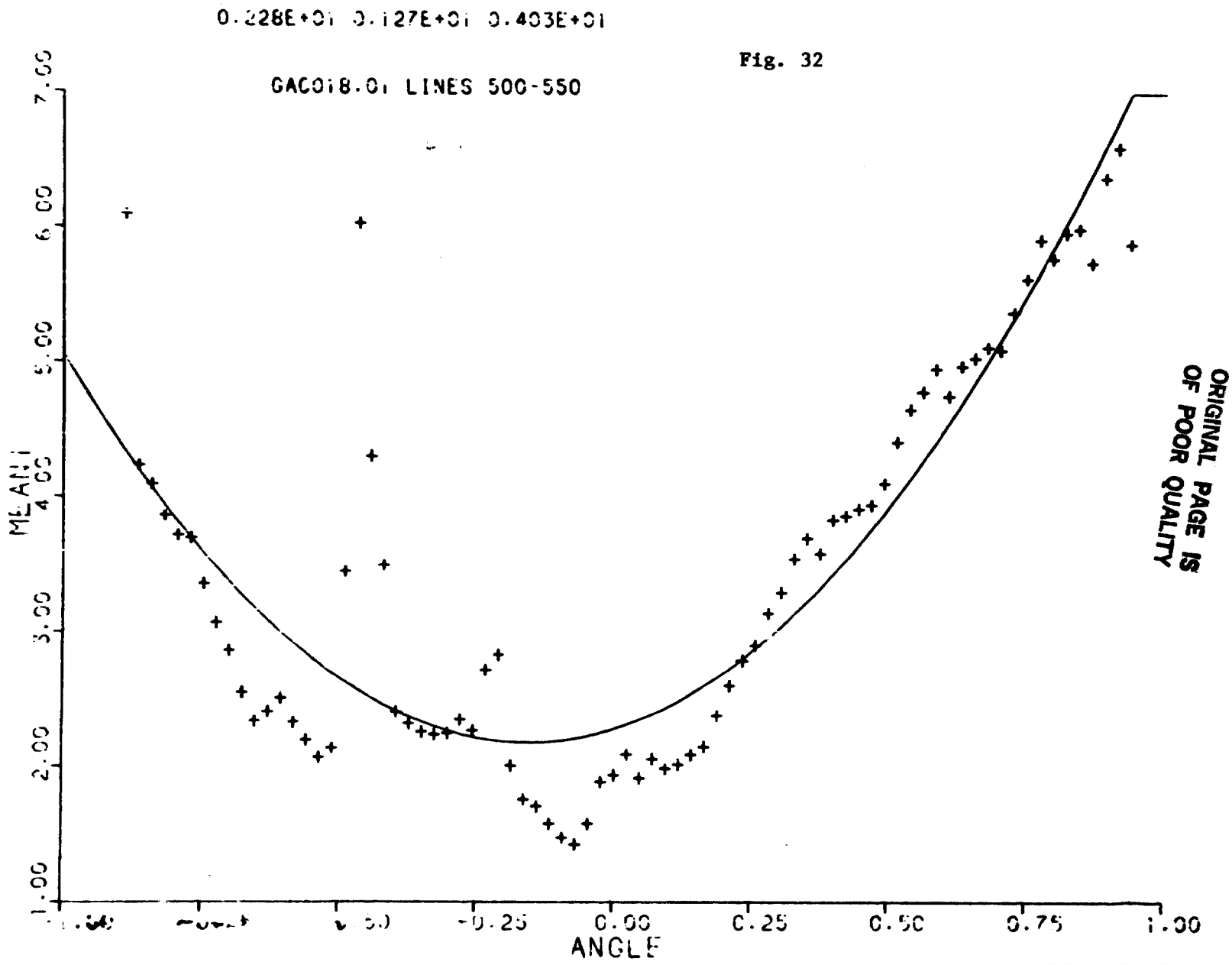

Fig. 32

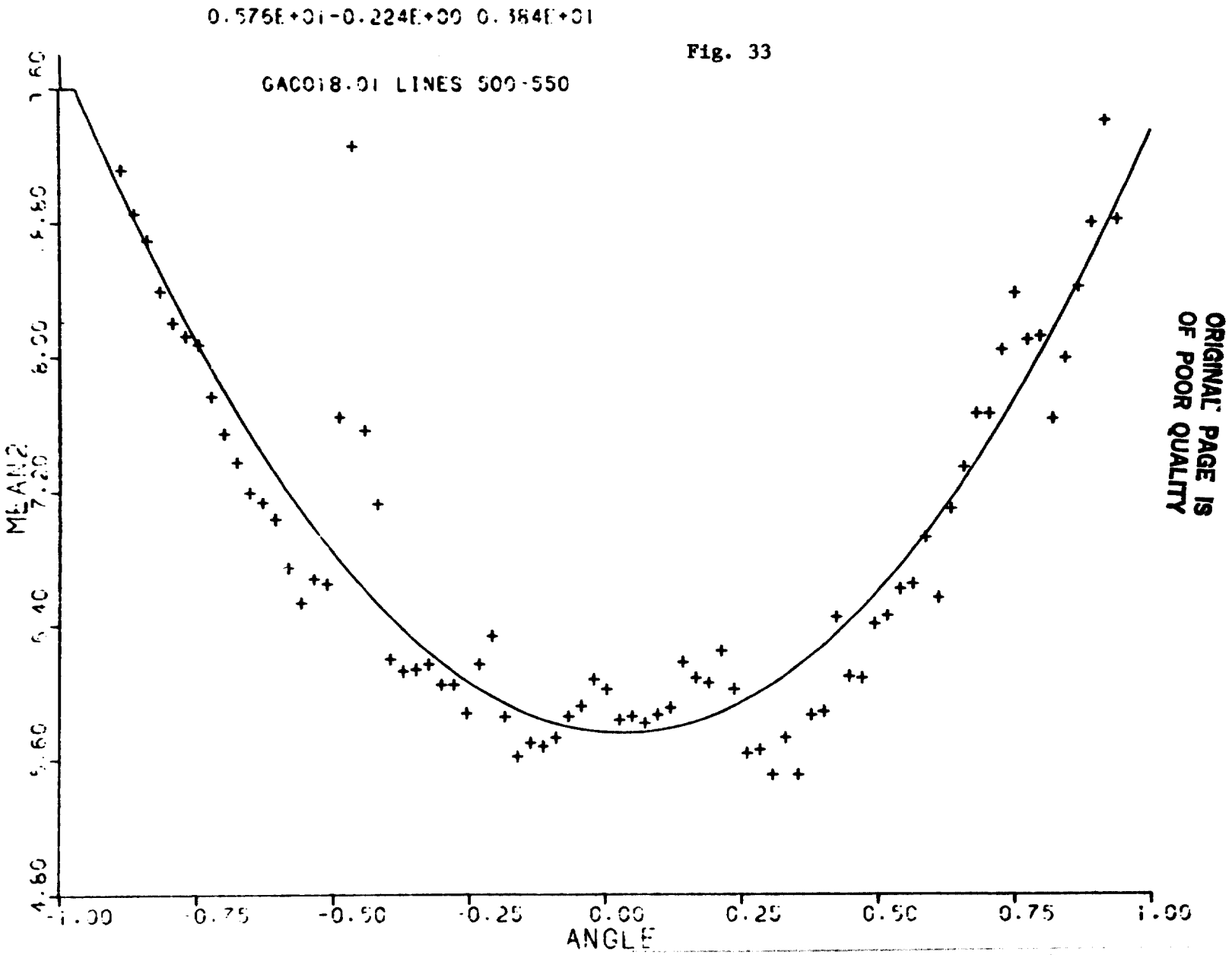

Fig. 33

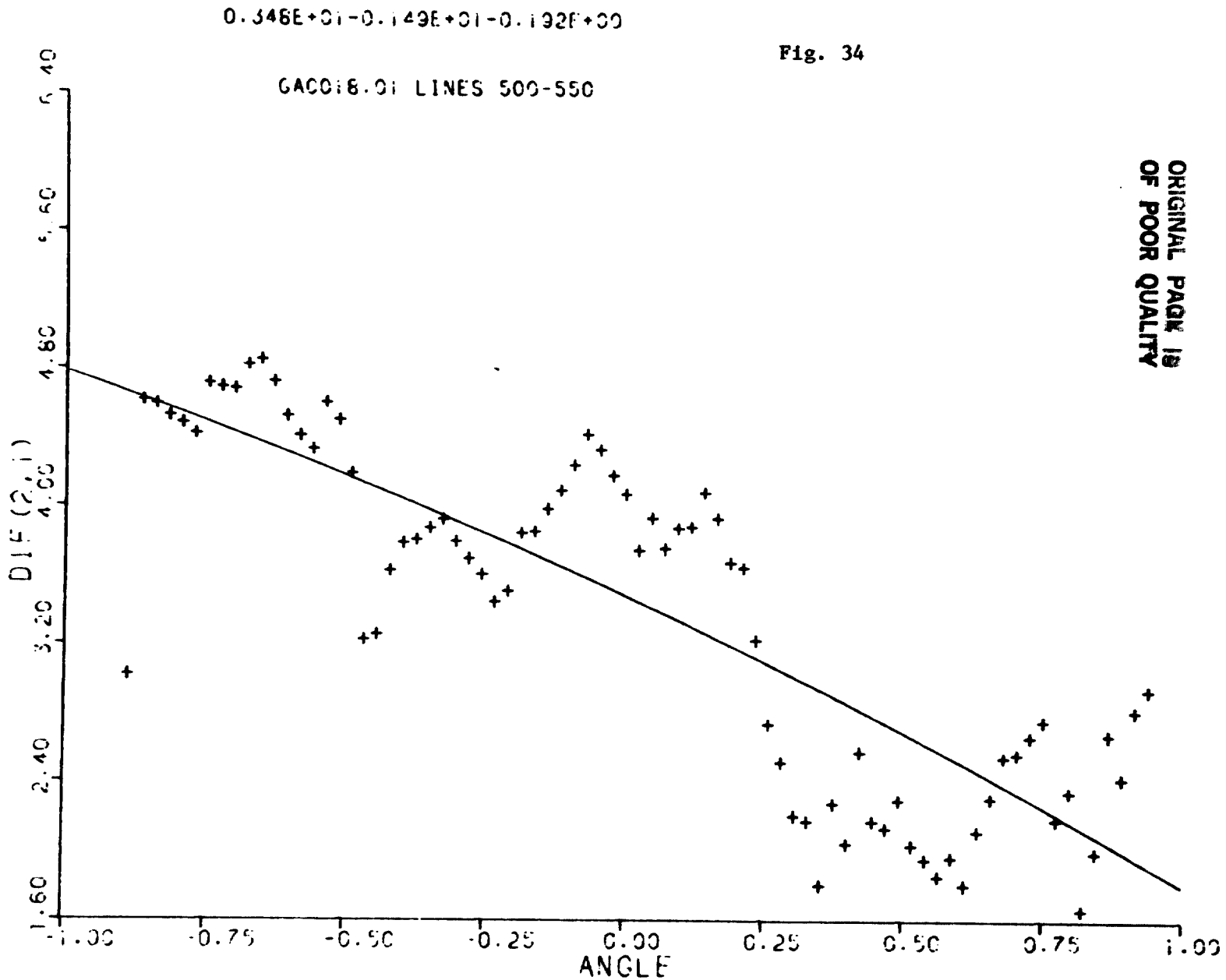

Fig. 34

Fig. 35

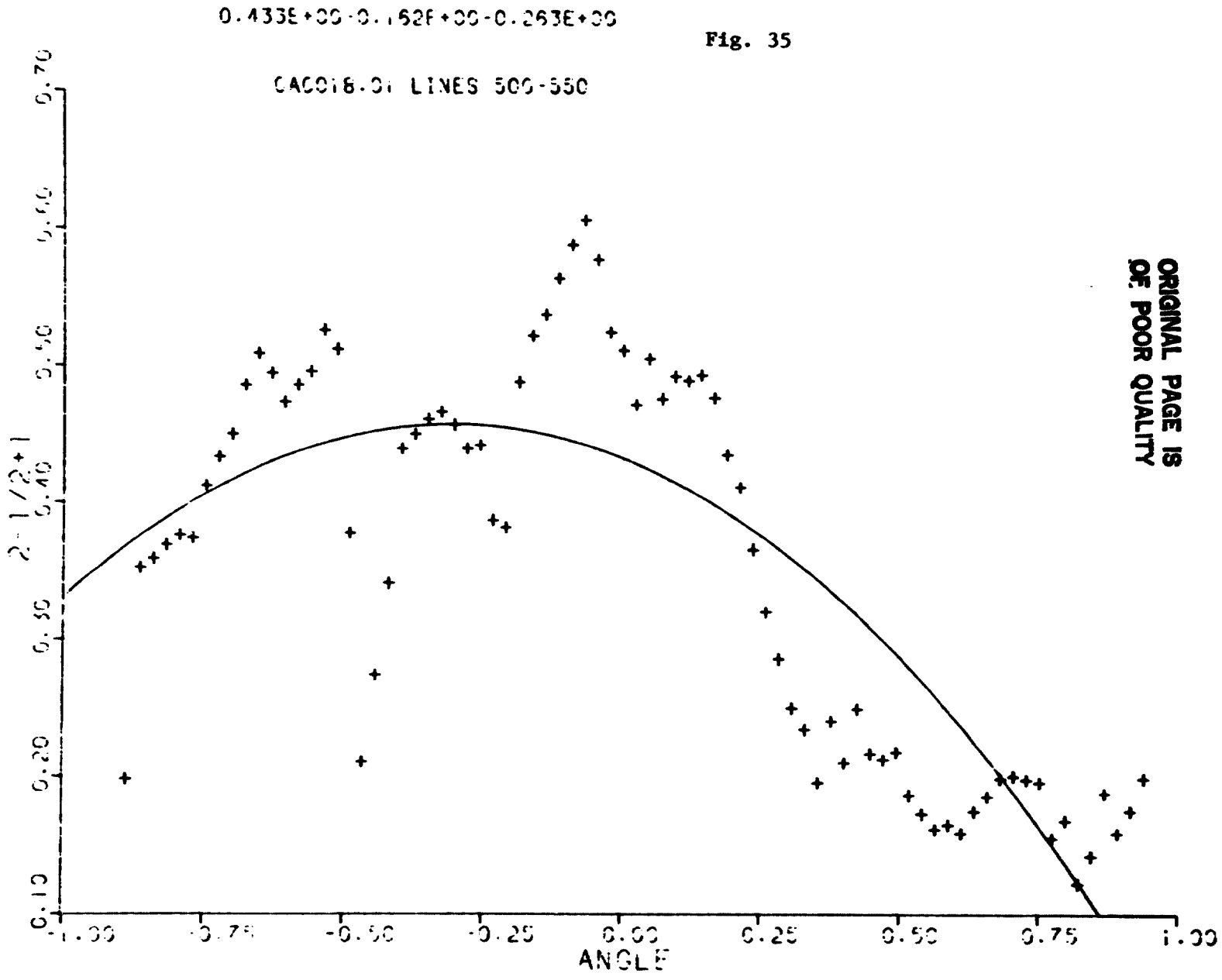

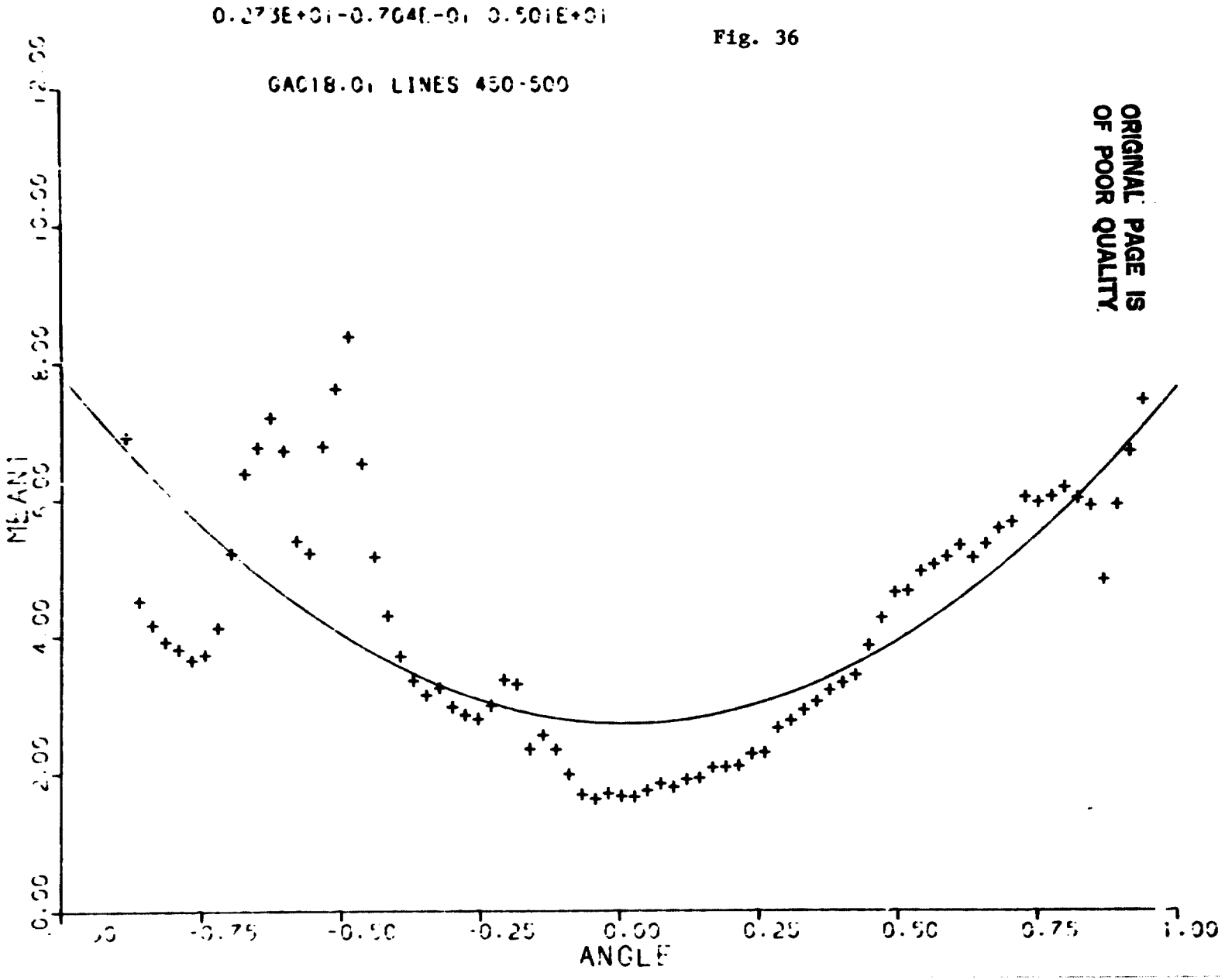

Fig. 36

Fig. 37

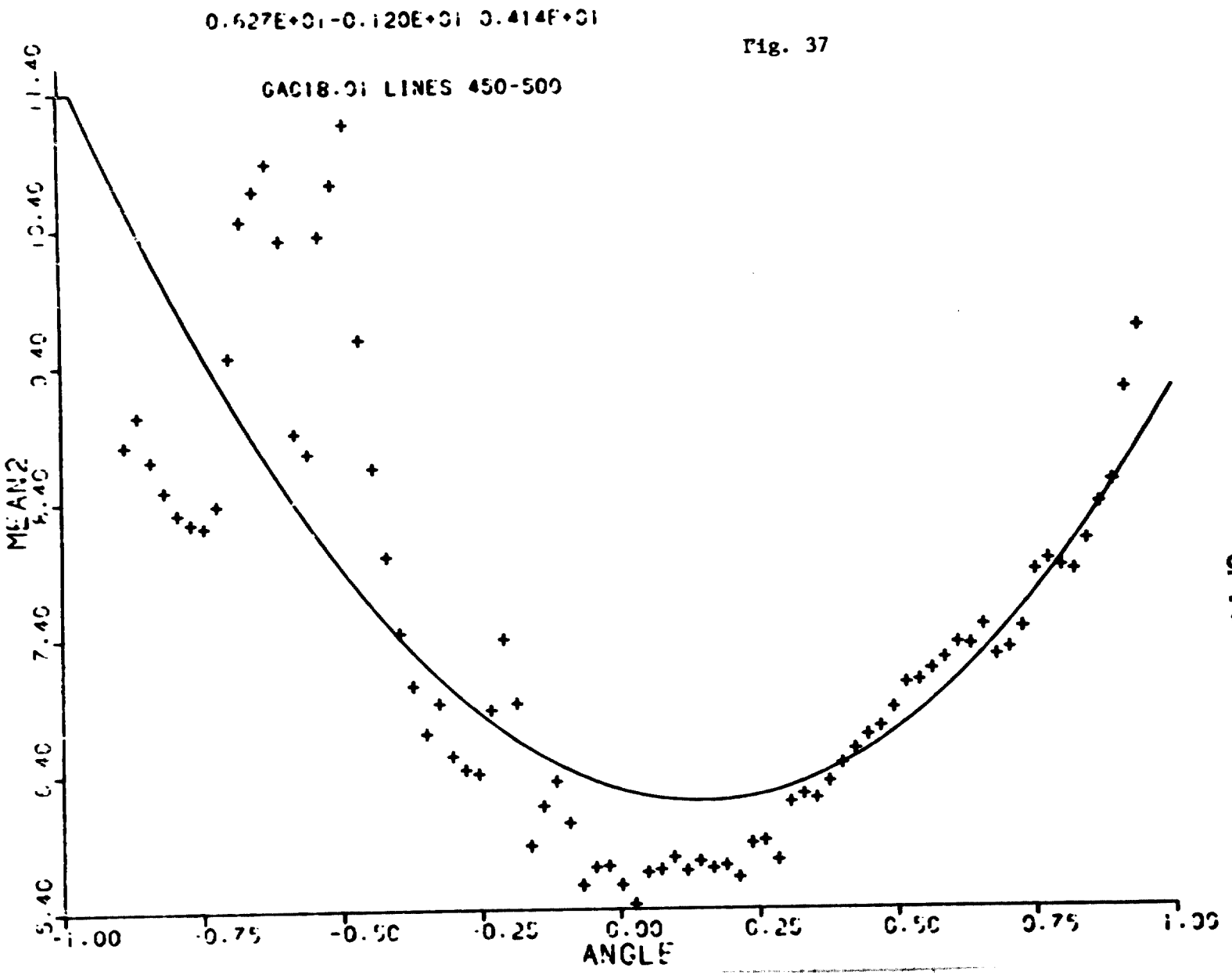

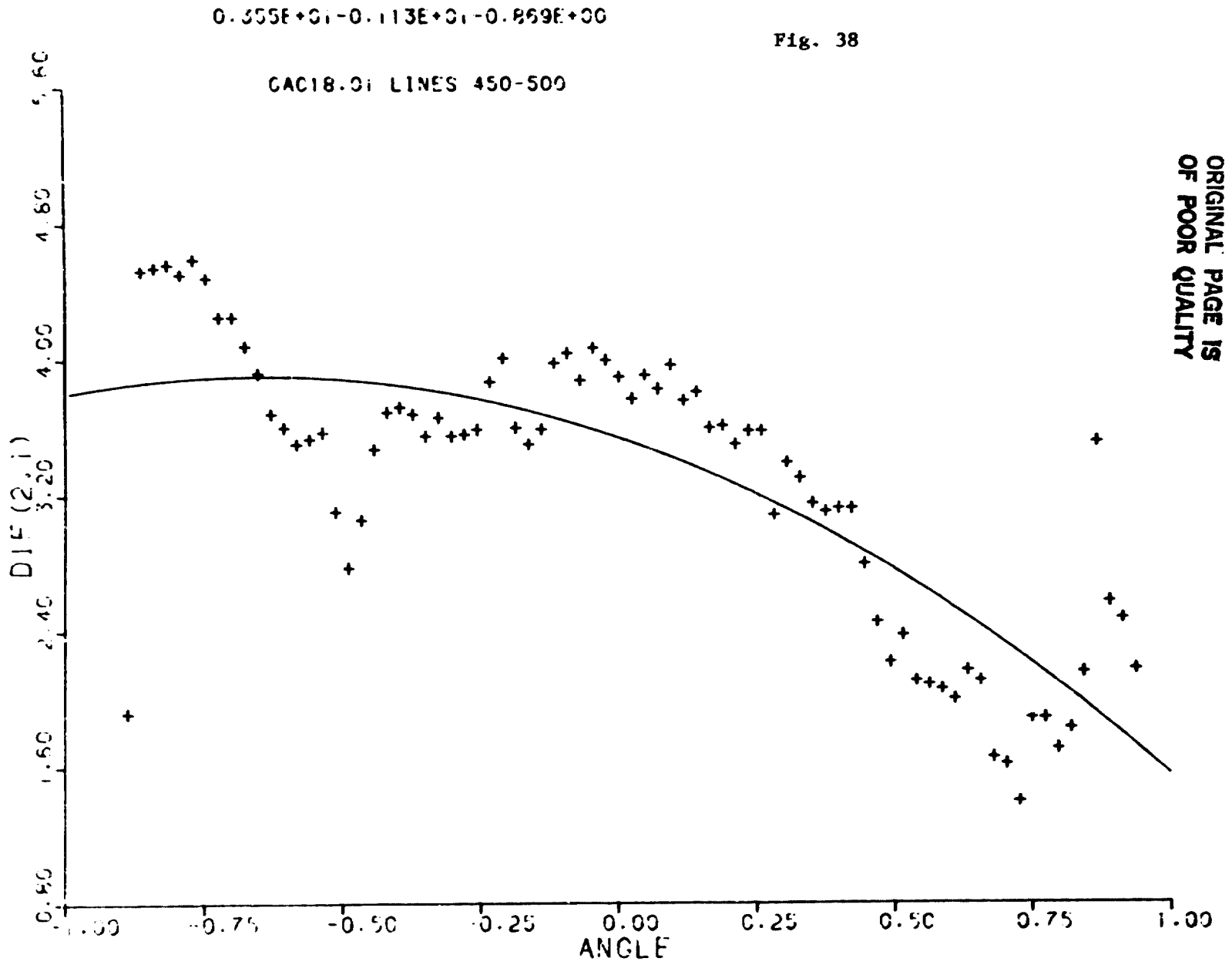

Fig. 38

0.411E+00-0.596E-01-0.343E+00

Fig. 39

CAC18.01 LINES 450-500

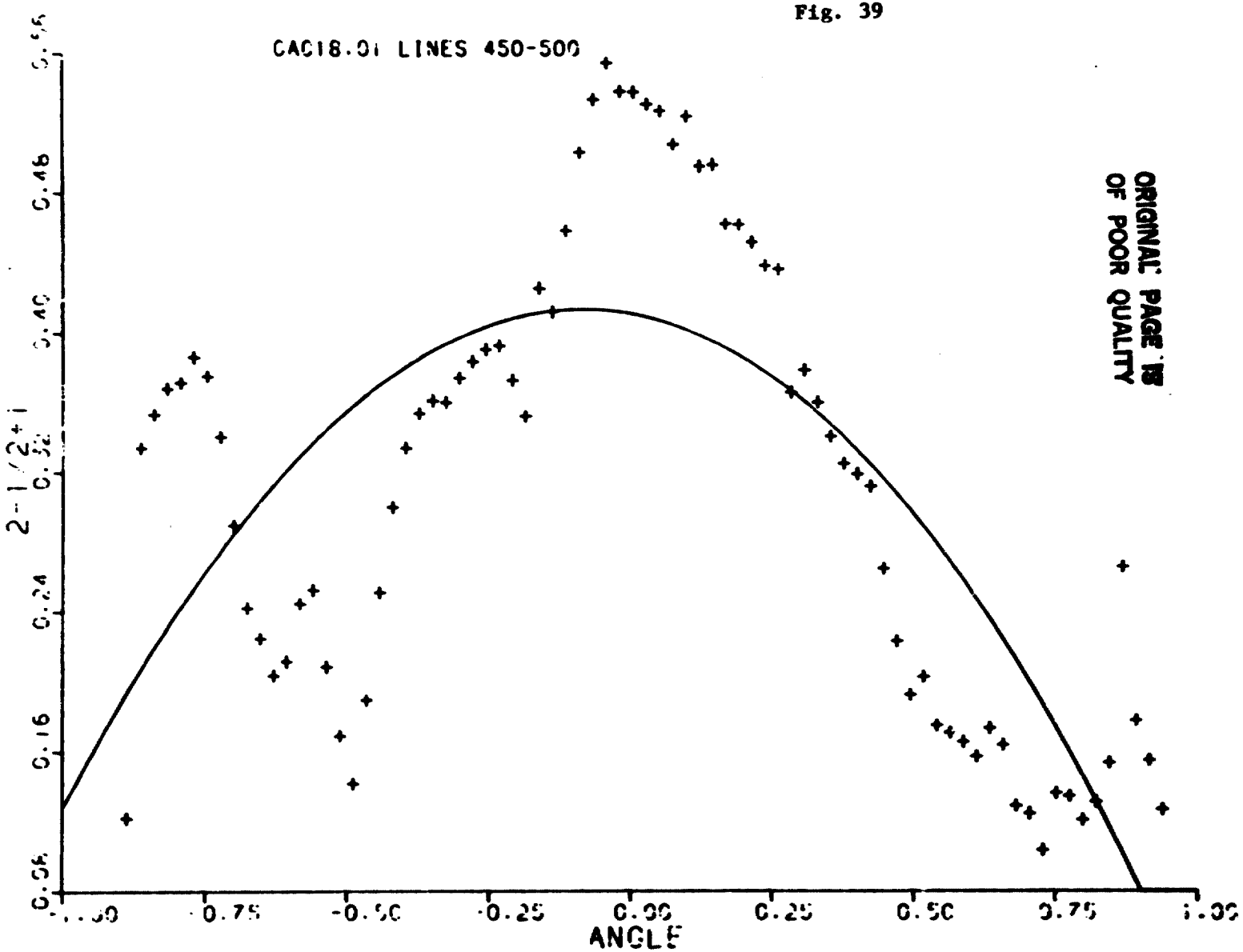

0.297E+01 0.633E+00 0.752E+01

Fig. 40

C-2

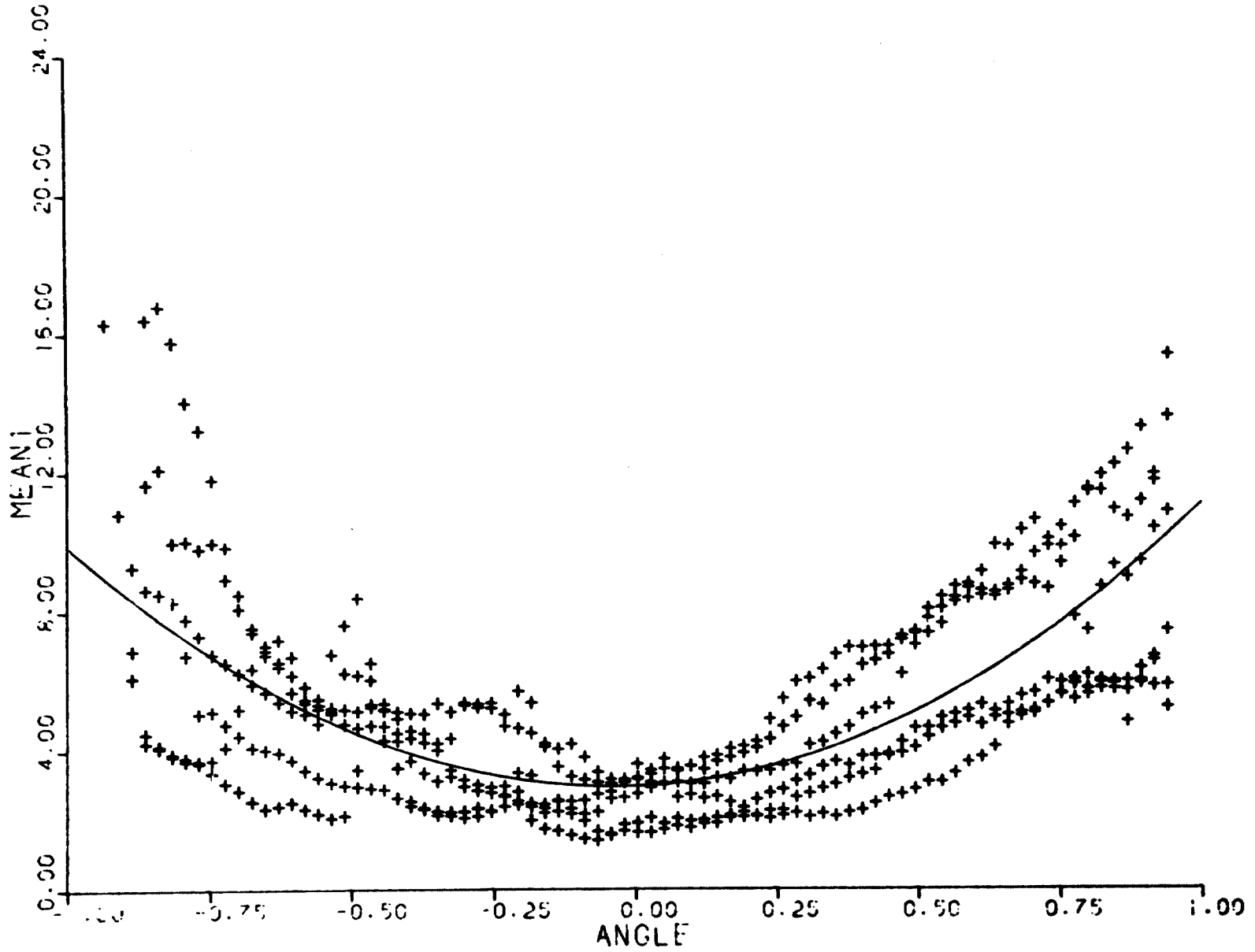

0.748E+01 0.402E-02 0.517E+01

Fig. 41

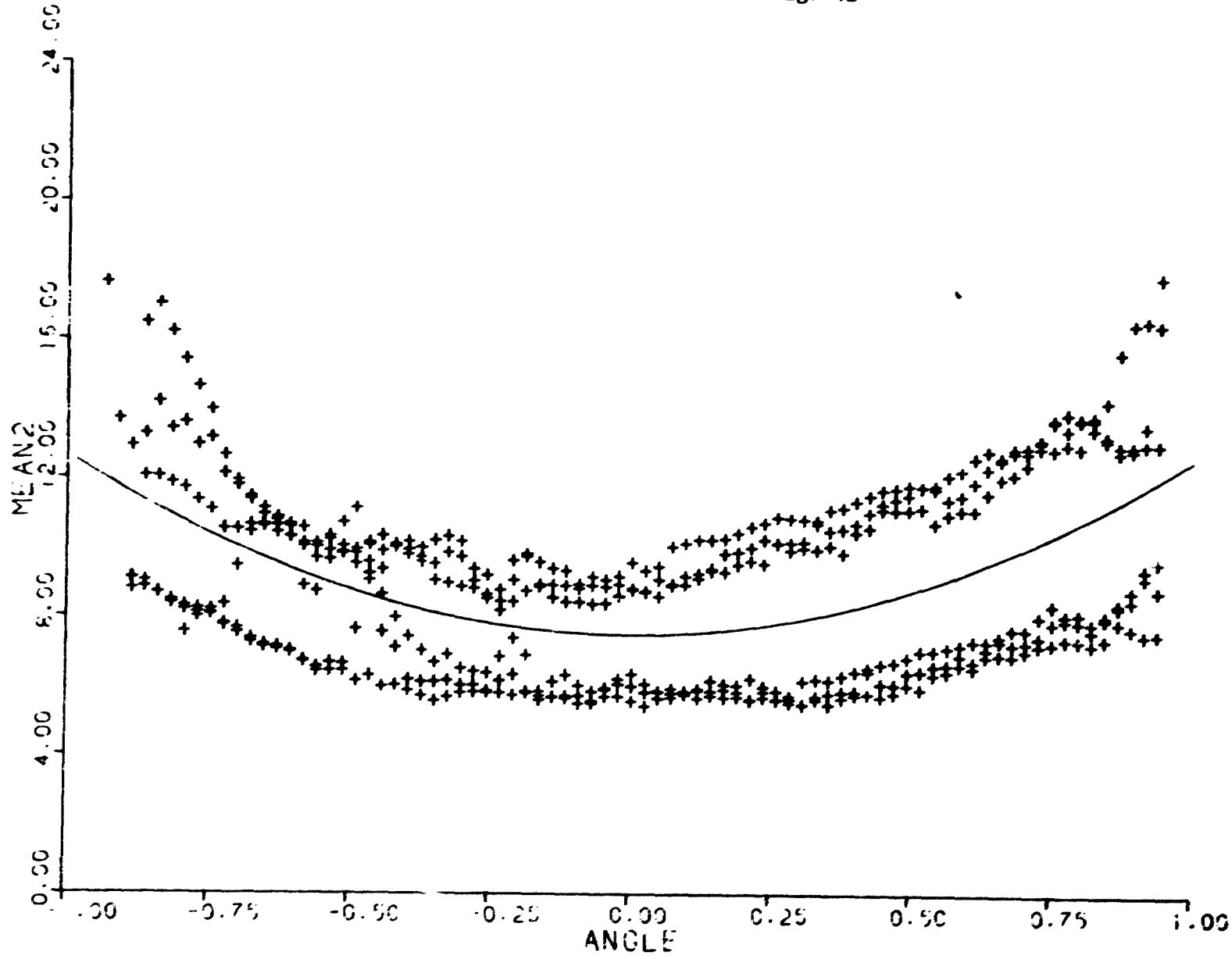

0.450E+01-0.629E+00-0.236E+01 Fig. 42

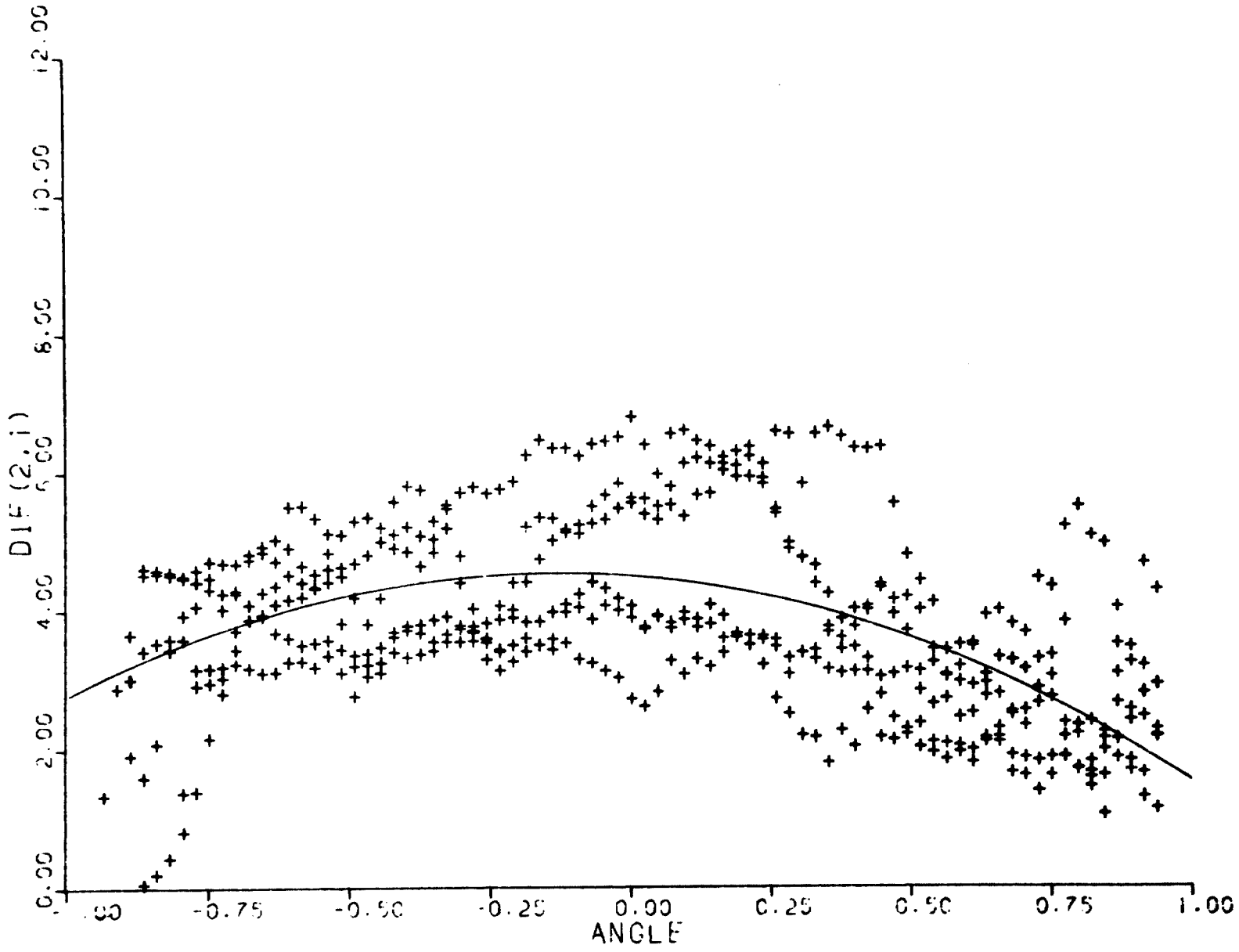

0.418E+00-0.642E-01-0.378E+00 Fig. 43

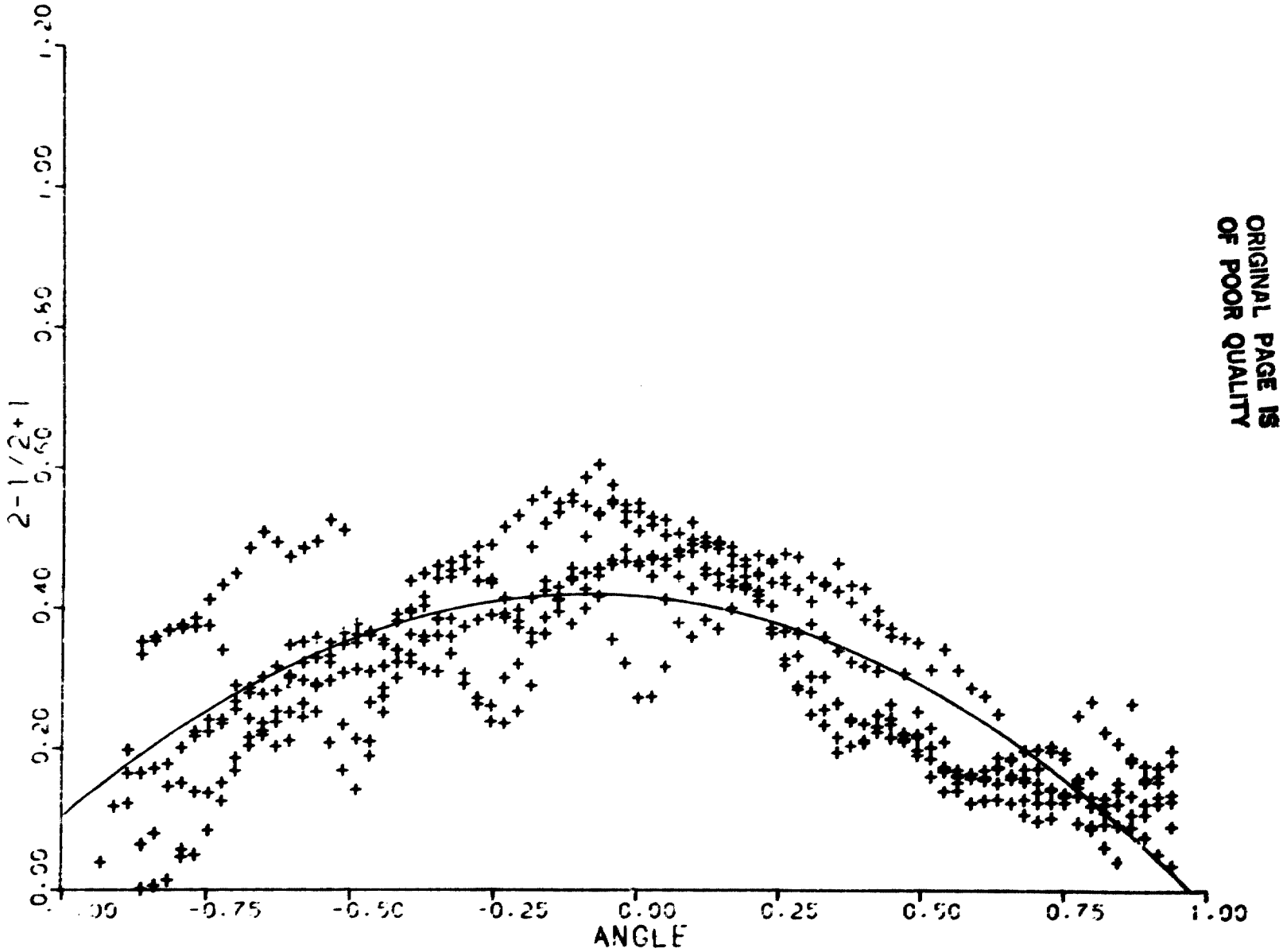

Fig. 44

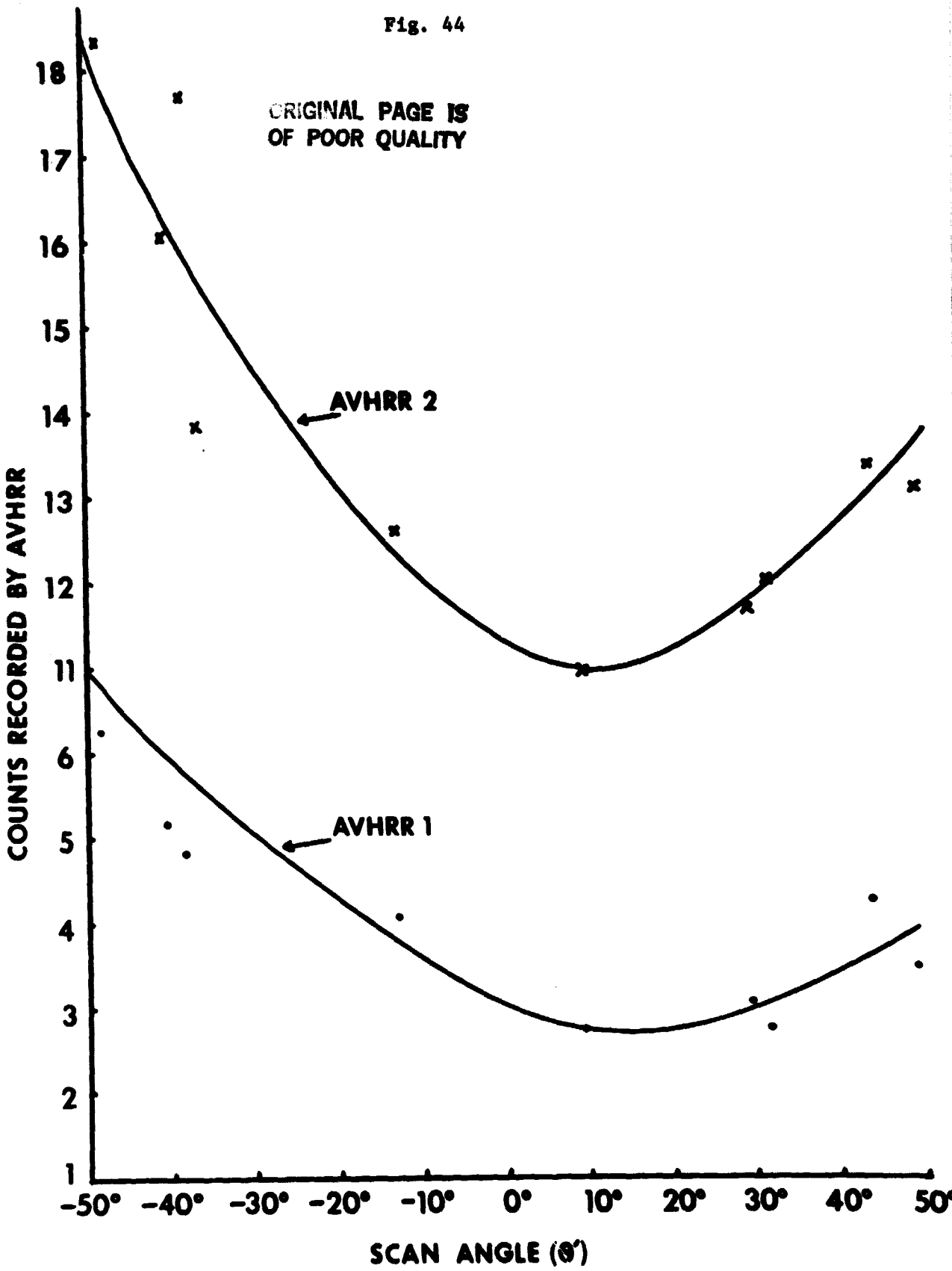

14.49 -0.57 0.01

Fig. 45A.

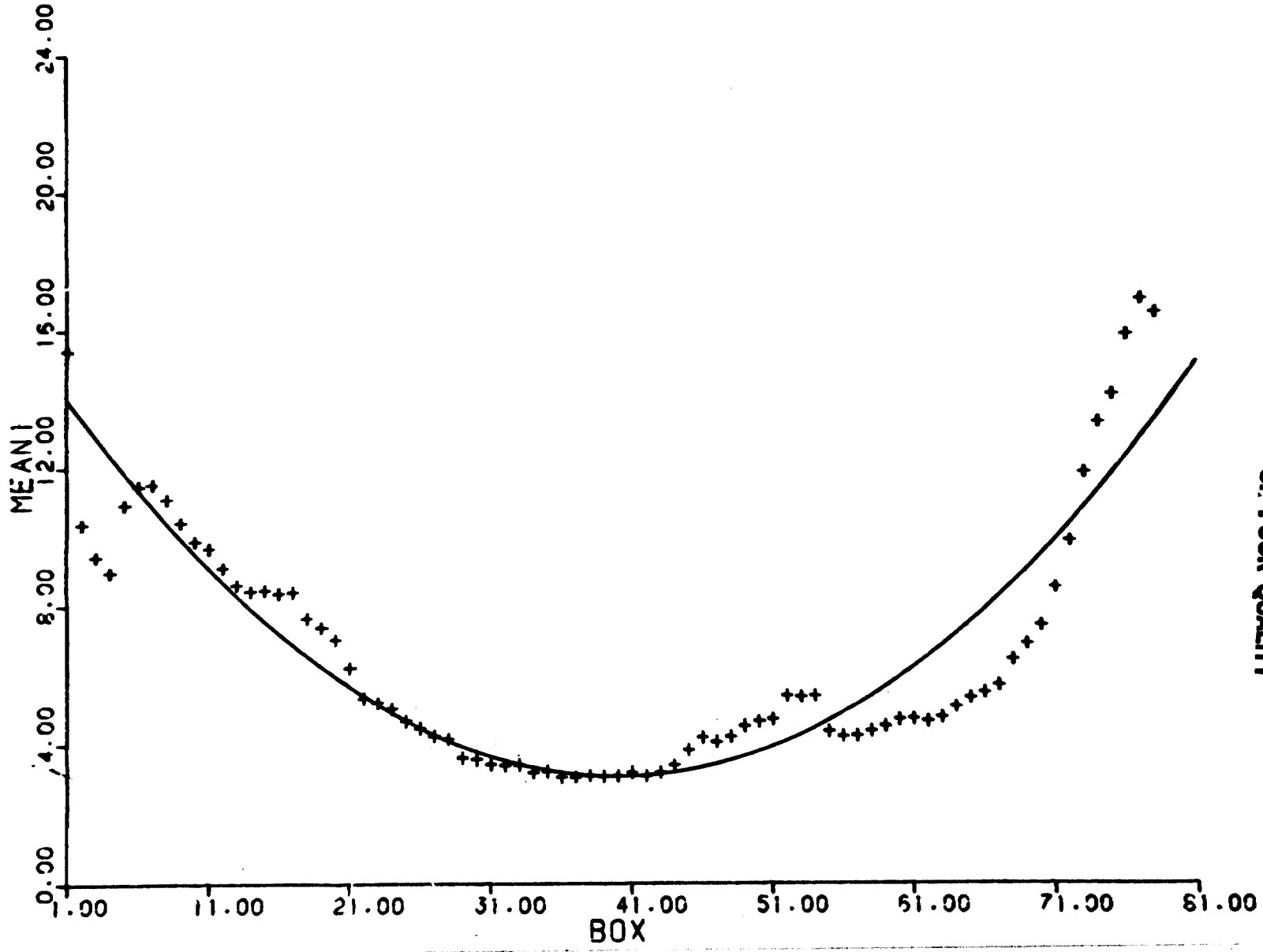

16.00 -0.33 0.00

Fig. 45b.

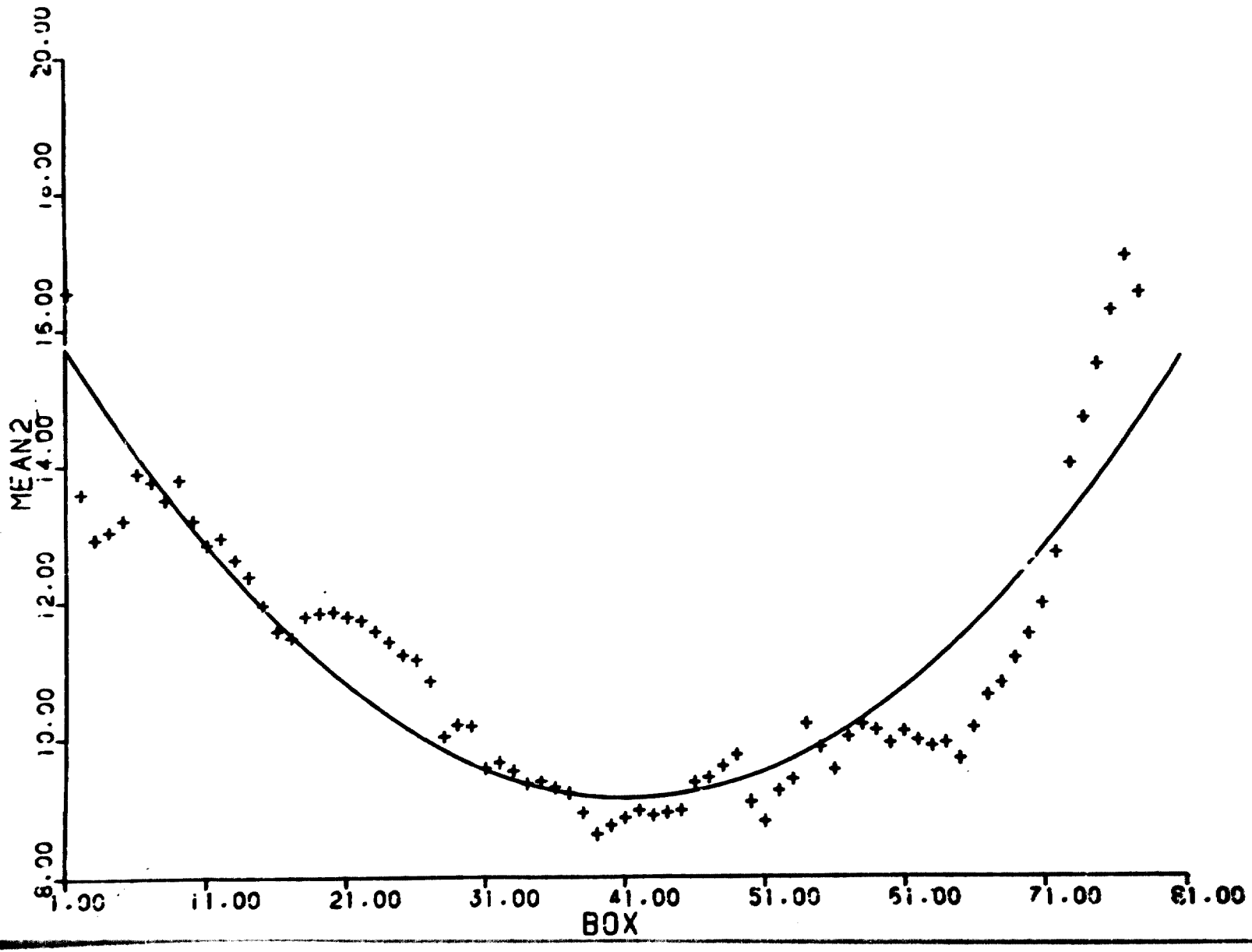

Fig. 45c.

98.53 1.07 -0.01

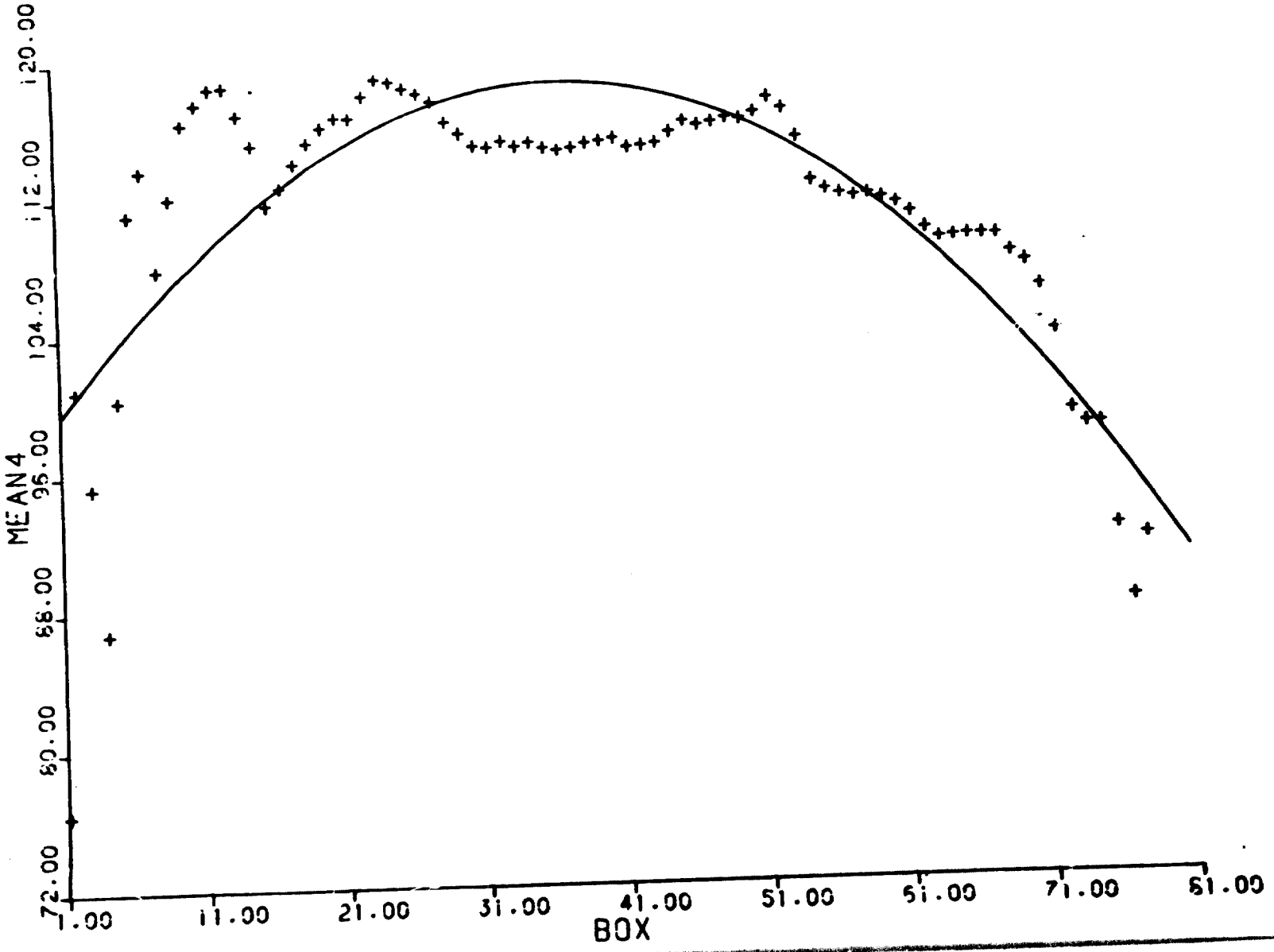

Fig. 46

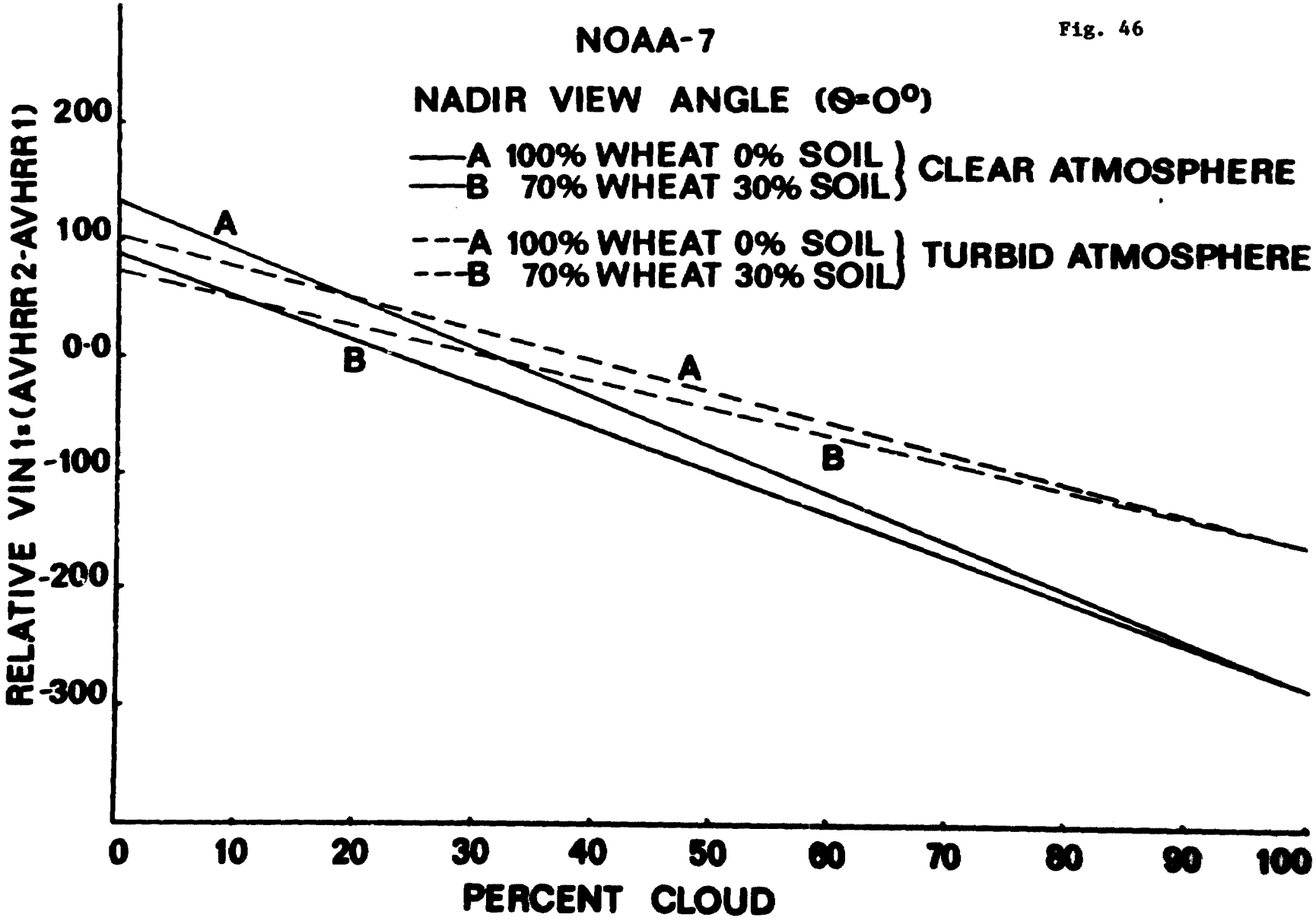

Fig. 47

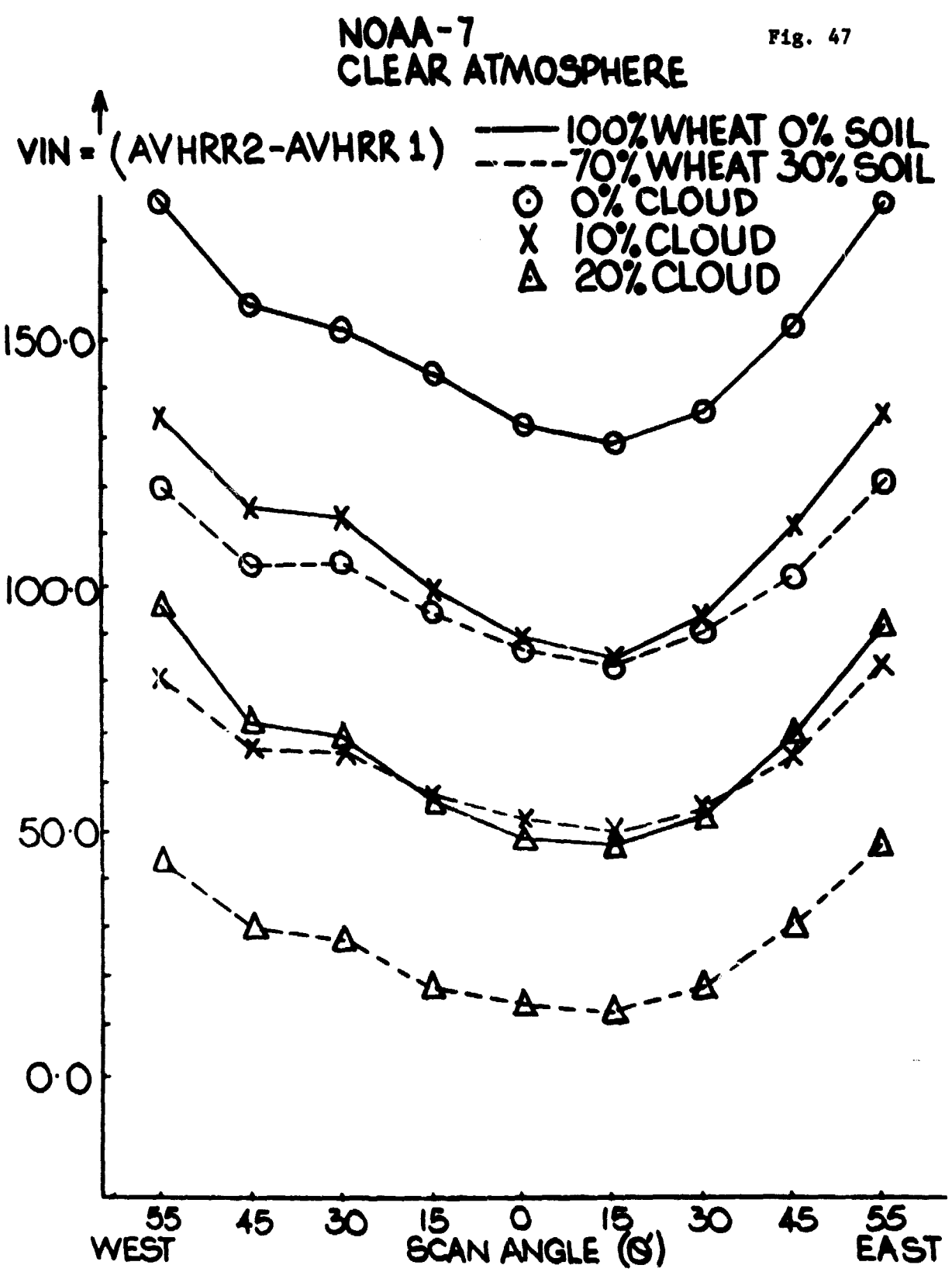

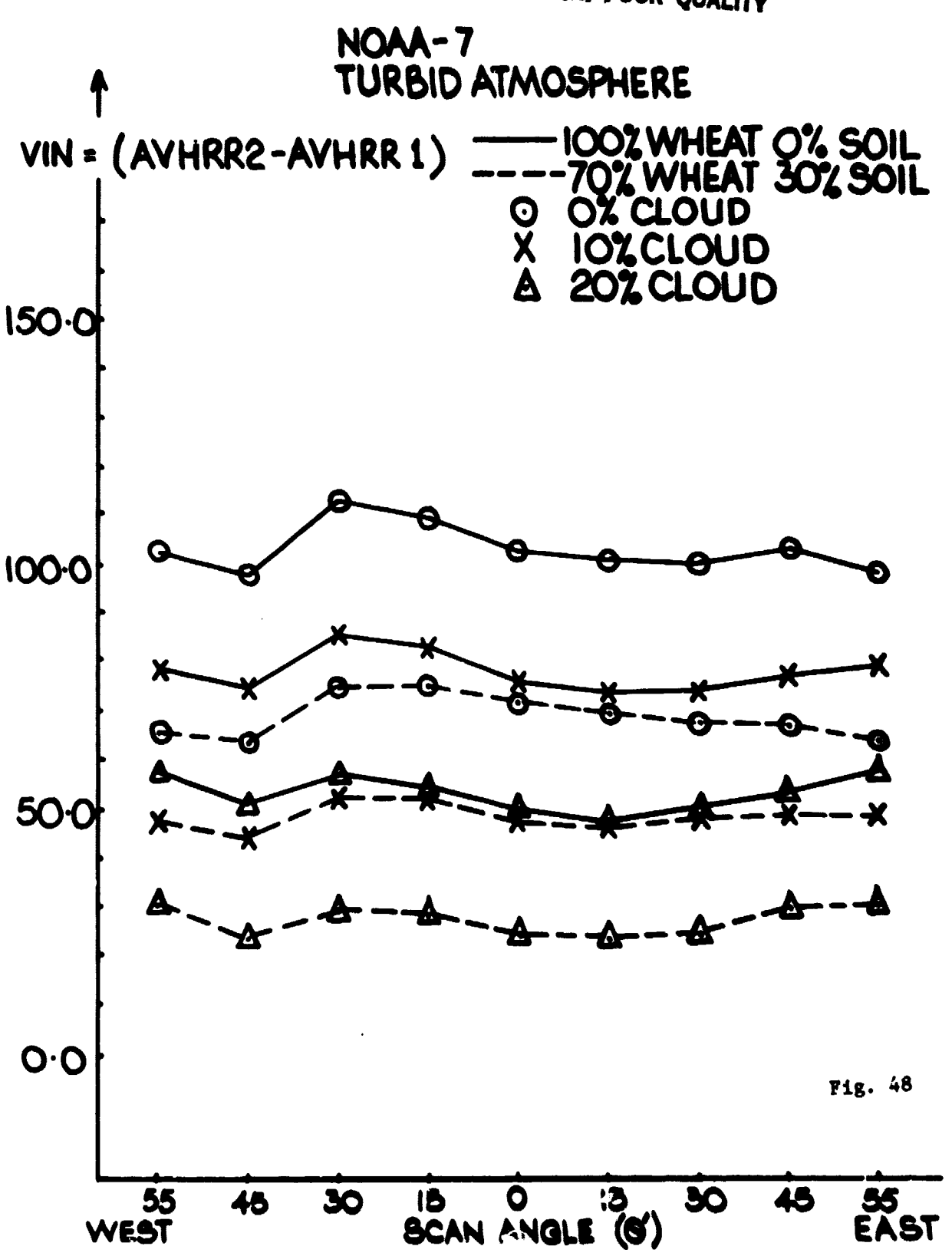

Fig. 48

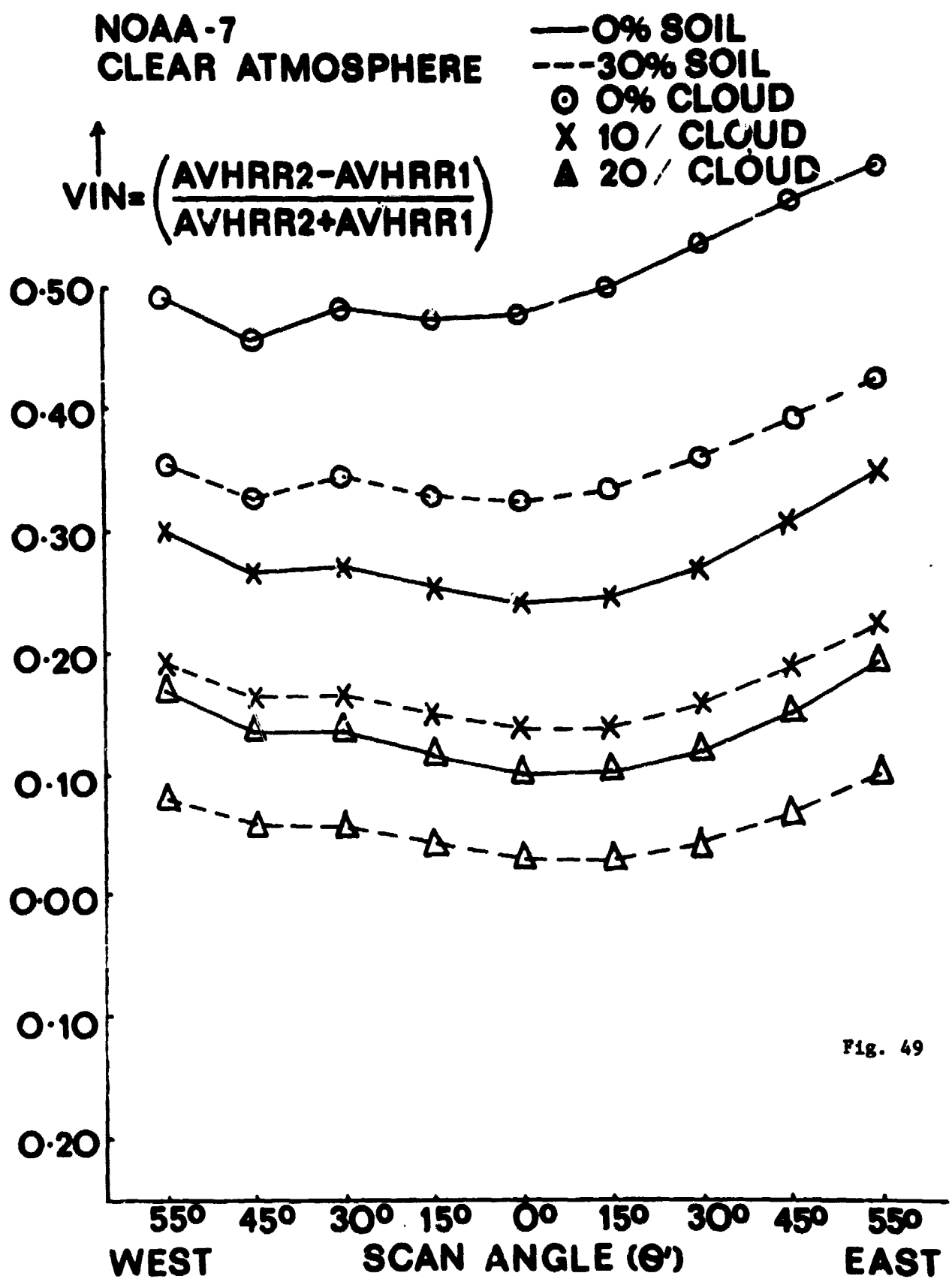

Fig. 49

NOAA-7
TURBID ATMOSPHERE

Fig. 50

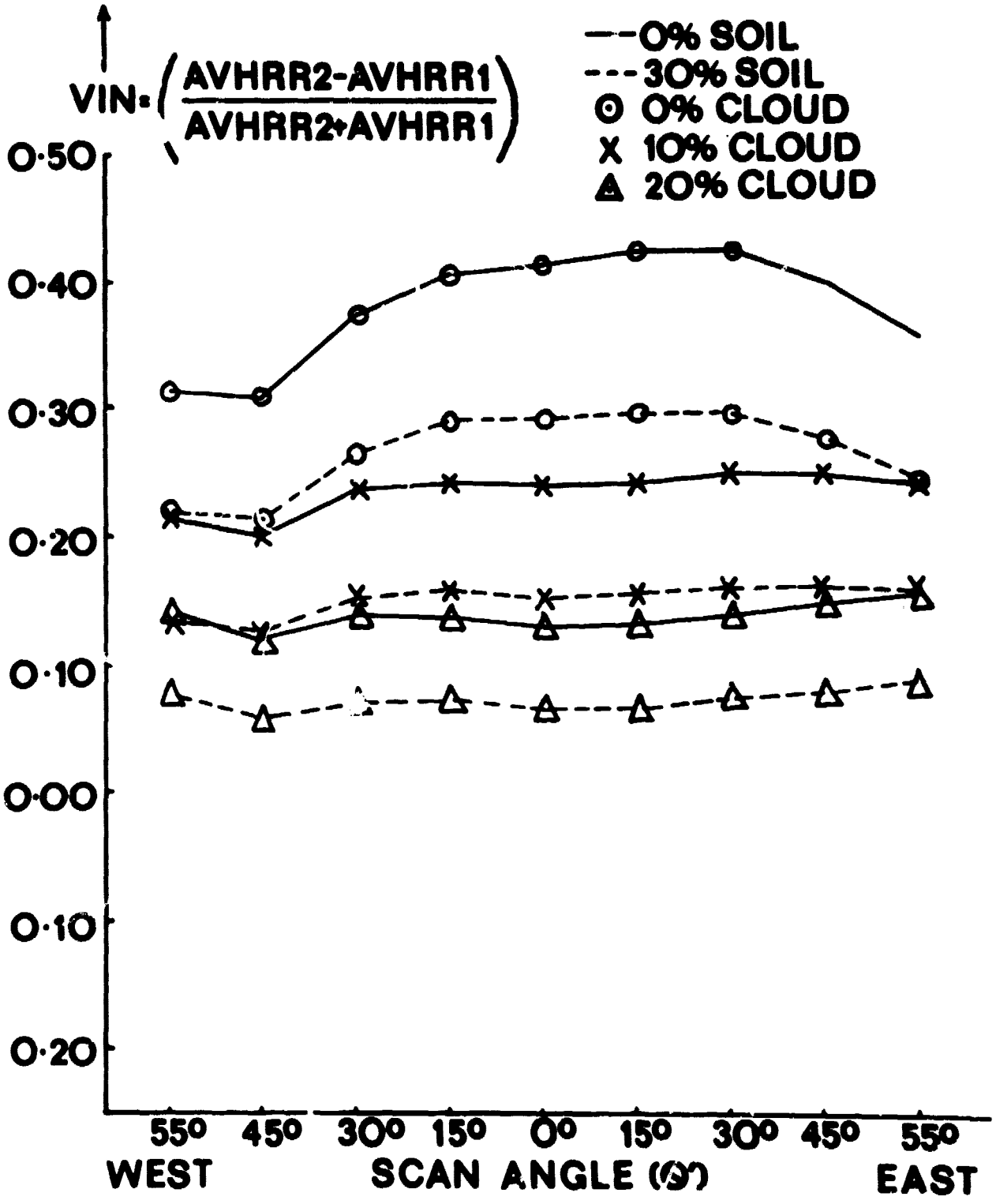

SIMULATED SENSOR RESPONSE
NOAA AVHRR CHANNEL 1
WHEAT CANOPY
NOAA=8 GROWTHST=3.5

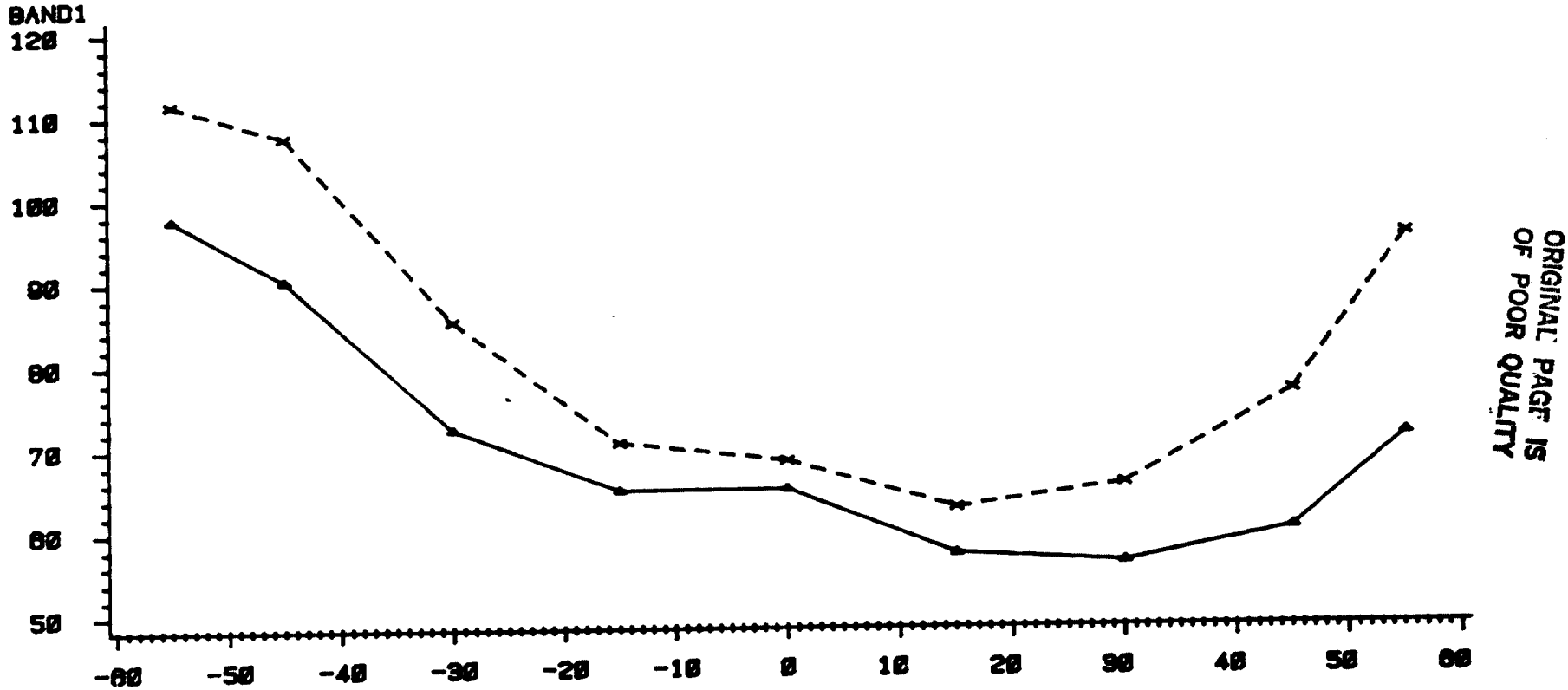

GRAPH NUMBER

VIEW ZENITH DOWNSUN=-60, UPSUN=+60
ATMOSPHERE 1=CLEAR,2=TURBID
GROWTHSTAGE 3.5=BOOT STAGE,
4.5=FULLY HEADED, 5.1=MILK STAGE

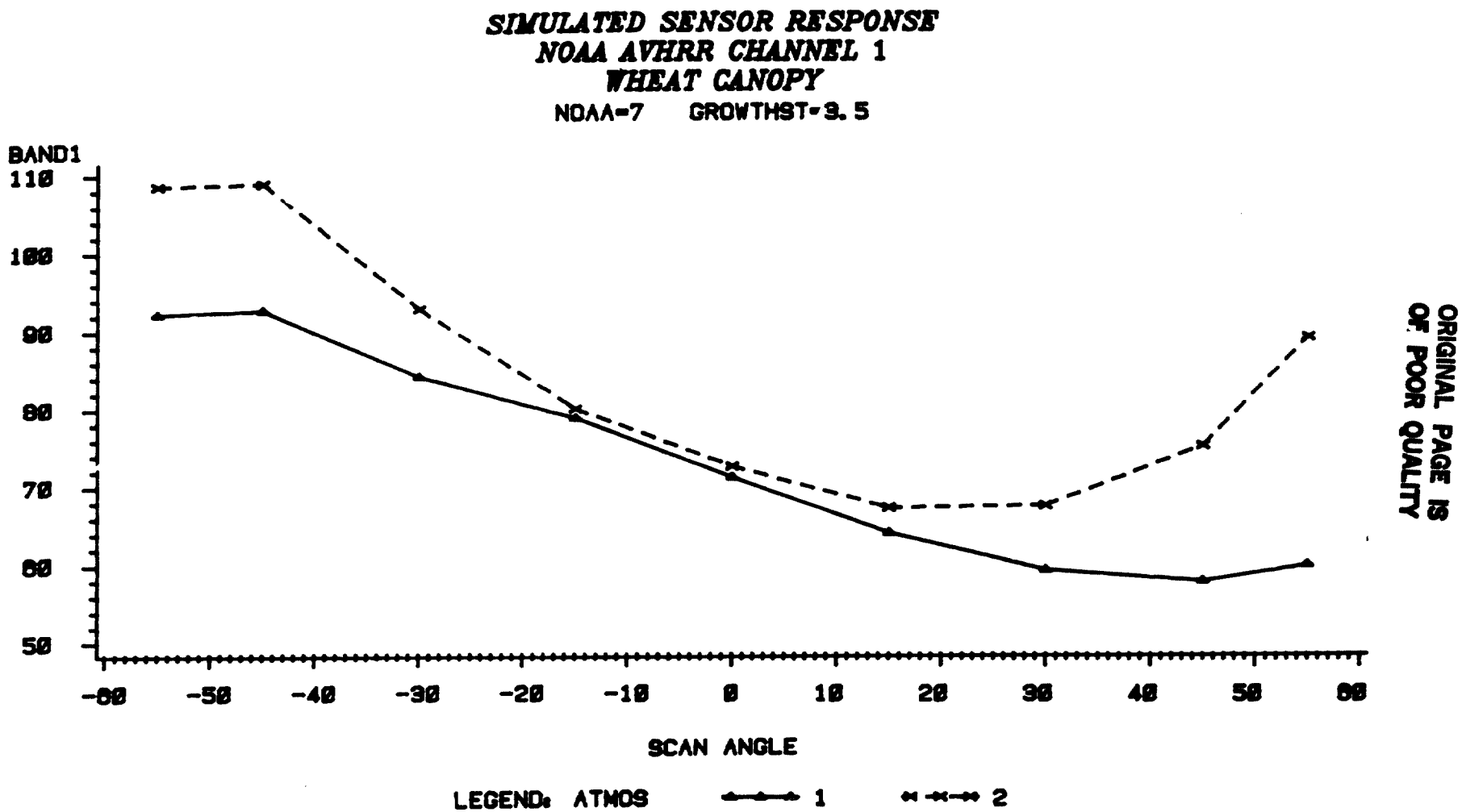

GRAPH NUMBER

VIEW ZENITH DOWNSUN=-60, UPSUN=+60
ATMOSPHERE 1=CLEAR,2=TURBID
GROWTHSTAGE 3.5=BOOT STAGE,
4.5=FULLY HEADED, 5.1=MILK STAGE

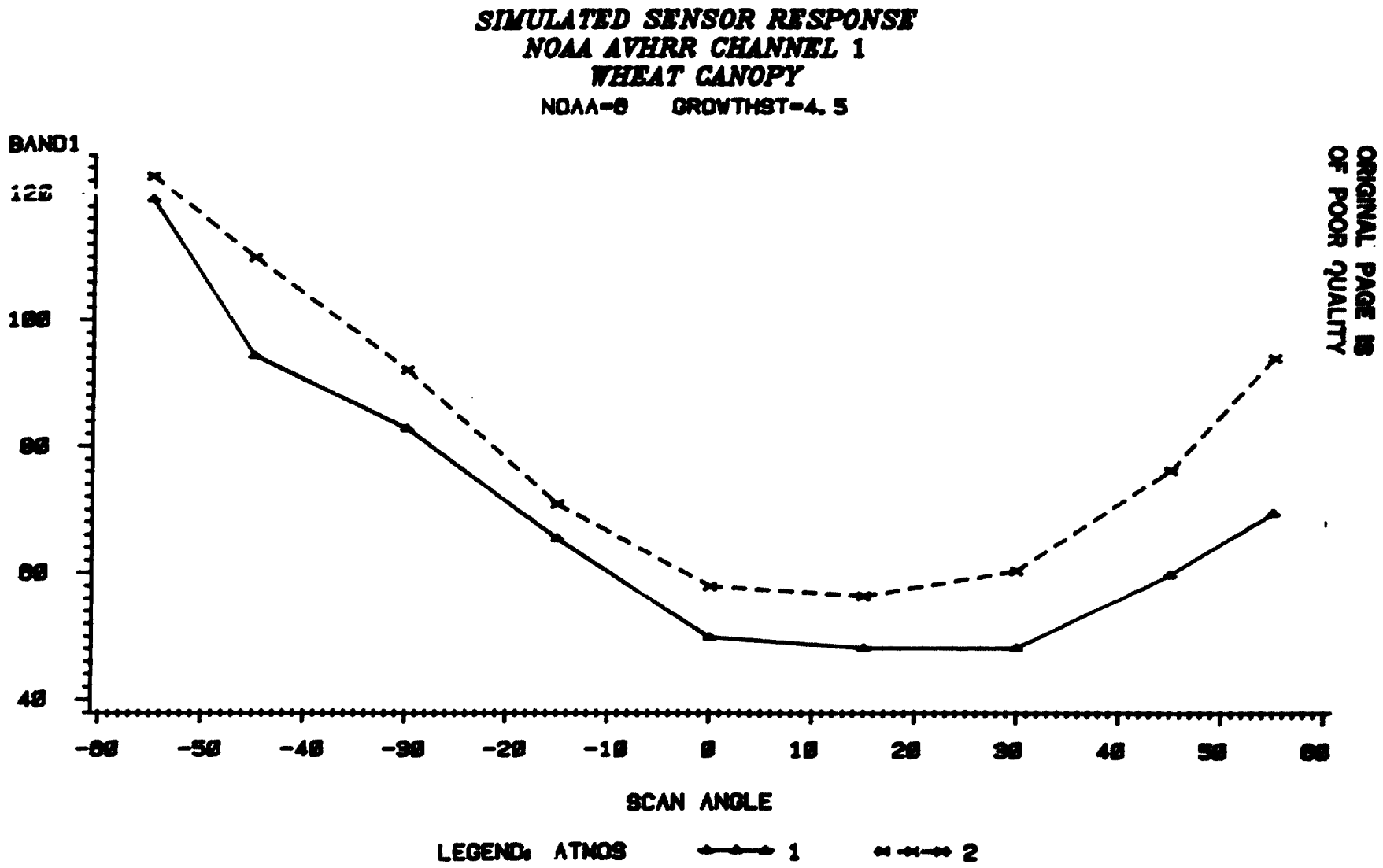

SIMULATED SENSOR RESPONSE
NOAA AVHRR CHANNEL 1
WHEAT CANOPY

NOAA=7 GROWTHST=4.5

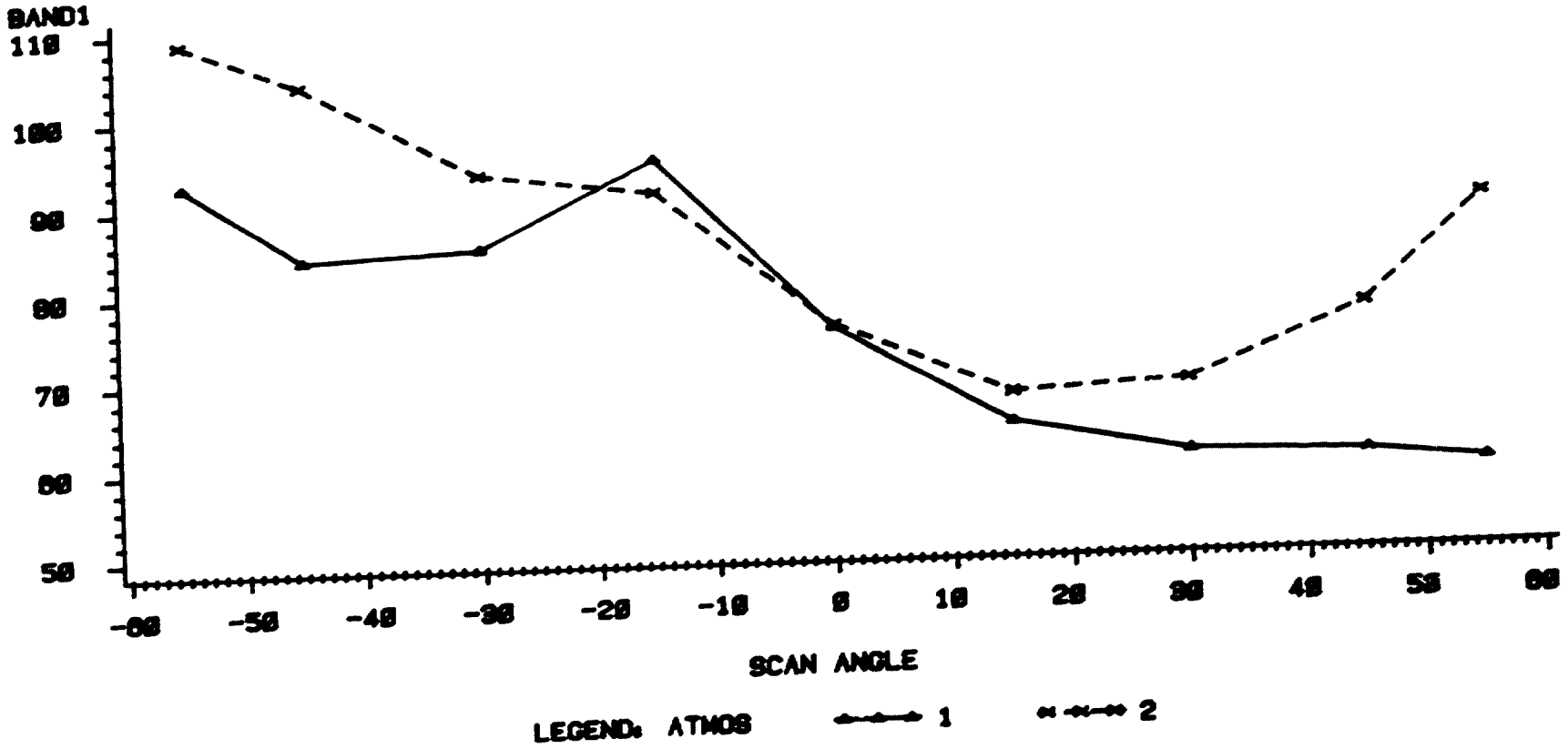

GRAPH NUMBER

VIEW ZENITH DOWNSUN=-60, UPSUN=+60
ATMOSPHERE 1=CLEAR,2=TURBID
GROWTHSTAGE 3.5=BOOT STAGE,
4.5=FULLY HEADED, 5.1=MILK STAGE

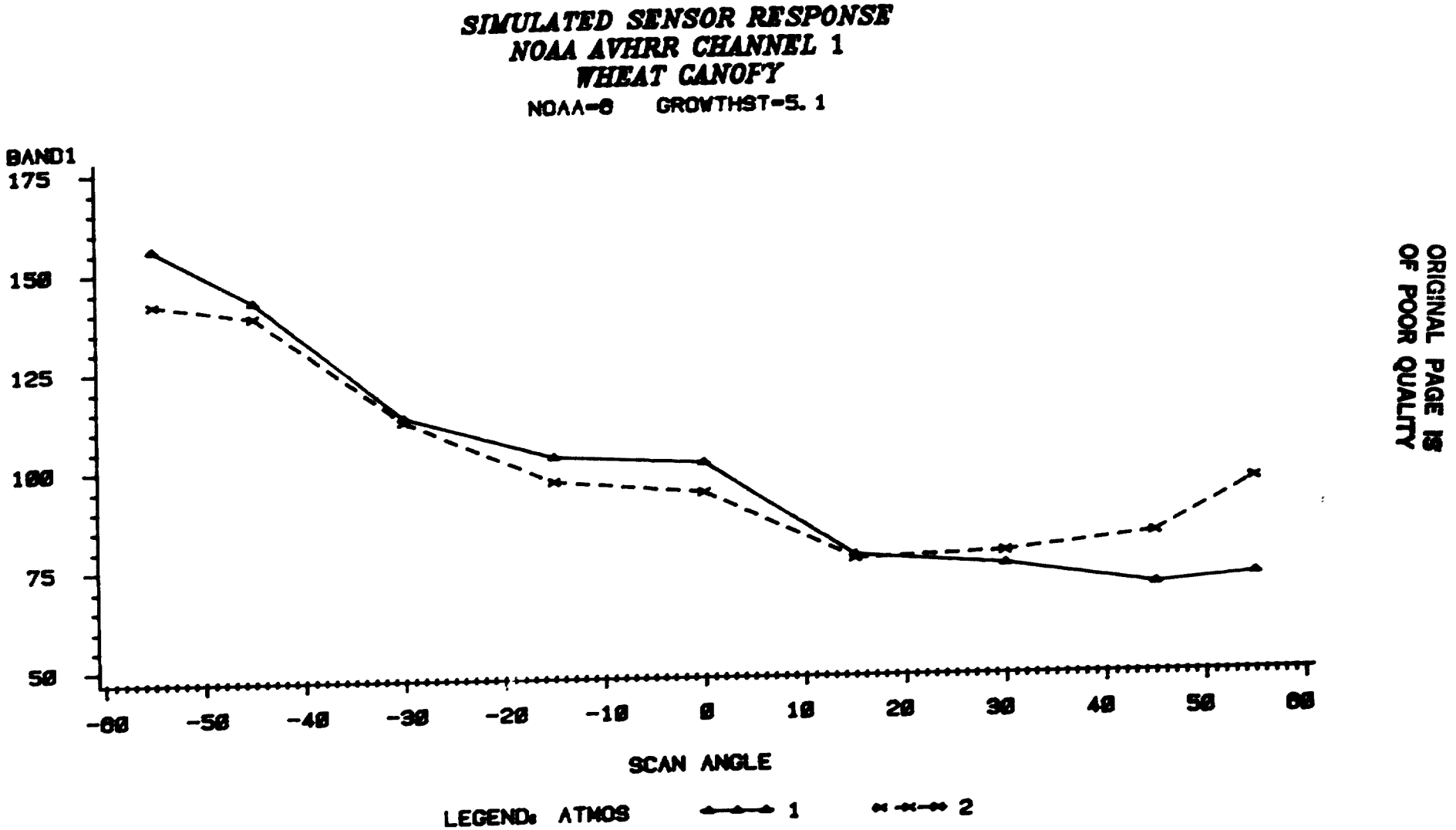

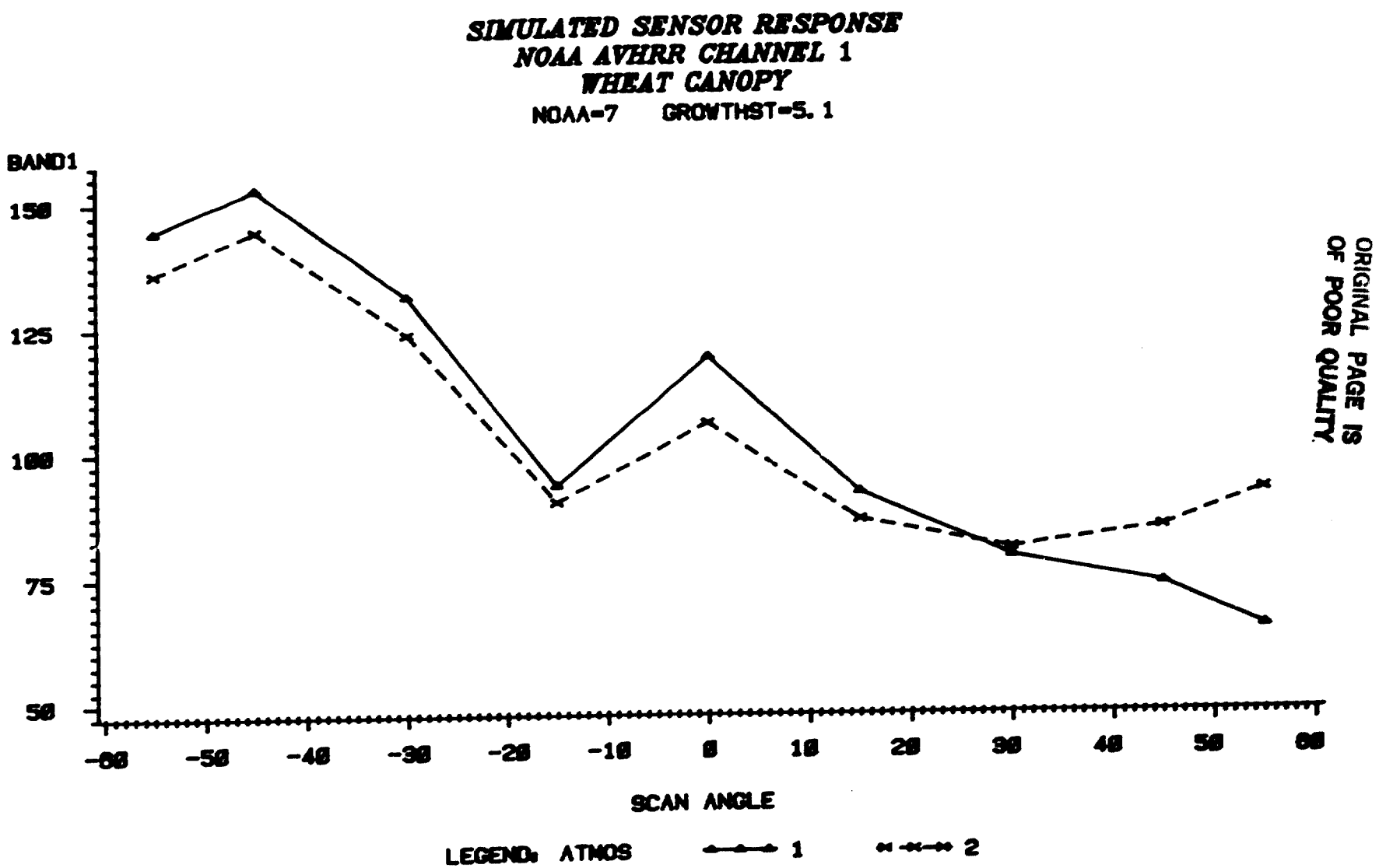

GRAPH NUMBER

VIEW ZENITH DOWNSUN=-60, UPSUN=+60
ATMOSPHERE 1=CLEAR,2=TURBID
GROWTHSTAGE 3.5=BOOT STAGE,
4.5=FULLY HEADED, 5.1=MILK STAGE

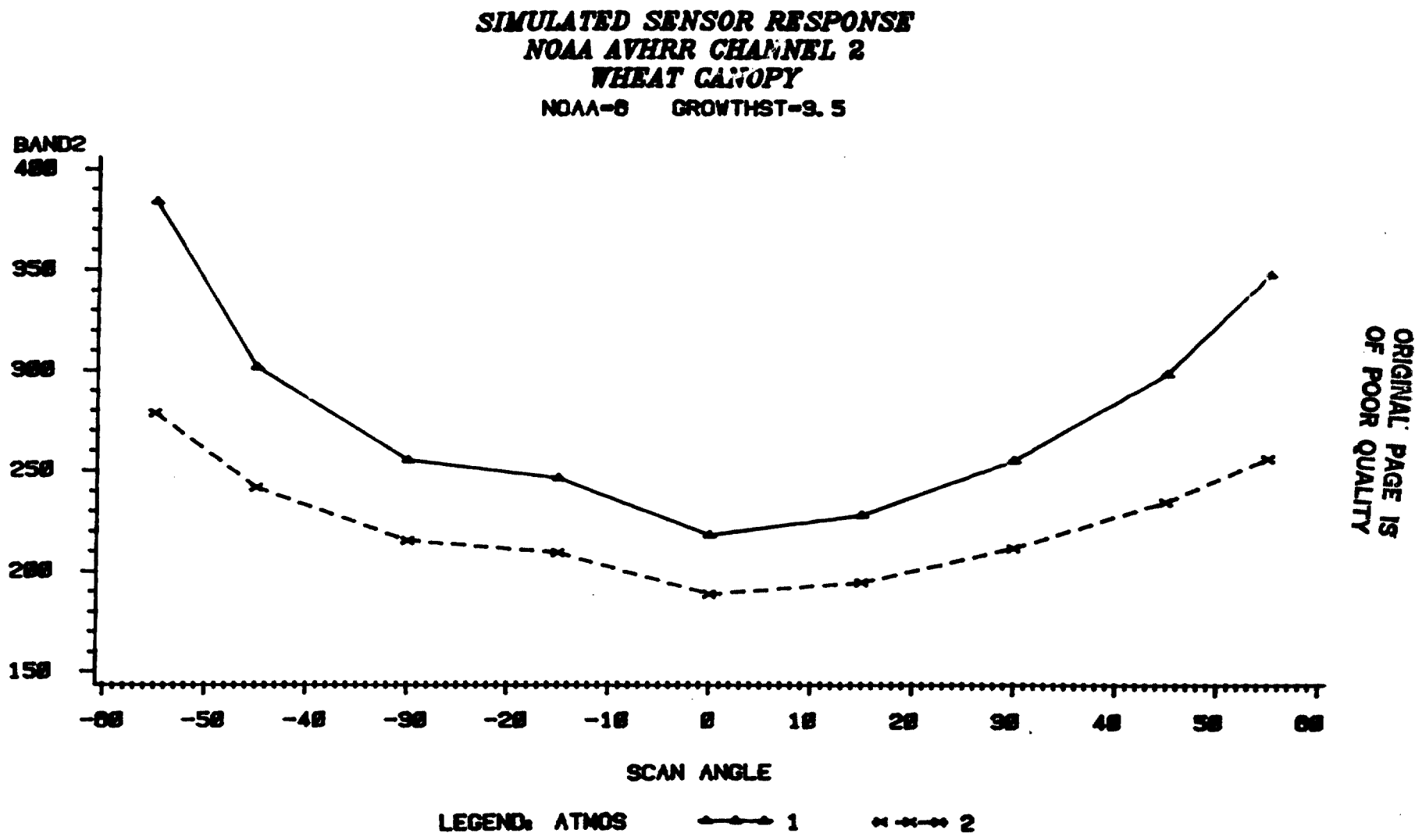

GRAPH NUMBER

VIEW ZENITH DOWNSUN=-60, UPSUN=+60
ATMOSPHERE 1=CLEAR,2=TURBID
GROWTHSTAGE 3.5=BOOT STAGE,
4.5=FULLY HEADED, 5.1=MILK STAGE

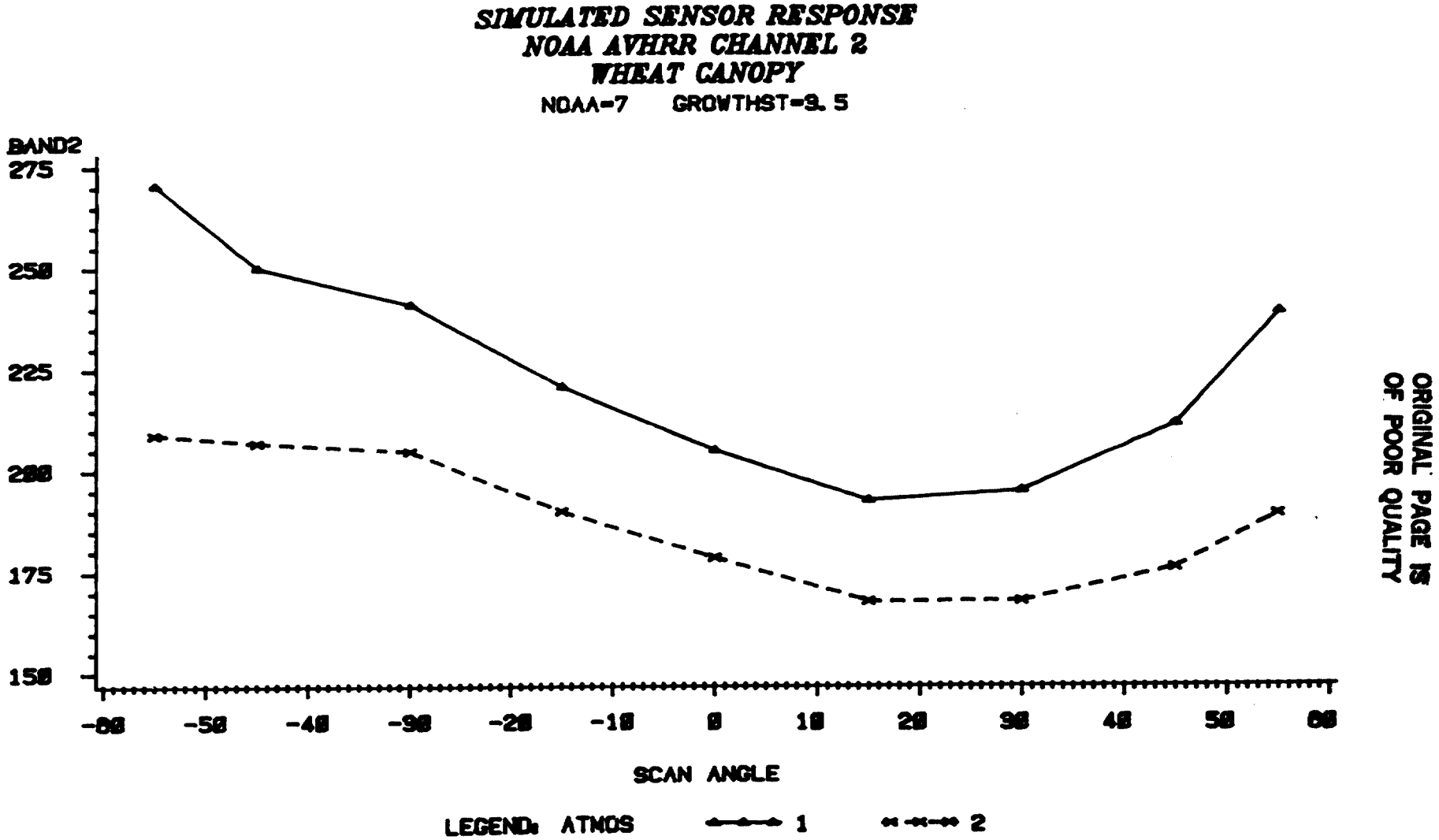

GRAPH NUMBER

VIEW ZENITH DOWNSUN=-60, UPSUN=+60
ATMOSPHERE 1=CLEAR,2=TURBID
GROWTHSTAGE 3.5=BOOT STAGE,
4.5=FULLY HEADED, 5.1=MILK STAGE

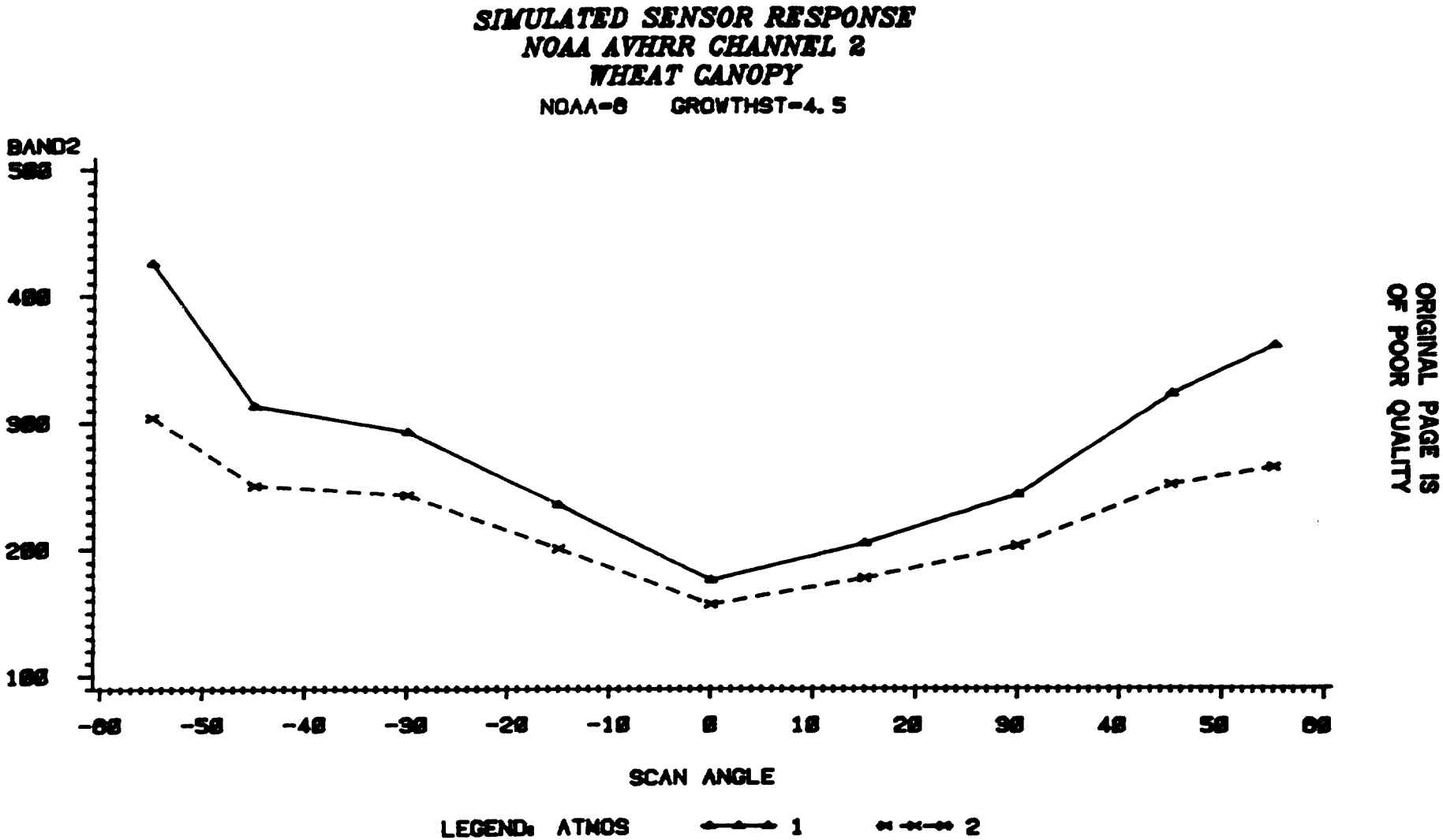

GRAPH NUMBER

VIEW ZENITH DOWNSUN=-60, UPSUN=+60
ATMOSPHERE 1=CLEAR,2=TURBID
GROWTHSTAGE 3.5=BOOT STAGE,
4.5=FULLY HEADED, 5.1=MILK STAGE

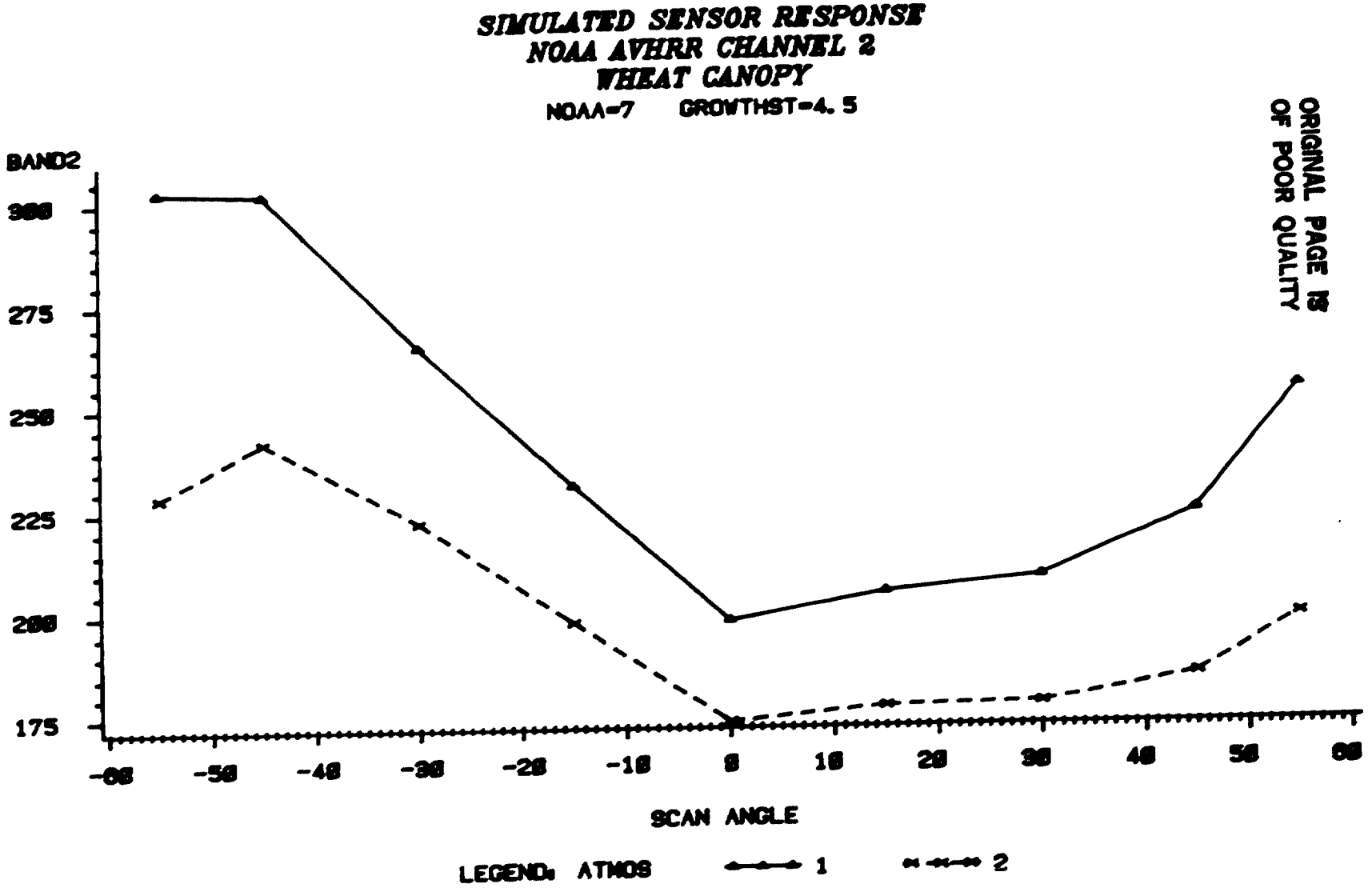

GRAPH NUMBER

VIEW ZENITH DOWNSUN=-60, UPSUN=+60
ATMOSPHERE 1=CLEAR,2=TURBID
GROWTHSTAGE 3.5=BOOT STAGE,
4.5=FULLY HEADED, 5.1=MILK STAGE

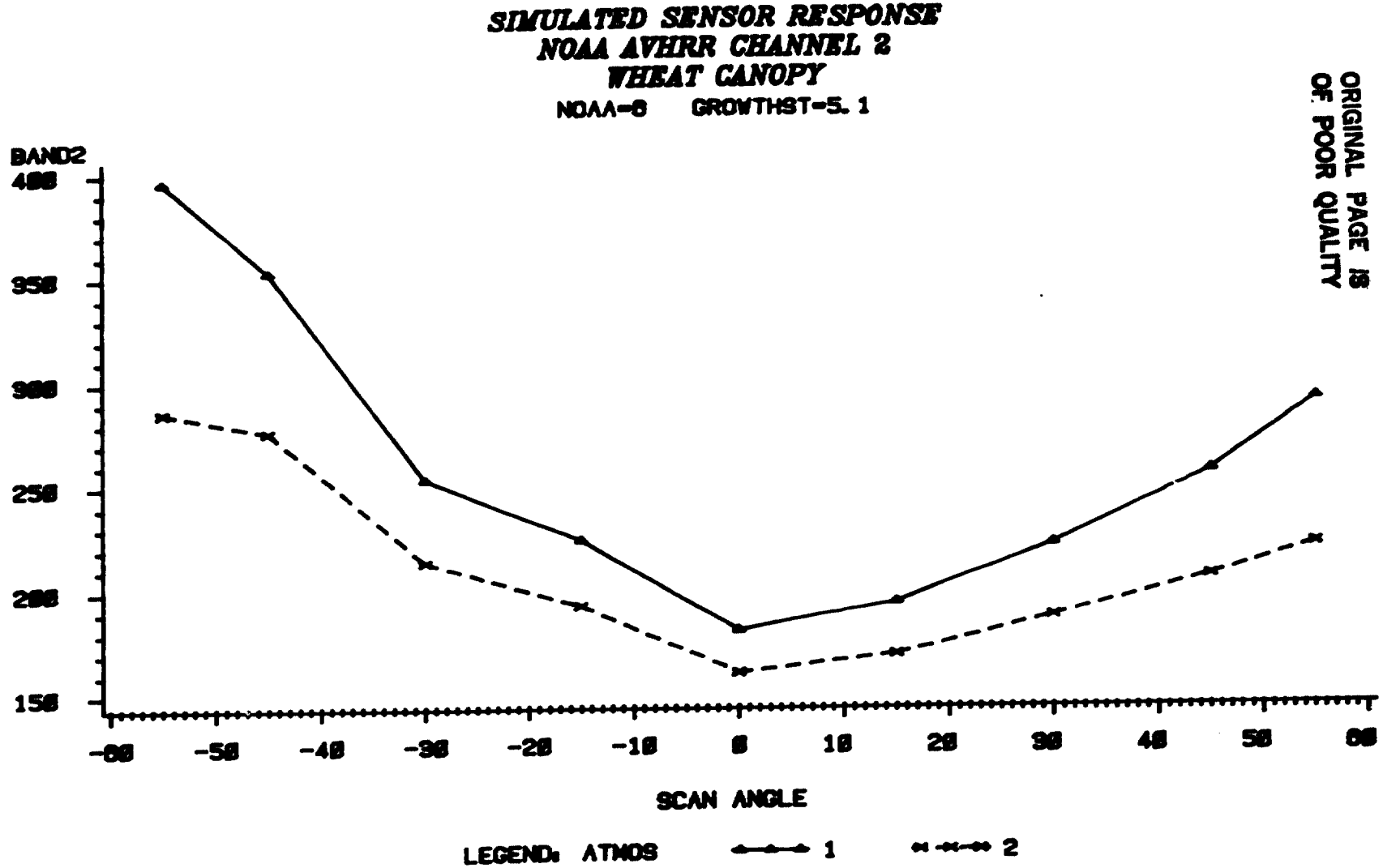

FIG. 62

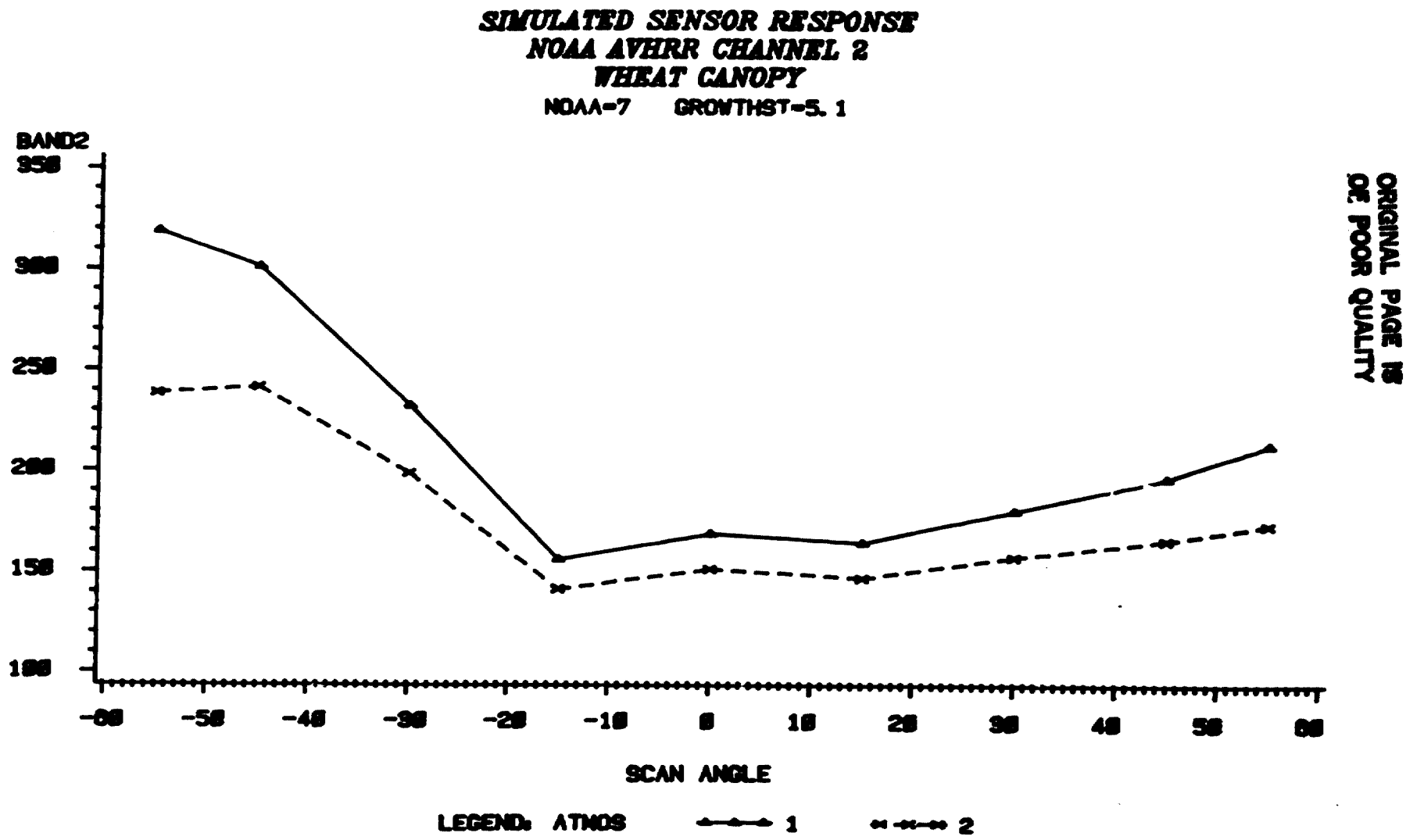

GRAPH NUMBER

VIEW ZENITH DOWNSUN=-60, UPSUN=+60
ATMOSPHERE 1=CLEAR,2=TURBID
GROWTHSTAGE 3.5=BOOT STAGE,
4.5=FULLY HEADED, 5.1=MILK STAGE

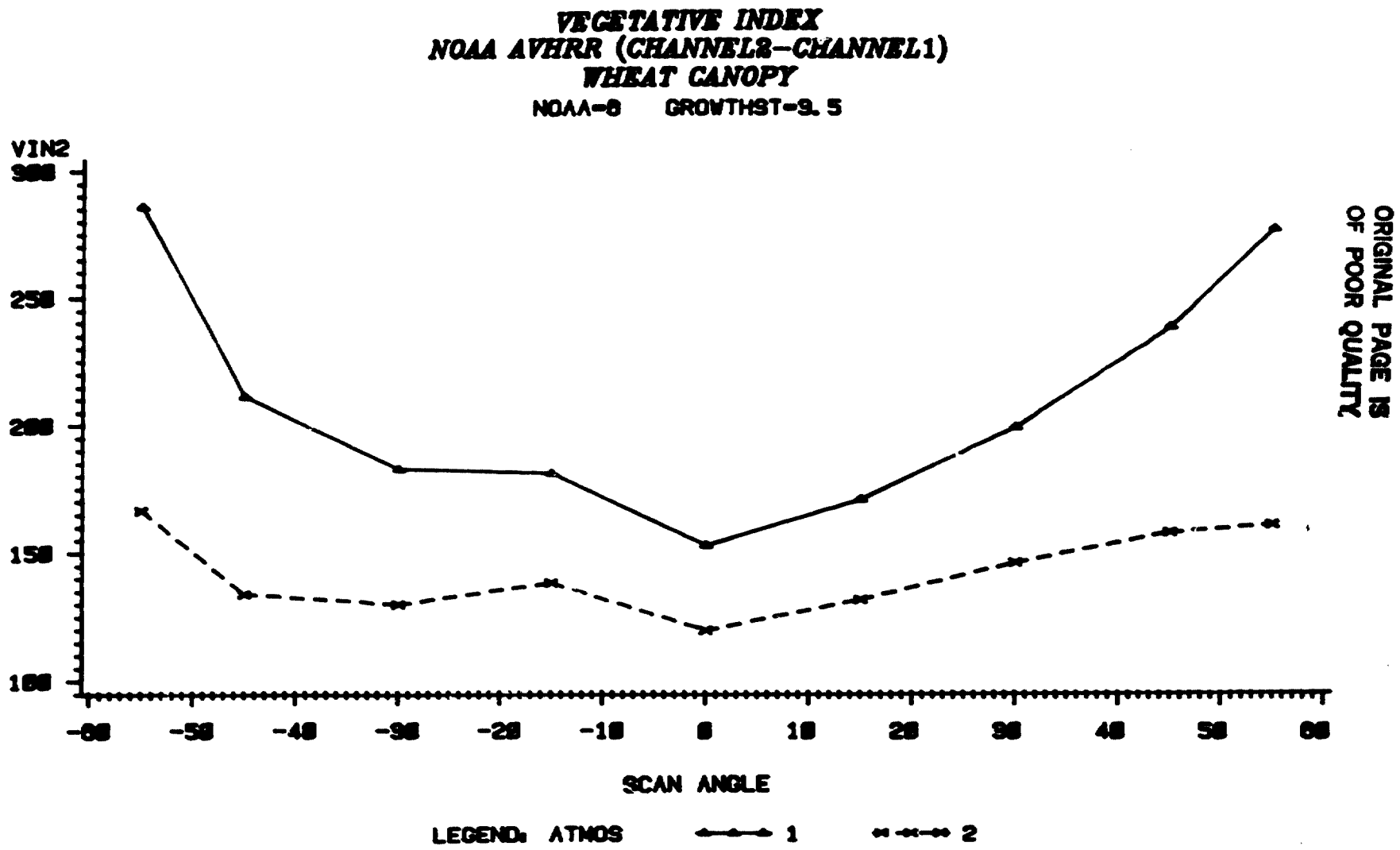

GRAPH NUMBER

VIEW ZENITH DOWNSUN=-60, UPSUN=+60
ATMOSPHERE 1=CLEAR,2=TURBID
GROWTHSTAGE 3.5=BOOT STAGE,
4.5=FULLY HEADED, 5.1=MILK STAGE

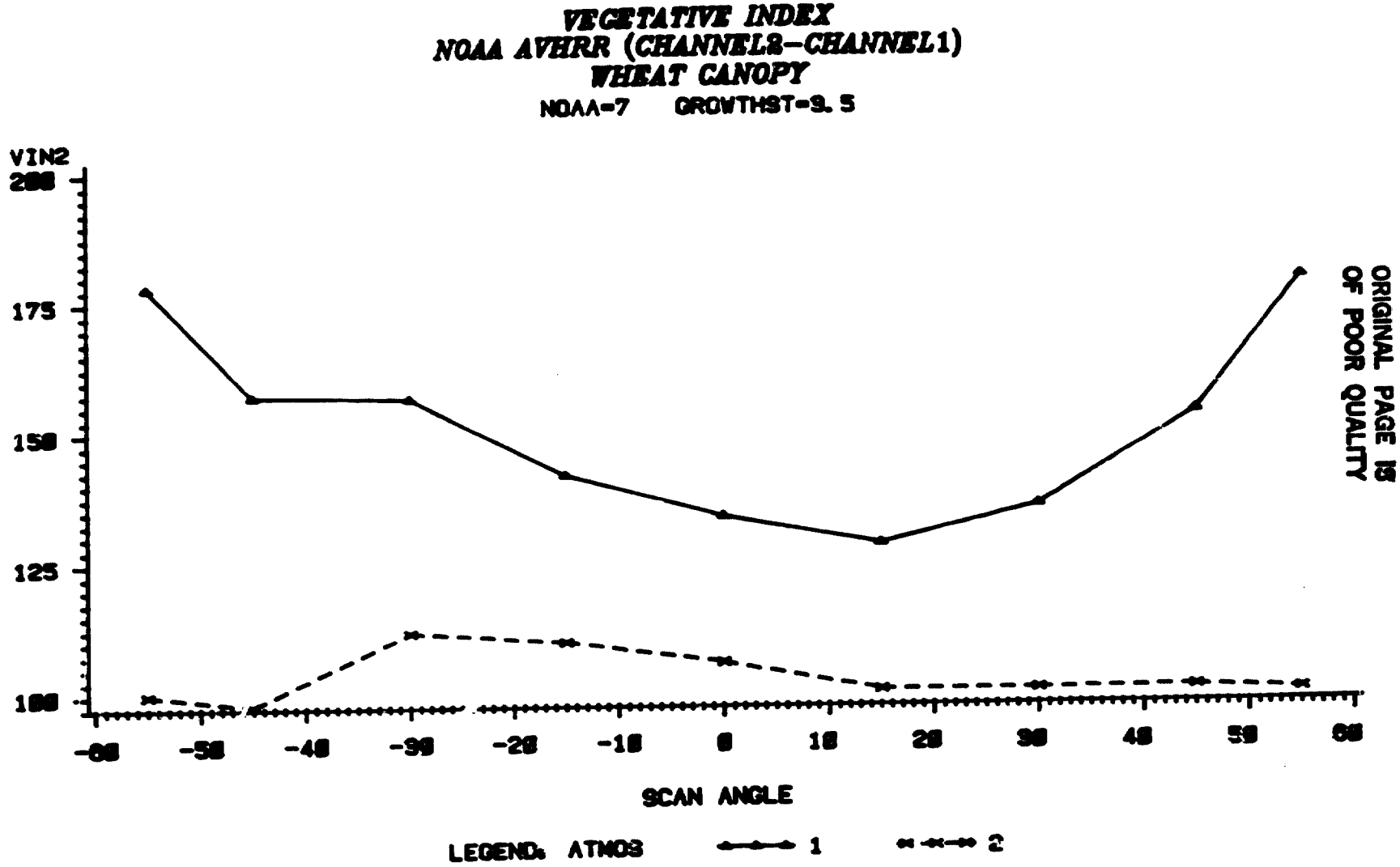

GRAPH NUMBER

VIEW ZENITH DOWNSUN=-60, UPSUN=+60
ATMOSPHERE 1=CLEAR,2=TURBID
GROWTHSTAGE 3.5=BOOT STAGE,
4.5=FULLY HEADED, 5.1=MILK STAGE

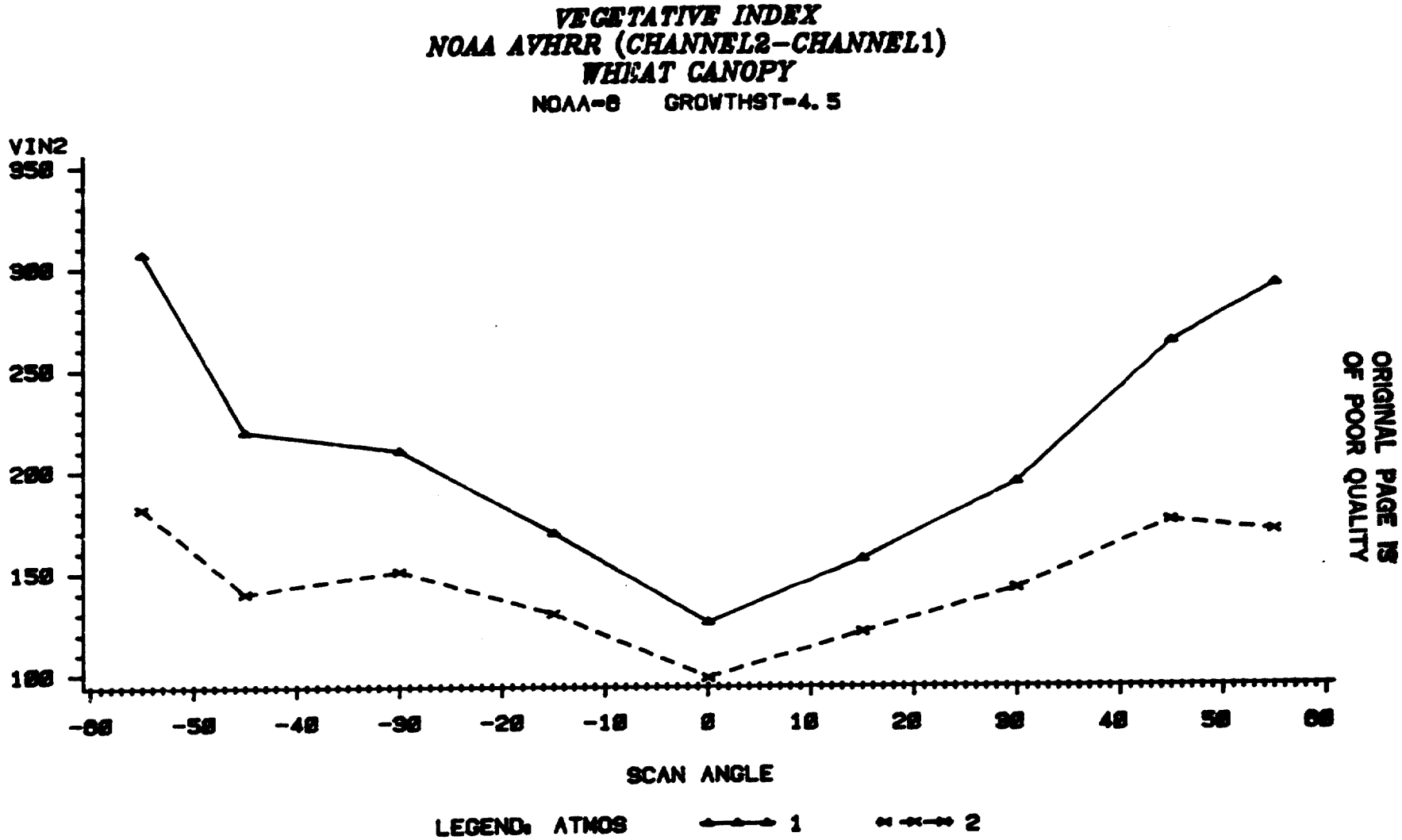

GRAPH NUMBER

VIEW ZENITH DOWNSUN=-60, UPSUN=+60
ATMOSPHERE 1=CLEAR,2=TURBID
GROWTHSTAGE 3.5=BOOT STAGE,
4.5=FULLY HEADED, 5.1=MILK STAGE

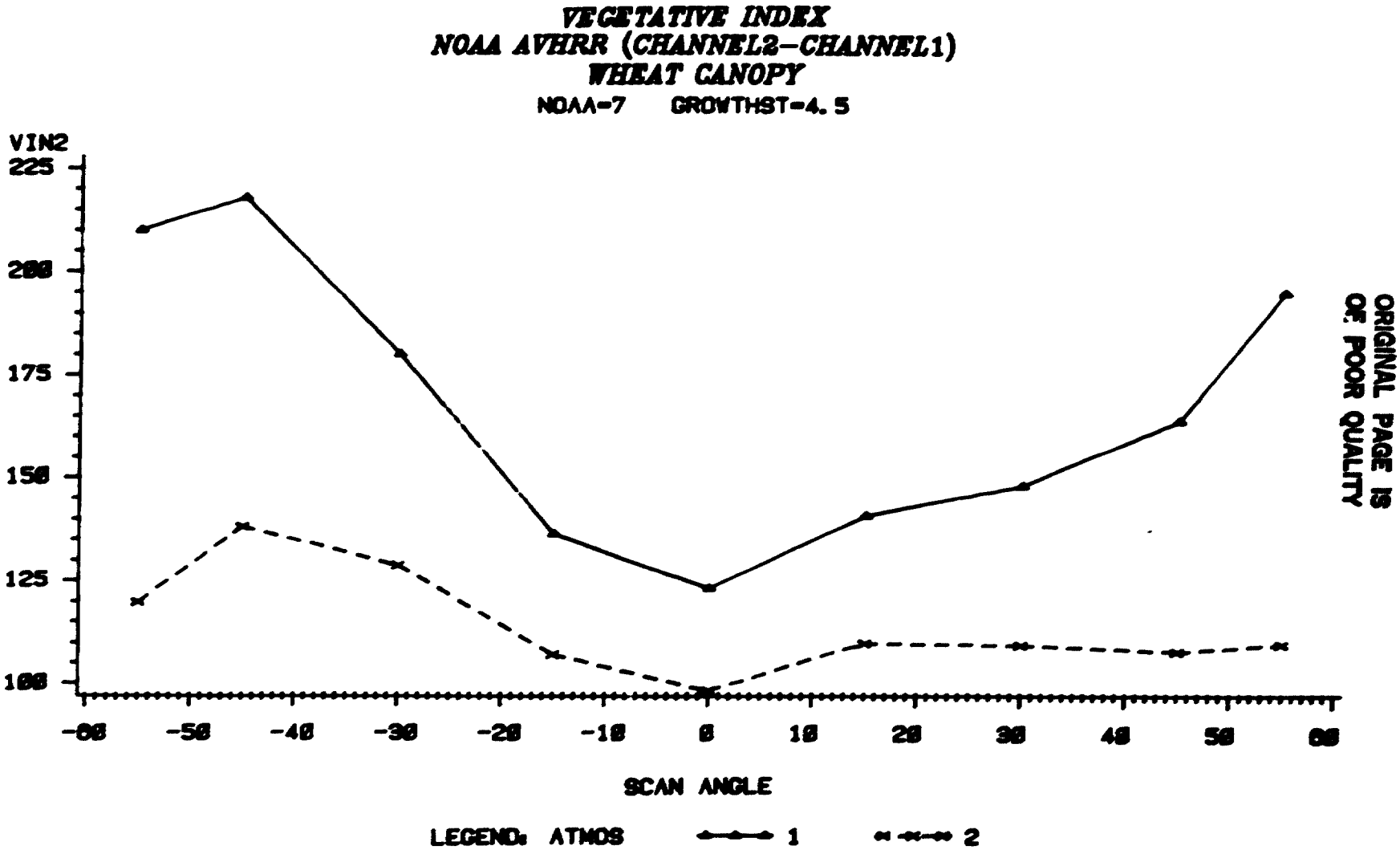

GRAPH NUMBER

VIEW ZENITH DOWNSUN=-60, UPSUN=+60
ATMOSPHERE 1=CLEAR,2=TURBID
GROWTHSTAGE 3.5=BOOT STAGE,
4.5=FULLY HEADED, 5.1=MILK STAGE

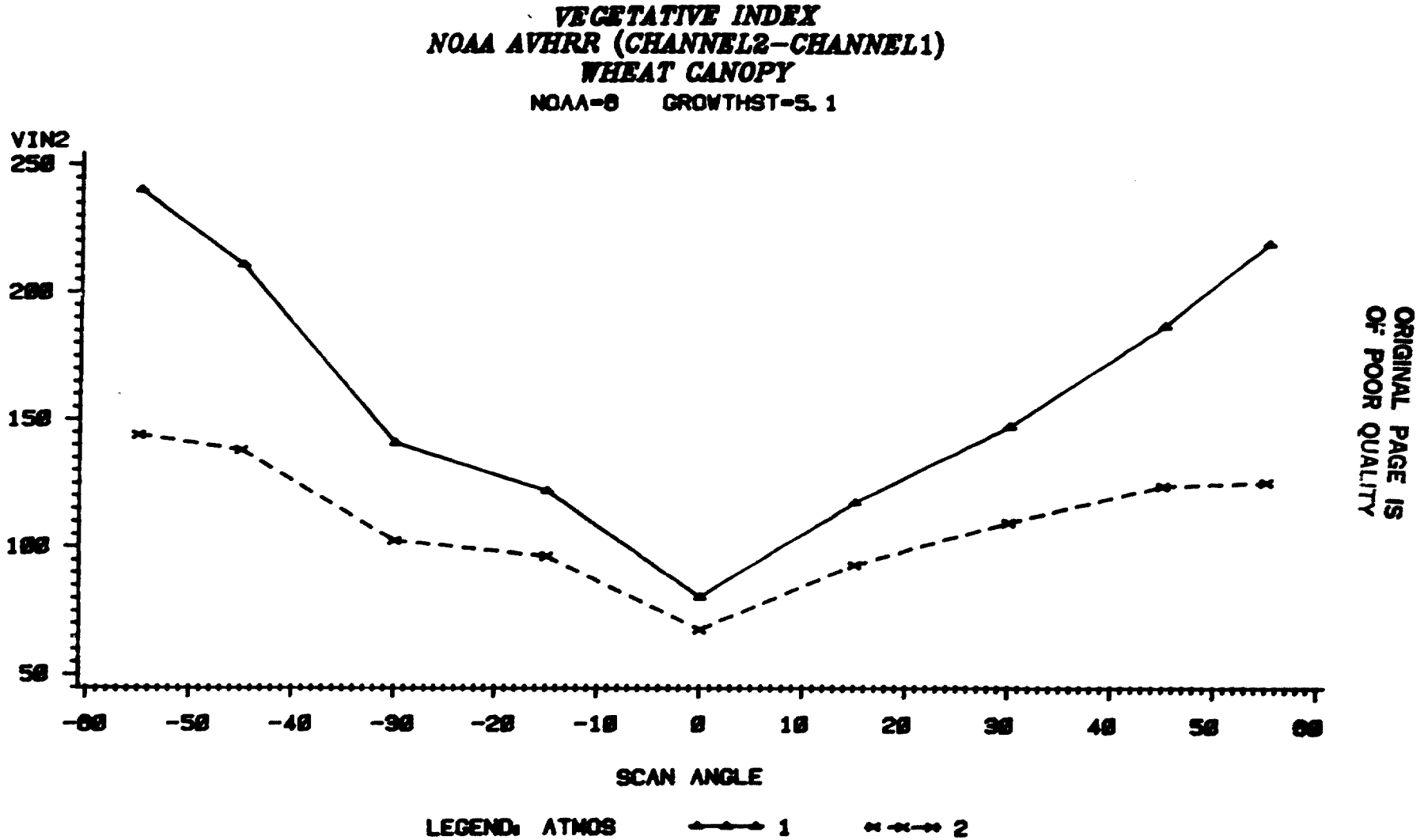

GRAPH NUMBER

VIEW ZENITH DOWNSUN=-60, UPSUN=+60
ATMOSPHERE 1=CLEAR,2=TURBID
GROWTHSTAGE 3.5=BOOT STAGE,
4.5=FULLY HEADED, 5.1=MILK STAGE

VEGETATIVE INDEX
NOAA AVHRR (CHANNEL2-CHANNEL1)
WHEAT CANOPY
NOAA=7 GROWTHST=5.1

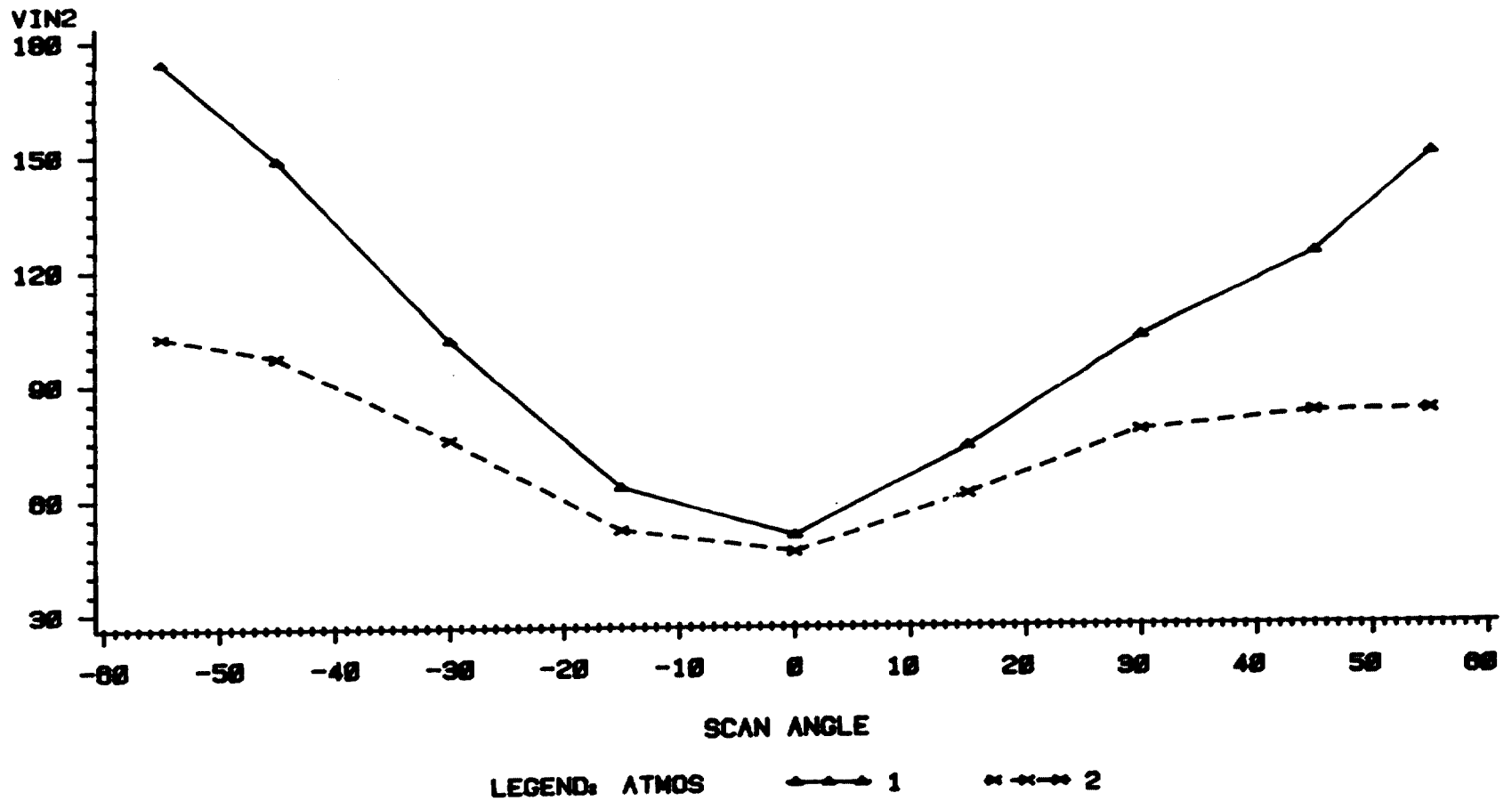

GRAPH NUMBER

VIEW ZENITH DOWNSUN=-60, UPSUN=+60
ATMOSPHERE 1=CLEAR,2=TURBID
GROWTHSTAGE 3.5=BOOT STAGE,
4.5=FULLY HEADED, 5.1=MILK STAGE

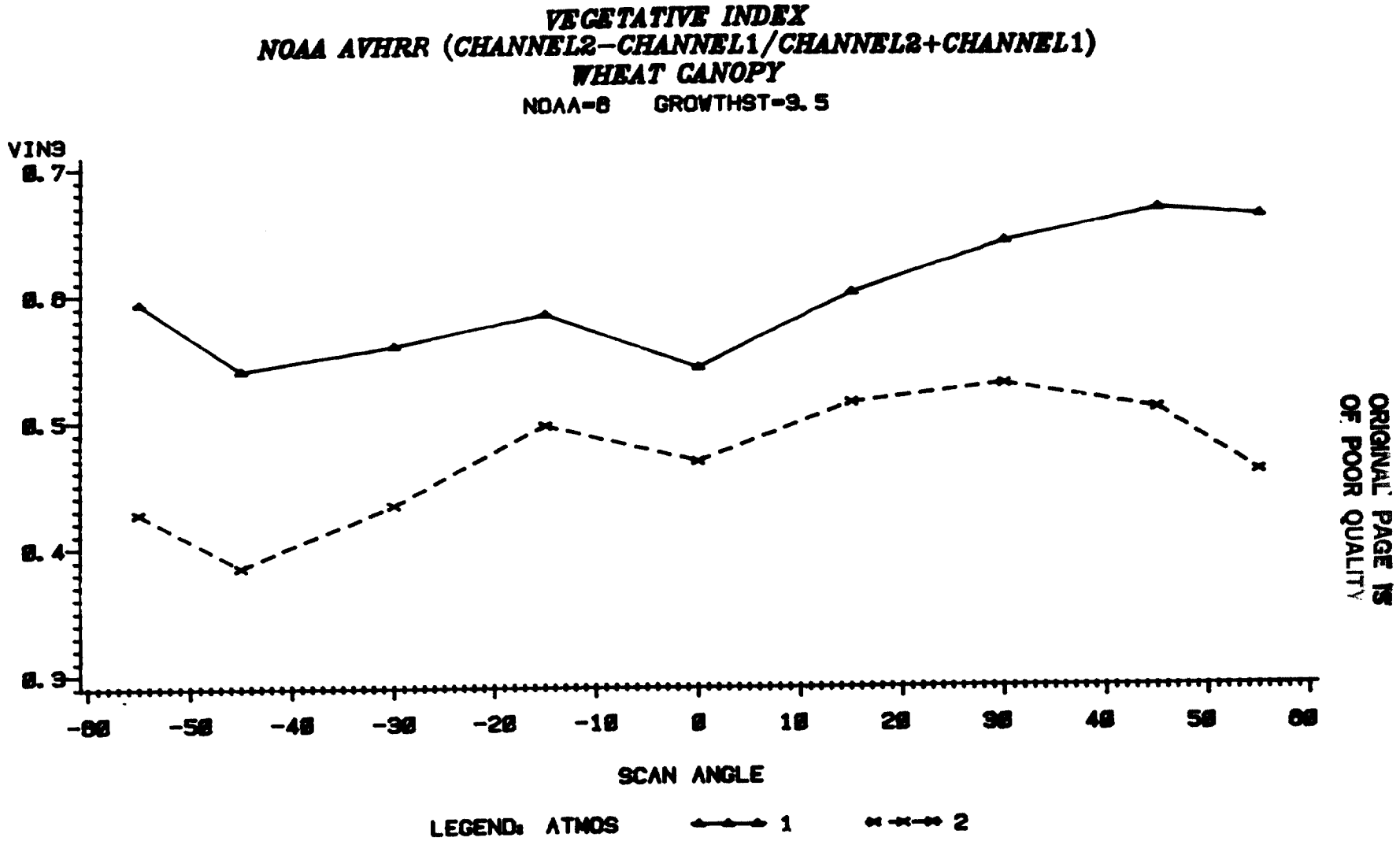

GRAPH NUMBER

VIEW ZENITH DOWNSUN=-60, UPSUN=+60
ATMOSPHERE 1=CLEAR,2=TURBID
GROWTHSTAGE 3.5=BOOT STAGE,
4.5=FULLY HEADED, 5.1=MILK STAGE

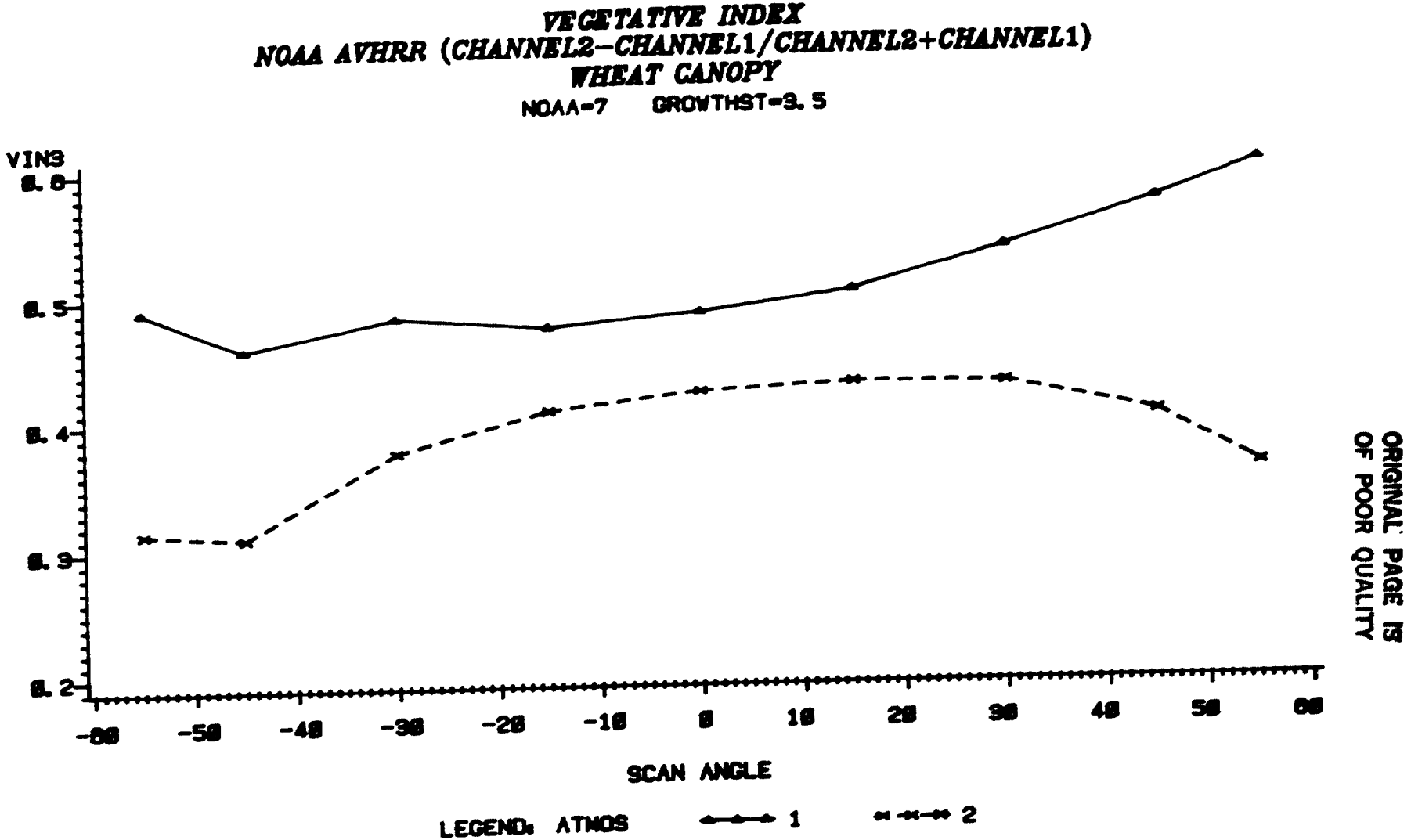

GRAPH NUMBER

VIEW ZENITH DOWNSUN=-60, UPSUN=+60
ATMOSPHERE 1=CLEAR,2=TURBID
GROWTHSTAGE 3.5=BOOT STAGE,
4.5=FULLY HEADED, 5.1=MILK STAGE

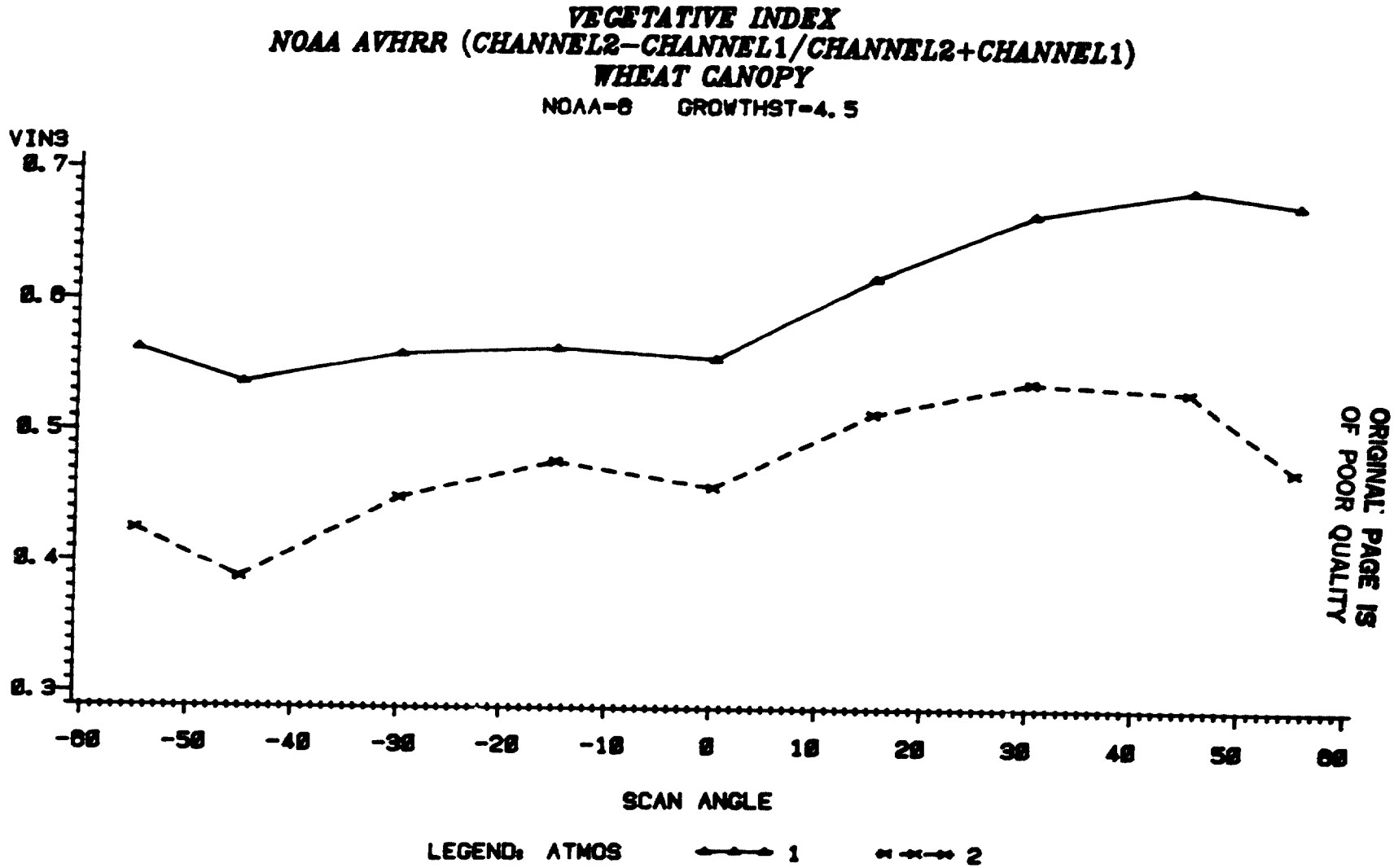

GRAPH NUMBER

VIEW ZENITH DOWNSUN=-60, UPSUN=+60
ATMOSPHERE 1=CLEAR,2=TURBID
GROWTHSTAGE 3.5=BOOT STAGE,
4.5=FULLY HEADED, 5.1=MILK STAGE

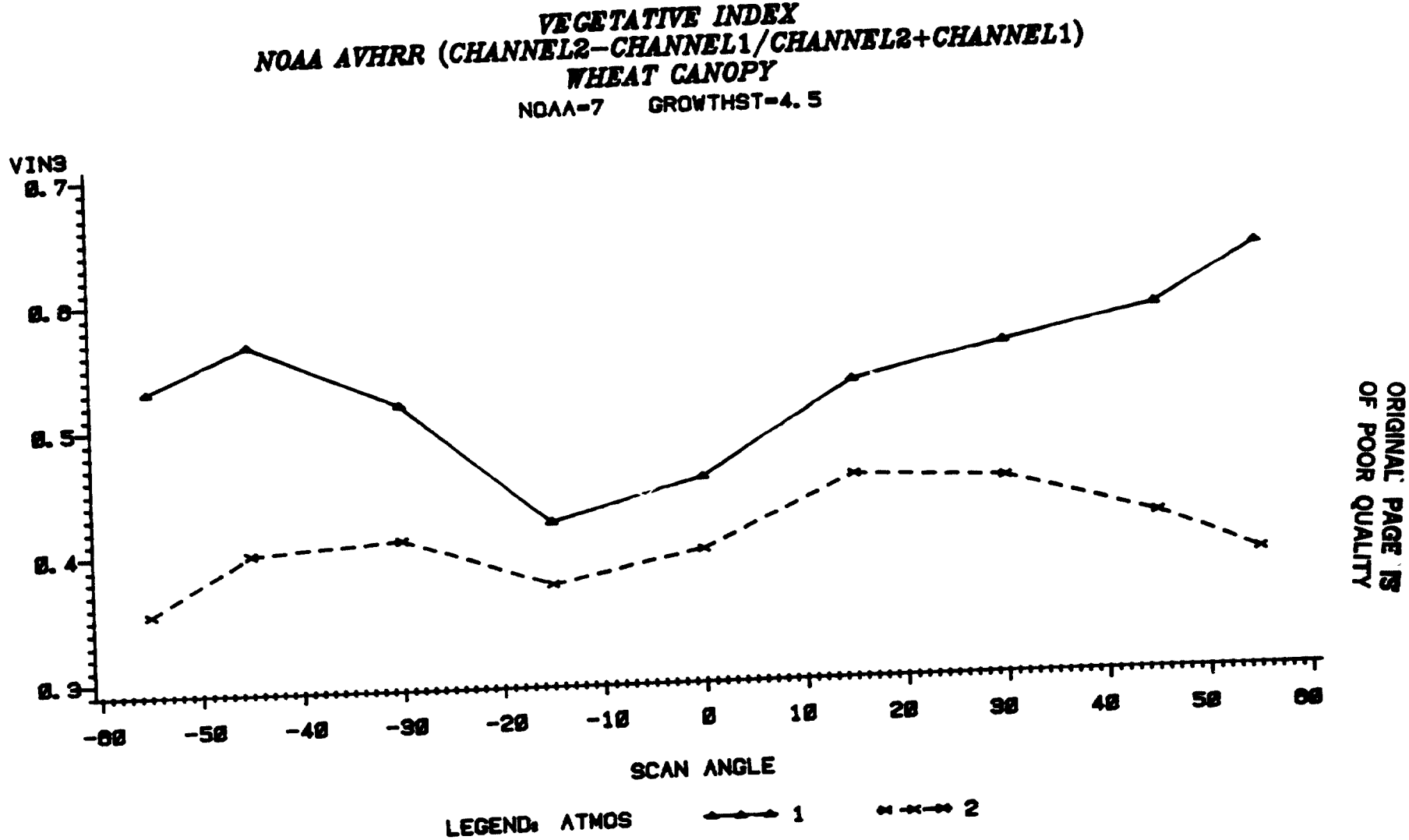

GRAPH NUMBER

VIEW ZENITH DOWNSUN=-60, UPSUN=+60
ATMOSPHERE 1=CLEAR,2=TURBID
GROWTHSTAGE 3.5=BOOT STAGE,
4.5=FULLY HEADED, 5.1=MILK STAGE

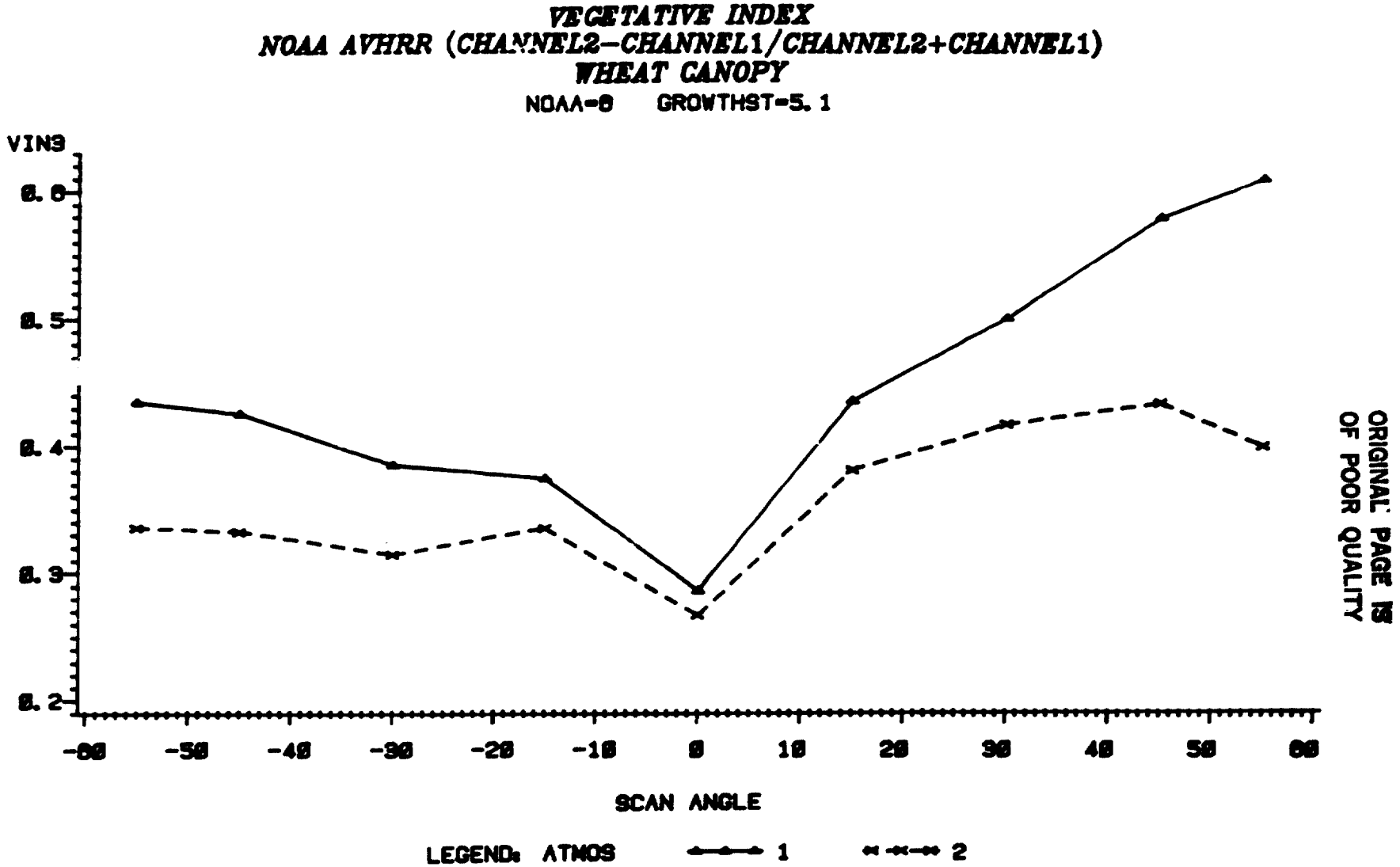

VEGETATIVE INDEX
NOAA AVHRR (CHANNEL2–CHANNEL1/CHANNEL2+CHANNEL1)
WHEAT CANOPY
NOAA-7 GROWTHST-5.1

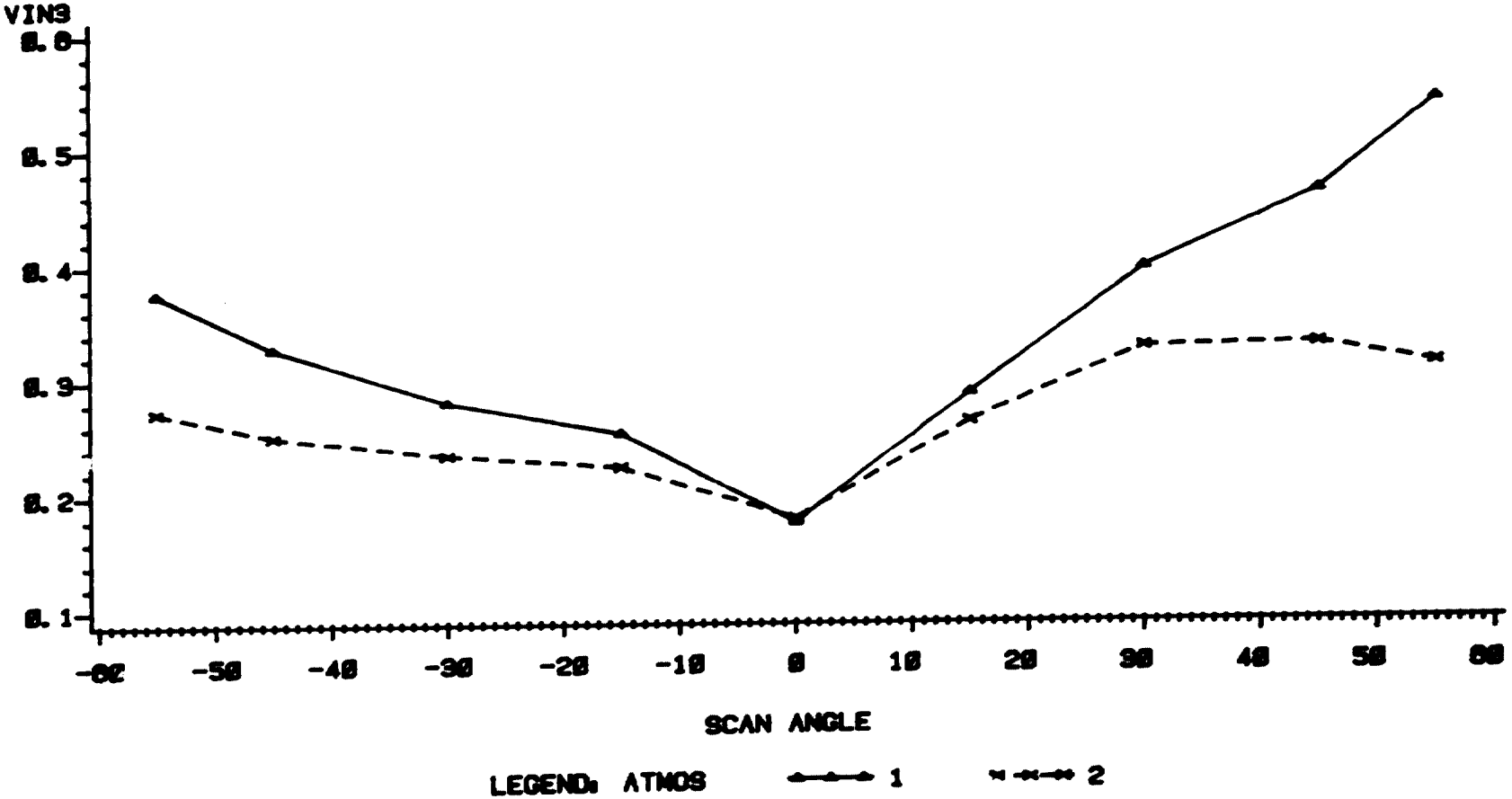

GRAPH NUMBER

VIEW ZENITH DOWNSUN=–60, UPSUN=+60
ATMOSPHERE 1=CLEAR,2=TURBID
GROWTHSTAGE 3.5=BOOT STAGE,
4.5=FULLY HEADED, 5.1=MILK STAGE